INSTITUTE OF FUNDAMENTAL TECHNOLOGICAL RESEARCH POLISH ACADEMY OF SCIENCES

Doctoral Dissertation

Design and Optimization of 2D Nanostructures based on Molybdenum

---

Mohammed Javeed Akhter

Supervisor: Prof. Wacław Kuś, Ph.D., Dr. Habil., Eng.

Warsaw 2024

Acknowledgement

I would like to express gratitude to my supervisor, Prof. Wacław Kuś, for introducing me to the concept of the molecular dynamics' simulation and evolutionary optimization and for the significant support he had provided me during the research work. I would also like to extend sincere thanks to prof. Tadeusz Burczyński for his immense support in shaping this work in the presented form.
I would like to thank my family and friends who always stay alongside and support me through all the hardship during my time as a PhD student.

List of symbols

MoS_2 : Molybdenum disulfide

TMDs : Transition metal dichalcogenides

MD : Molecular Dynamic

MS : Molecular statics

LAMMPS : Large-scale Atomic/Molecular Massive Parallel Simulator

f_i : force acting on atom

E_i : Potential energy

r_i : position of atom

θ : Angle between the atoms

θ_0 : Equilibrium angle,

ϕ : dihedral angle

m_i : mass of atom

r_i : position of atom

a_i : acceleration of atom

N : Number of atoms

N_f : Total translational degrees of freedom of the system

k_B : Boltzmann's constant

v^{α}_i : Velocity of atom α *in* i direction

T_0 : desired temperature

$T(t)$: Current temperature

Q : Effective mass of the thermostat

V : Total volume of the system

P_0 : Instantaneous pressure

$P(t)$: Desired pressures

τ_P : Time constant for pressure fluctuations

η : volume scaling factor

R_0 : center of mass of the system

SW : Stillinger-Weber

q_{ij} and q_{ji} : charges of atoms i and j

Q_2 : Two body (bond stretching) interactions

Q_3 : Three body (bond bending) interactions

U : Potential energy

F : Applied point load force,

d : Indentation depth at the center of the membrane,

r : Hole radius

ν : Poisson's ratio of the membrane

E^{2D} : 2D Young's modulus

σ_0^{2D} : 2D pretension

E : Elastic energy of a crystal

V_0 : Equilibrium volume

σ : Second-rank Cauchy stress tensor.

C_{ijkl} : Fourth-rank anisotropic elastic stiffness tensor.

ε : Second-rank small strain tensor.

ch : design vector

g_i : design variables

f(**ch**) : objective function

P : Properties of the nanostructure obtained from a given design vector **ch**,

$\mathbf{P}_{ref}$: Desired reference or prescribed properties of the nanostructure

$\mathbf{P}_{ij}$: Elastic constants to be used during objective function evaluation

Contents

Preamble

The work leading to this thesis was performed within the activities of project funded by the National Science Centre of Poland, awarded through decision number 2016/21/B/ST8/02450.

Part of the results presented here are published in the following peer reviewed articles:

- Akhter Mohammed Javeed, Kuś Wacław, Mrozek Adam and, Burczyński Tadeusz, Mechanical Properties of Monolayer MoS_2 with Randomly Distributed Defects, Materials 2020, 1307, 13; https://doi.org/10.3390/ma13061307
- Kuś Wacław, Akhter Mohammed Javeed and, Burczyński Tadeusz, Optimization of Monolayer MoS_2 with Prescribed Mechanical Properties, Materials 2022, 15(8), 2812; https://doi.org/10.3390/ma15082812

Atomistic simulations in this work were performed at the Interdisciplinary Centre for Mathematical and Computational Modelling at the University of Warsaw under grant GB80-16.

Synopsis

In the realm of next-generation electronics, a material of extraordinary promise has emerged: two-dimensional molybdenum disulfide, or MoS_2, a single layer of the mineral molybdenite. While its electromechanical properties have garnered significant attention, unlocking its full potential hinges on a thorough understanding of its mechanical behavior. This understanding is particularly crucial in the context of MoS_2 application in both nanodevices, such as sensors and transistors, and composite materials, where its potential to replace silicon as a reinforcement material arises due to the ever-present challenge of miniaturization in conventional electronics. However, a critical barrier exists in the form of mechanically weak interfaces that form when MoS_2 comes into contact with adjoining materials. To bridge this gap and pave the way for reliable MoS_2-based systems, this thesis delves into the fundamental mechanics of 2D MoS_2 using the powerful tools of molecular statics and dynamics simulations.

The first part of this thesis embarks on an exploration of the mechanical properties of MoS_2, specifically focusing on the impact of structural defects on its monolayer form. The overarching goal is to unravel the strengthening mechanisms at play within free-standing MoS_2 and decipher how defects influence its mechanical response. Through meticulous simulations involving randomly distributed defects at varying concentrations, ranging from 0% to 25%, the study sheds light on the detrimental effect of these imperfections on the material's elastic properties, with a particularly noticeable decline observed at the highest concentration. These valuable insights pave the way for informed design principles in the development of 2D MoS_2-based devices.

Building upon these foundational findings, the second part of the thesis embarks on a quest to optimize the nanostructure of MoS_2. Leveraging the power of an evolutionary algorithm (EA), the study sets out to design monolayer 2D MoS_2 nanostructures with precisely tailored elastic properties. This innovative approach, where the EA works hand-in-hand with molecular dynamics simulations, identifies the optimal size of elliptical voids required to achieve the desired mechanical characteristics. The success of this methodology underscores its potential in tailoring the mechanical properties of MoS_2 nanostructures.

Streszczenie

Wśród materiałów stosowanych w elektronice nowej generacji pojawił się niezwykle obiecujący dwuwymiarowy dwusiarczek molibdenu, czyli MoS_2, pojedyncza warstwa mineralnego molibdenitu. W literaturze znaczną uwagę poświęcono jego właściwościom elektromechanicznym, uwolnienie jego pełnego potencjału zależy od dokładnego zrozumienia jego własności mechanicznych. To zrozumienie jest szczególnie istotne w kontekście zastosowania MoS_2 zarówno w nanourządzeniach, takich jak czujniki i tranzystory, jak i materiałach kompozytowych, gdzie jego potencjał do zastąpienia krzemu jako materiału wzmacniającego wynika z stale obecnego wyzwania, jakim jest miniaturyzacja w elektronice. Istnieje jednak krytyczna bariera w postaci mechanicznie słabych powierzchni międzyfazowych, które tworzą się, gdy MoS_2 wchodzi w kontakt z przylegającymi materiałami. Aby wypełnić tę lukę i utorować drogę systemom opartym na MoS_2, w niniejszej pracy zgłębiono mechaniczne własności dwuwymiarowego MoS_2 przy użyciu narzędzi statyki i dynamiki molekularnej.

Pierwsza część tej pracy obejmuje badanie właściwości mechanicznych MoS_2, ze szczególnym uwzględnieniem wpływu defektów występujących w strukturze. Nadrzędnym celem jest odpowiedź na pytanie w jaki sposób defekty wpływają na jego własności mechaniczne. Dzięki symulacjom obejmującym losowo rozmieszczone defekty w zakresie od 0% do 25% liczby atomów, badanie pozwala określić wpływ tych niedoskonałości na właściwości sprężyste materiału, przy czym szczególnie zauważalny spadek wartości własności obserwuje się przy najwyższej liczbie defektów. Te spostrzeżenia pozwalają w przyszłości na projektowanie nanourządzeń 2D opartych na MoS_2.

Opierając się na wynikach w pierwszej części pracy, druga podejmuje próbę optymalizacji nanostruktury MoS_2. Wykorzystując możliwości algorytmu ewolucyjnego (EA), badanie ma na celu zaprojektowanie jednowarstwowych nanostruktur 2D MoS_2 o precyzyjnie dostosowanych właściwościach mechanicznych. To podejście, w którym EA współpracuje ręka w rękę z symulacjami dynamiki molekularnej, skutecznie określa optymalny rozmiar eliptycznych pustek wymaganych do osiągnięcia pożądanych właściwości mechanicznych. Sukces tej metodologii podkreśla jej skuteczność potencjał w dostosowywaniu właściwości mechanicznych nanostruktur MoS_2.

Chapter-1: Introduction

1.1 Graphene: A Single Layer with Remarkable Properties

Graphene, a single layer of carbon atoms arranged in a honeycomb pattern, is derived from graphite, the material commonly used in pencils. Within each graphene layer, carbon atoms are strongly bound by covalent bonds. Graphene along with other graphitic structures are shown in Figure 1.1. However, the forces holding the layers together, known as van der Waals forces, are relatively weak. This weak interaction allows for the separation of graphene layers, a property that makes it useful as an industrial dry lubricant. Graphite's high in-plane conductivity, reaching up to 10^5 S/cm, has led to its widespread use as an electrode material. Additionally, graphite exhibits excellent thermal conductivity, sharing many characteristics with metals [1]. The most remarkable properties of graphite emerge when it is exfoliated to isolate a single carbon layer. This process was successfully achieved in 2004 by Geim and Novoselov [2], earning them the Nobel Prize in Physics in 2010. Following the development of various mass production techniques, graphene's exceptional properties have been extensively studied [3].

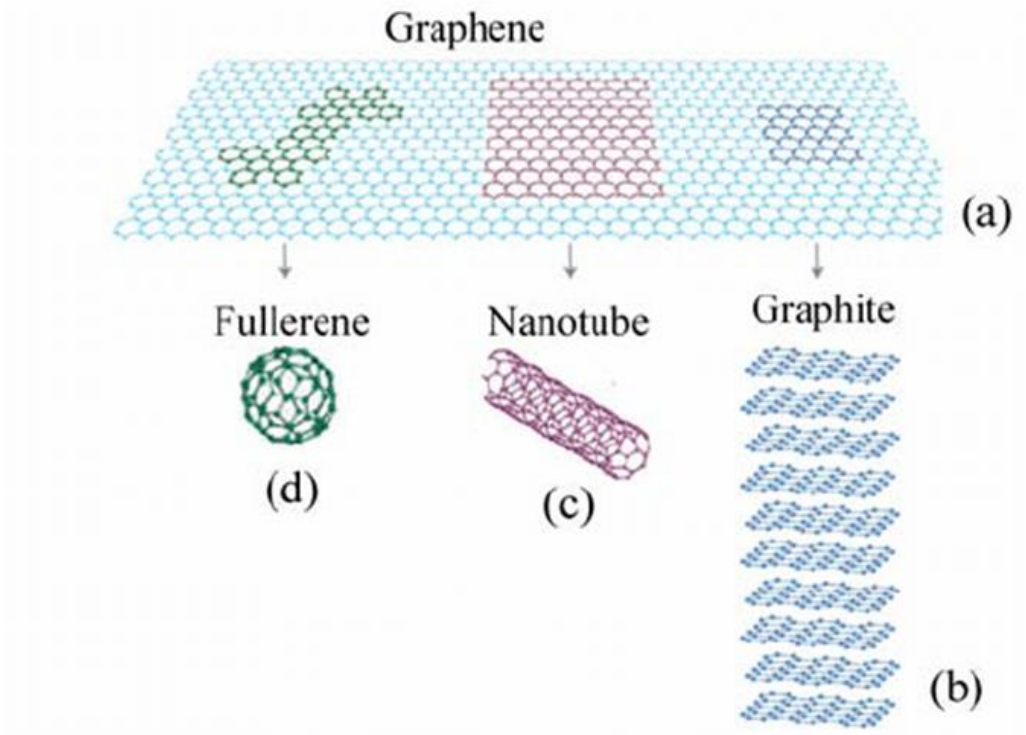

Figure 1.1 Schematic structure of (a) graphene, (b) graphite, (c) carbon nanotube and (d) fullerene. [232]

Graphene exhibits remarkable thermal and mechanical properties, making it a promising material for various applications. Its exceptional properties stem from its sp^2 hybridized bonds, which form a strong and stable honeycomb structure [4]. Graphene's outstanding mechanical properties, characterized by a Young's modulus of around 1 TPa and an intrinsic strength of 130 Gpa[5], make it highly resistant to deformation and breakage. This resilience is crucial for its use in delicate nanodevices, where even minor imperfections can lead to structural failure. The high surface-to-thickness ratio of graphene, a hallmark of two-dimensional (2D) materials, presents a wealth of opportunities for surface functionalization and modification. This property allows graphene to be tailored to specific applications by attaching various active principles and compounds. Graphene's surface sensitivity makes it a valuable material for biomolecule sensing and delivery. Its conductivity changes rapidly in response to the presence of ions or molecules, enabling it to detect and transport even minute quantities of these substances [6]. Graphene-based biosensors, fabricated using single layers of graphene deposited between electrodes, can be activated or deactivated by the presence of specific ions or molecules. These sensors hold promise for various applications in medical diagnostics and environmental monitoring [7].

Graphene is exceptional due to its unique band structure [8]. The conduction and valence bands touch at the Dirac point, resulting in electrons behaving as massless two-dimensional particles. This characteristic endows graphene with a range of remarkable properties, including:

- Extremely high carrier mobility: Graphene exhibits exceptional carrier mobility, far surpassing that of conventional semiconductors like silicon (1400 cm^2/Vs) [9]. This exceptional mobility enables faster and more efficient electronic devices.

- Ambipolarity: Graphene's Fermi level can be continuously adjusted within the conduction or valence band, allowing for electrostatic control of its doping [10]. This property facilitates the creation of p-n junctions without chemical doping and enables the tailoring of graphene's properties for specific applications.

- Potential for ohmic contacts: Graphene's tunable Fermi level holds the potential to match the work functions of different contact materials, minimizing contact resistance and leading to ohmic contacts [11].

- Challenges in FETs: The ambipolar and gapless nature of graphene poses challenges in field-effect transistors (FETs) due to the inability to completely switch off the current. Various

alternative structures, such as tunnel field-effect transistors and bilayer structures, have been proposed to address this challenge [12].

- Bilayer structures: Bilayer graphene structures exhibit a finite bandgap under certain conditions (Figure 1.2), offering the possibility of overcoming the limitations of single-layer graphene in FETs.

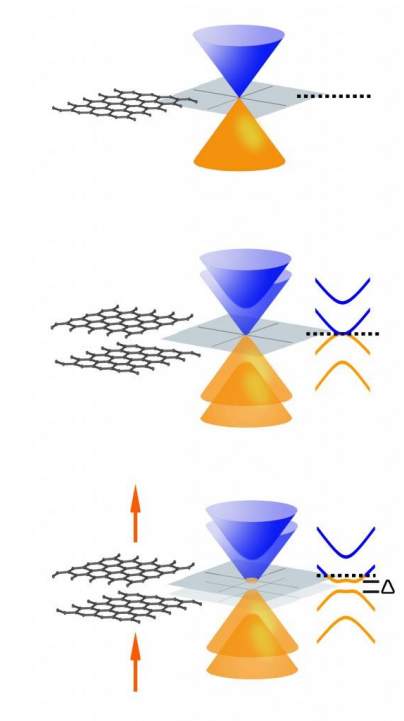

Figure 1.2 One of the most unusual features of single-layer graphene (top) is that its conical conduction and valence bands meet at a point – it has no bandgap. Symmetrical bilayer graphene (middle) also lacks a bandgap. Electrical fields (arrows) intro introduce asymmetry into the bilayer structure (bottom), yielding a bandgap (Δ) that can be selectively tuned. [233]

Graphene's extraordinary properties are driving its adoption in a diverse array of emerging fields, transitioning from theoretical concepts to practical applications. In the realm of optoelectronics, where high material absorption is crucial for efficient photon-to-carrier conversion, graphene presents unique advantages. Due to its gapless nature, free-doped graphene flakes can absorb light across a broad spectrum, ranging from ultraviolet to terahertz frequencies. For photon energies below 3 eV, a single carbon sheet exhibits an absorption rate of 2.3%, which increases linearly with the number of layers. While this remarkable absorption capability makes graphene an excellent candidate for transparent electrodes in photovoltaic devices, its single-layer transparency poses a challenge. To address this issue, researchers are exploring strategies to increase the absorption of single-layer graphene while maintaining its transparency.

1.2 Transition Metal Dichalcogenide Materials (TMDs): The 2D family blossom

Graphene's two-dimensional (2D) structure presents both advantages and challenges and has inspired the exploration of other 2D materials with complementary properties. The 2D nature of graphene offers several advantages, including its exceptional electrical conductivity, thermal conductivity, and mechanical strength. However, it also presents challenges, such as its limited ability to open and close a transistor channel, which is crucial for certain electronic applications. To overcome these limitations and explore a broader range of functionalities, researchers have turned their attention to other 2D materials. These materials exhibit a variety of properties that complement graphene, opening up new possibilities for device design and application. The recent discovery of a diverse family of 2D materials, each with its own unique characteristics, has further expanded the potential of this field. These materials offer a vast array of properties to explore and combine, providing a rich landscape for materials design and innovation.

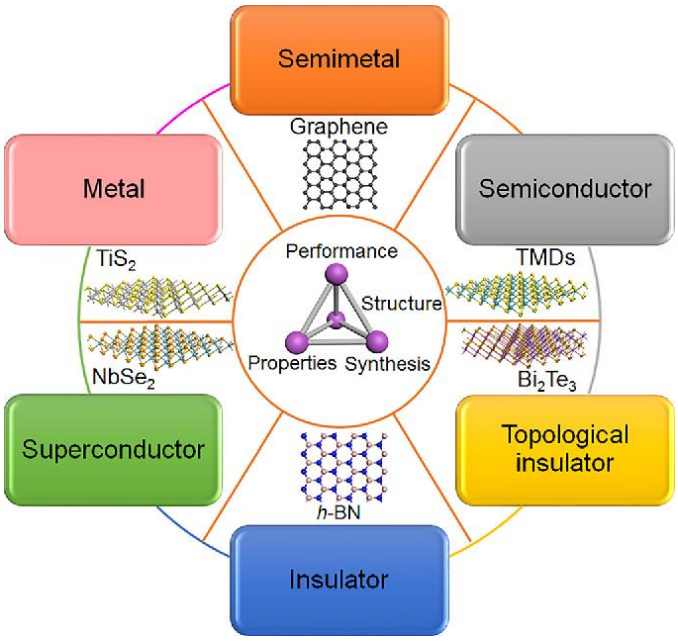

Figure 1.3 The denomination of 2D materials encompasses a wide variety of materials with different properties, which can be combined to design and create a full new set of devices based on them. Figure inspired in [5,32].

Figure 1.3 highlights a diverse range of 2D materials, each exhibiting unique properties that complement graphene. These materials include native insulators like hexagonal boron nitride (h-BN), semiconductors such as transition metal dichalcogenides (TMDs), metals like MoS_2 and TiS_2, superconductors, and topological insulators like $NbSe_2$ and Sb_2Te_3 [13]. The weak interaction between layers held together by van der Waals forces enables the stacking of these 2D materials to create novel van der Waals heterostructures [14]. This process, akin to a "Lego game," allows for the

combination of materials with diverse properties, leading to the emergence of new functionalities as shown in Figure 1.4 [15] This ability to tailor material properties by stacking different 2D materials opens up a vast array of possibilities for device design and application. By combining the unique characteristics of individual 2D materials, researchers can create heterostructures with enhanced performance and novel functionalities.

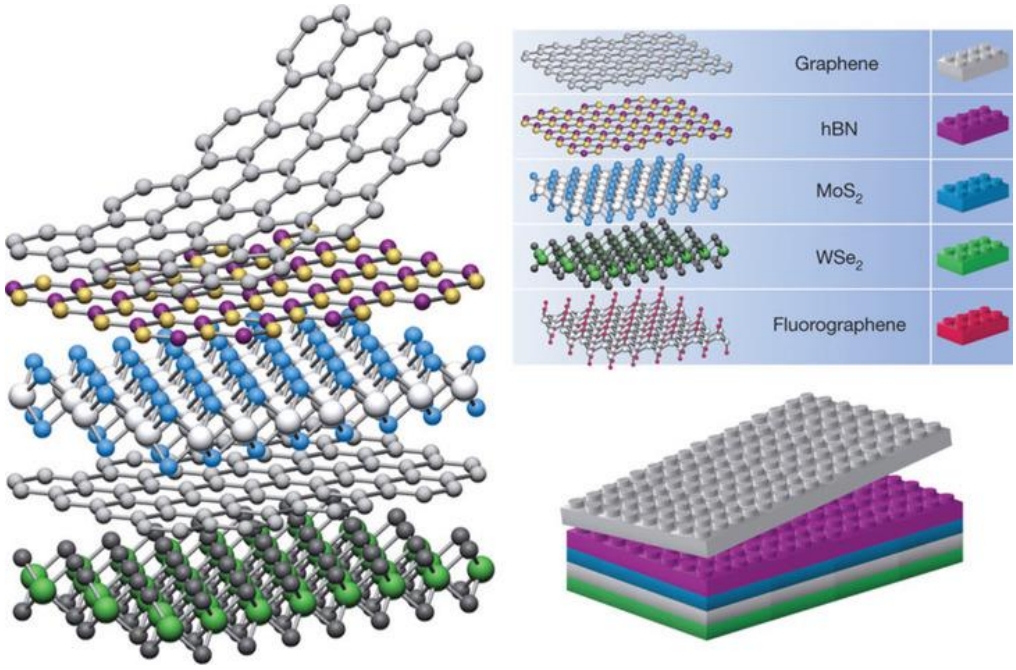

Figure 1.4 Vertical stacking of 2D materials forming heterostructures [17].

Transition metal dichalcogenides (TMDs) are a diverse group of materials with unique properties that make them promising for a variety of applications. These materials, characterized by their formula MX_2, where M is a transition metal (Mo, W) and X is a chalcogen (S, Se, or Te), exhibit a wide range of behaviors, including 2H-MoS_2 semiconducting and 1T-MoS_2 metallic properties [16]. TMDs transition metal represents from group 4 to 10 and chalcogen element encompass a diverse range of layered materials with varying electronic properties as shown in Figure 1.5. These materials exhibit a spectrum of properties, ranging from insulating (e.g., HfS_2) to semiconducting (e.g., 2H-MoS_2 and 2H-WS_2), semi-metallic (e.g., WTe_2 and $TiSe_2$) to truly metallic (e.g., NbS_2 and VSe_2) [17]. The tunable bandgap of TMDs arises from the gradual filling of the nonbonding *d* orbitals of transition metal electrons. Additionally, the presence of unpaired *d* orbitals in transition metals leads to exotic properties such as superconductivity, charge density waves (CDW), magnetism, and Mott transition (metal to non-metal transition).

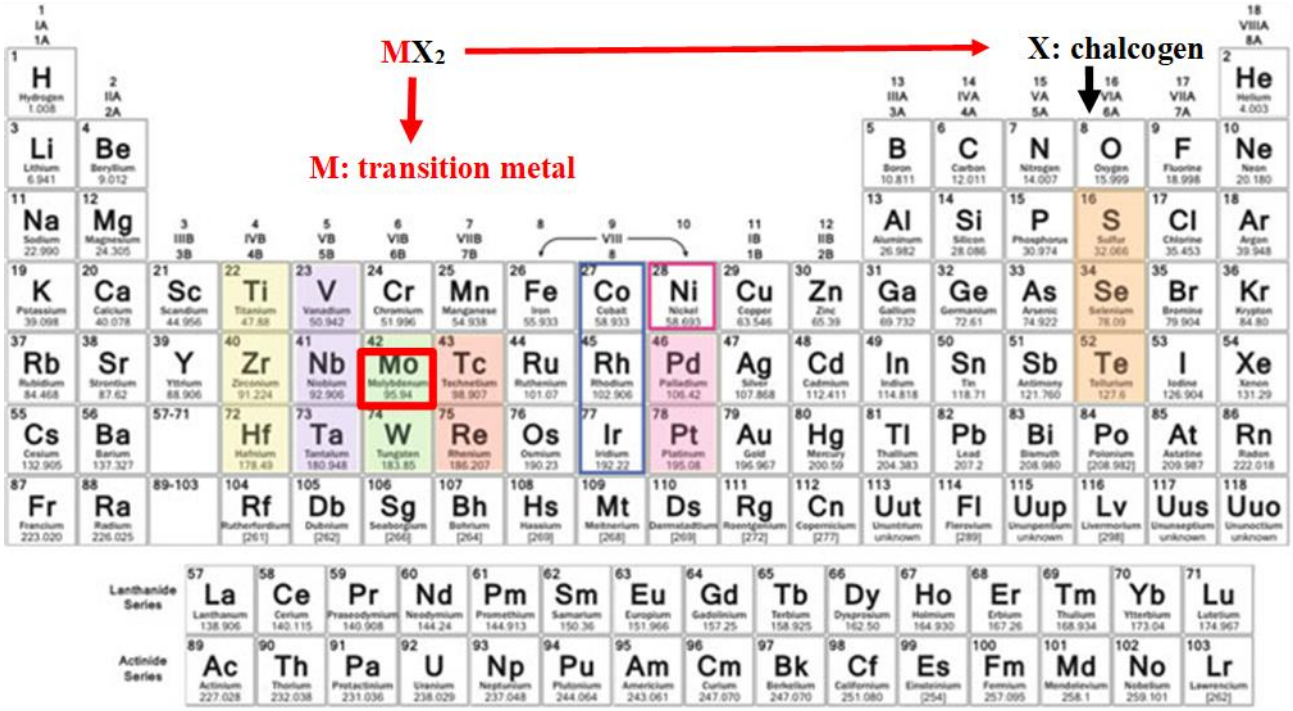

Figure 1.5 The transition metals and the three chalcogen elements that crystallize into layered structures are highlighted in the Periodic Table. The transition metals that crystallize into layered structures with some chalcogens but not with others are framed. The columns in the Periodic Table show both 'old' and new labels, i.e. chalcogens can be referred to as either group VIA or group 16 elements [18]

One remarkable feature of TMDs is the difference in properties between their monolayer and bulk counterparts. This distinction arises from quantum confinement effects, which cause the monolayer material to transition from an indirect bandgap in the bulk form to a direct bandgap in the single-layer form [19]. The direct bandgap of monolayer TMDs, along with their sizeable bandgaps, makes them attractive candidates for logic circuits [20–22]. Their atomic-body thickness also enables effective control of the channel by the gate [23], mitigating the short-channel effects that can hinder performance in conventional transistors. In addition to their potential for logic applications, TMDs also exhibit promising optoelectronic properties. Their high absorption coefficients, comparable to those of silicon [24], and their diverse absorption spectra make them suitable for the development of photodetectors, multijunction solar cells, and ultrathin solar cells [25–29]. Furthermore, TMDs have demonstrated the ability to emit light, making them viable materials for light-emitting diodes (LEDs). Researchers have successfully fabricated LEDs using various TMDs, showcasing their potential in optoelectronic devices [30,31].

There is growing interest in exploring the properties of other two-dimensional (2D) materials as an alternative approach. Investigating the characteristics of other 2D materials holds promise for addressing the limitations of graphene and opening up new possibilities for semiconductor

applications. Researchers are actively seeking alternative 2D materials that can fulfill specific application requirements. One such material is mono-layered molybdenum disulfide ($MLMoS_2$), which is the focus of study in this research. By exploring and understanding the properties and behavior of materials like $MLMoS_2$, researchers aim to find suitable alternatives to graphene for specific applications, taking into consideration factors such as band gap engineering, electrical properties, and overall performance.

1.2.1 Molybdenum disulfide (MoS_2):

Molybdenum disulfide (MoS_2) holds immense promise for next-generation electronic and optoelectronic devices due to its unique properties [32]. As the first semiconducting transition metal dichalcogenide (TMD) obtained in a monolayer form, MoS_2 exhibits a remarkable transformation in its band structure, transitioning from an indirect bandgap in bulk form to a direct bandgap in the monolayer state. This unique property complements graphene, a zero-bandgap material, making MoS_2 an ideal candidate for various applications. MoS_2 boasts an impressive room-temperature carrier mobility of approximately 100 $cm^2 V^{-1}s^{-1}$, along with a large switching on/off ratio exceeding 10^8 [20]. Moreover, monolayer MoS_2 exhibits exceptional properties such as valley polarization and valley Hall effect, arising from its lack of inversion symmetry [33]. Furthermore, 2D MoS_2 emerges as a promising low-cost and highly efficient electrocatalyst for the hydrogen evolution reaction (HER). Its catalytic activity can be further enhanced by increasing edge sites and defect density, as well as by employing heteroatom substitutional doping [34]. Figure 1.6 depicts the exponential increase in interest over the past several years, as evidenced by the number of publications per year found in the Web of Knowledge using the keywords "MoS_2" and "monolayer." This graph illustrates the growing attention and research efforts dedicated to two-dimensional TMD MoS_2.

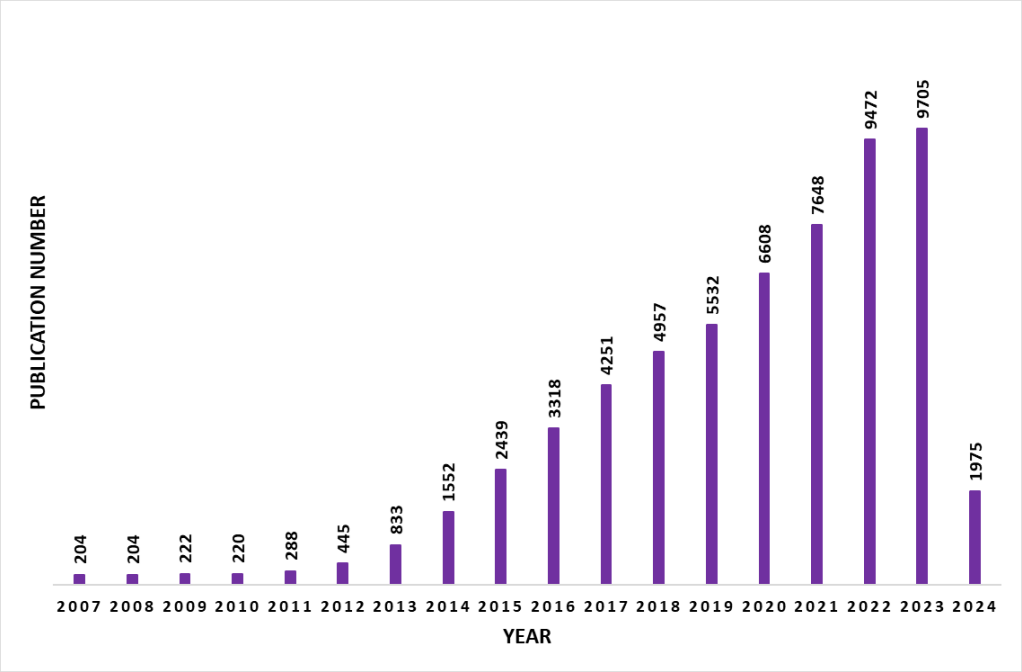

Figure 1.6 A histogram showing the number of papers about MoS_2 vs. publication year (up to Feb 2024) . Data obtained from https://app.dimensions.ai/discover/publication?search_mode=content&search_text=2D%20molybdenum%20disulfide&search_type=kws&search_field=full_search

Molybdenum disulfide (MoS_2) exhibits a layered structure, where each layer consists of covalently bonded S-Mo-S atomic planes held together by weak van der Waals forces in the bulk form [35]. In monolayer MoS_2, two polymorphs exist, distinguished by the coordination manner between the Mo atom and its surrounding six S atoms. These polymorphs are trigonal prismatic coordination (D 3h point group), commonly referred to as 1H, and octahedral coordination (D 3d), commonly known as 1T (Figure 1.7 a, b) [36]. Multilayer MoS_2 displays a wider range of polymorphs due to variations in the stacking sequence between layers. Three extensively studied polytypes are 1T, 2H, and 3R. The letters represent different crystal symmetry systems: trigonal (1T), hexagonal (2H), and rhombohedral (3R). The digits indicate the number of layers in each unit cell (Figure 1.7 c, d) [37]. The 2H and 3R phases are energetically more favorable than the metastable 1T phase and are commonly found in natural minerals and synthetic products. Both 2H and 3R share the same intralayer coordination configuration (trigonal prismatic) but differ in interlayer coupling manners. In the 2H polytype, two layers are fully eclipsed, with Mo (S) atoms of one layer positioned directly above S (Mo) atoms of the other layer. In the 3R phase, three layers are staggered, with S atoms in the middle layer located above Mo atoms in the bottom layer and below the hollow hexagonal center of the top layer. The lattice orientation between adjacent layers in 2H-MoS_2 exhibits a 60° twist, while all three layers in the unit cell of 3R-MoS_2 share the same crystal direction.

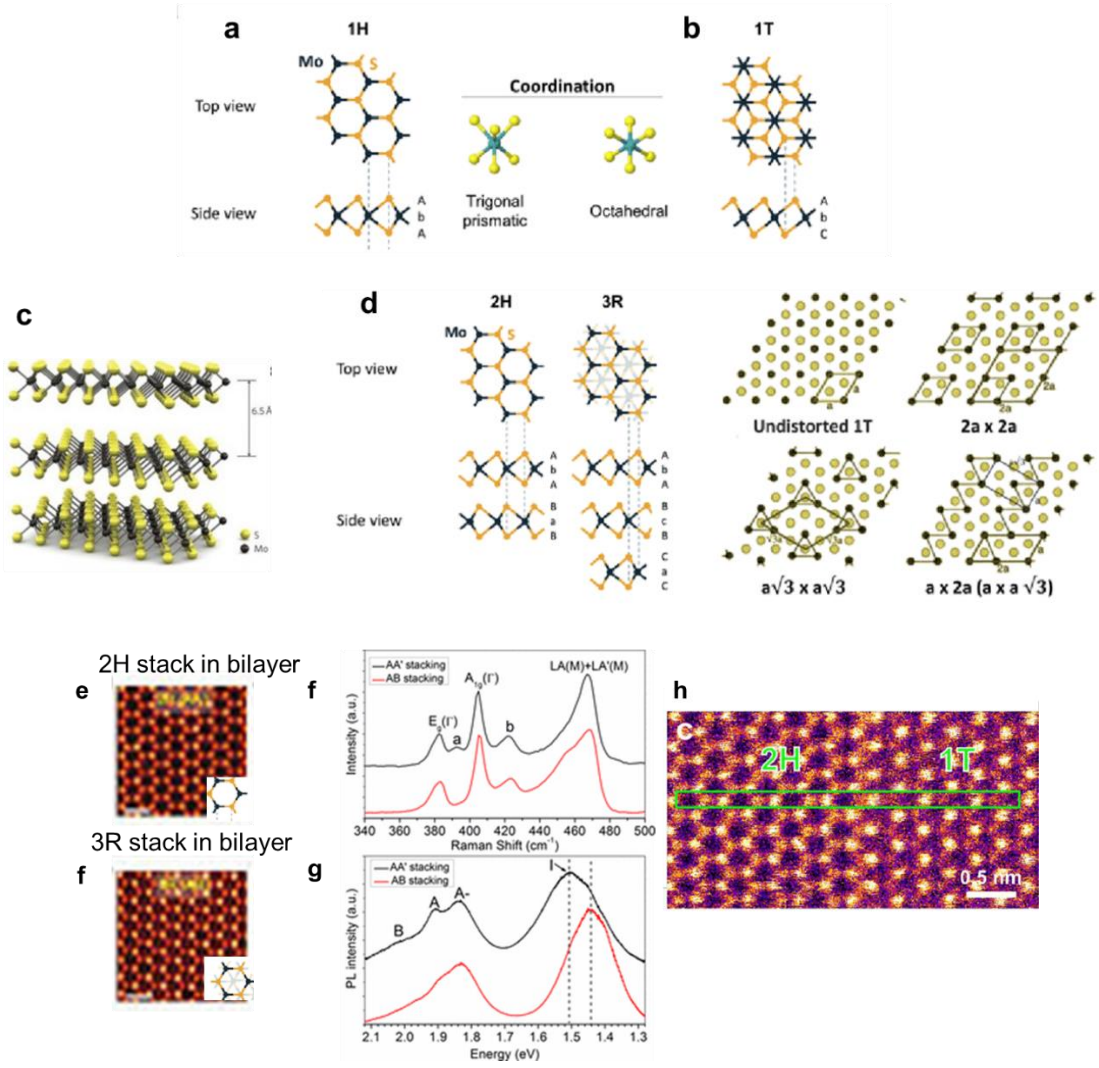

Figure 1.7 Structural models and characterizations of various polymorph phases of MoS_2. *(a,b) Atomic models showing 1H and 1T phases of monolayer* MoS_2, *respectively. (c) 3D schematic illustration of multilayer* MoS_2. *(d) Atomic models displaying three different phases, 1T, 2H and 3R, in multilayer* MoS_2, *respectively. (e,f) ADF-STEM images of bilayer* MoS_2 *exhibiting 2H and 3R stacking sequences, respectively, where an atomic column corresponding to a pair of stacked sulphur atoms in the centre of each hexagonal ring can be seen in (f) as a distinct feature of 3R polytype. (g,h) Resonance Raman and PL spectra displaying distinguishable variations between 2H and 3R stacked bilayer* MoS_2. *(i) ADF-STEM image showing an artificial generation of 1T phase in the 2Hphase monolayer* MoS_2 *by a controllable electron irradiation using in-situ scanning electron microscopy. Blue solid circles, yellow solid circles and yellow dashed circles indicate Mo, 2S and 1S atoms, respectively. The green dashed line shows the boundary between 1H and 1T phase.*[[36], [38], [39], [40]]

Annular dark-field scanning transmission electron microscopy (ADF-STEM) is the most direct and unambiguous tool for distinguishing between different phases of 2D MoS_2 due to its atomic resolution and quantitative relationship between intensity and atomic number (Figure 1.7 e, f) [38,41]. Raman and PL spectroscopy can also identify different stacking configurations in bilayer and trilayer MoS_2 (Figure 1.7 g, h) [39,42]. Phase conversions between different MoS_2 phases, particularly between 2H and 1T phases, have been studied extensively (Figure 1.7 i), [40,43]. 2H-MoS_2 is a diamagnetic semiconductor, while 1T-MoS_2 is a paramagnetic metal [37]. The phase transition from 2H to 1T can be triggered by intercalation with alkali metals, rhenium (Re) atom doping, or controllable electron beam irradiation [44,45]. These methods alter the *d*-electron count for Mo atoms in MoS_2, destabilizing the original 2H phase.

1.2.2 Properties of Molybdenum disulfide (MoS_2):

Monolayer and few-layer MoS_2 possess unique properties that make them promising materials for sensing applications [32,46,47]. These materials can be synthesized through various methods, including mechanical exfoliation, liquid exfoliation, and chemical vapor deposition (CVD) [17,47].

- Mechanical exfoliation: Involves peeling off thin layers of MoS_2 from bulk MoS_2 using adhesive tape or other mechanical means (Figure 1.8 a).
- Liquid exfoliation: Utilizes solvents or liquid solutions to disperse MoS_2 flakes into individual layers (Figure 1.8 b).
- Chemical vapor deposition (CVD): A growth technique that deposits thin films of MoS_2 onto a substrate through chemical reactions.

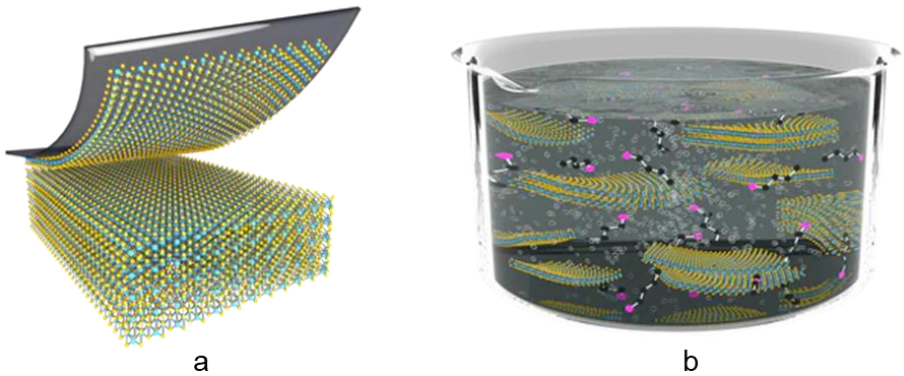

Figure 1.8 (a) Mechanical exfoliation involves peeling successive layers from a van der Waals material using a tape. (b) Liquid exfoliation often uses bubbles to force layers apart.

Among the liquid exfoliation methods, the lithium intercalation technique can induce a phase transition in MoS_2, converting the 2H phase to octahedral coordinated phases [17,47,48]. These phases exhibit distinct properties compared to the 2H phase, potentially enhancing their sensing capabilities.

Molybdenum disulfide (MoS_2) possesses remarkable mechanical properties that make it suitable for flexible nanodevices. Studies on 5-25 layers and monolayer MoS_2 have demonstrated its exceptional mechanical strength [49]. Monolayer MoS_2 exhibits a 2D elastic modulus of approximately 170 to 180 N/m and a Young's modulus of around 270 GPa, slightly exceeding that of stainless steel [50,51]. Thin-film transistors fabricated using CVD-grown MoS_2 have shown remarkable mechanical flexibility without compromising their electrical performance upon bending [52]. These findings suggest that MoS_2 is a promising candidate for the development of flexible nanodevices, Mechanical properties of MoS_2 are shown in Table 1:

Table 1: Mechanical properties of MoS_2

Property	**Value**
2D Elastic Modulus	~170 to 180 N/m
Young's Modulus	~270 GPa

The exceptional mechanical properties of MoS_2, coupled with its remarkable electrical and optical properties, make it a versatile material with immense potential for various applications, including flexible electronics, energy storage, and sensing devices.

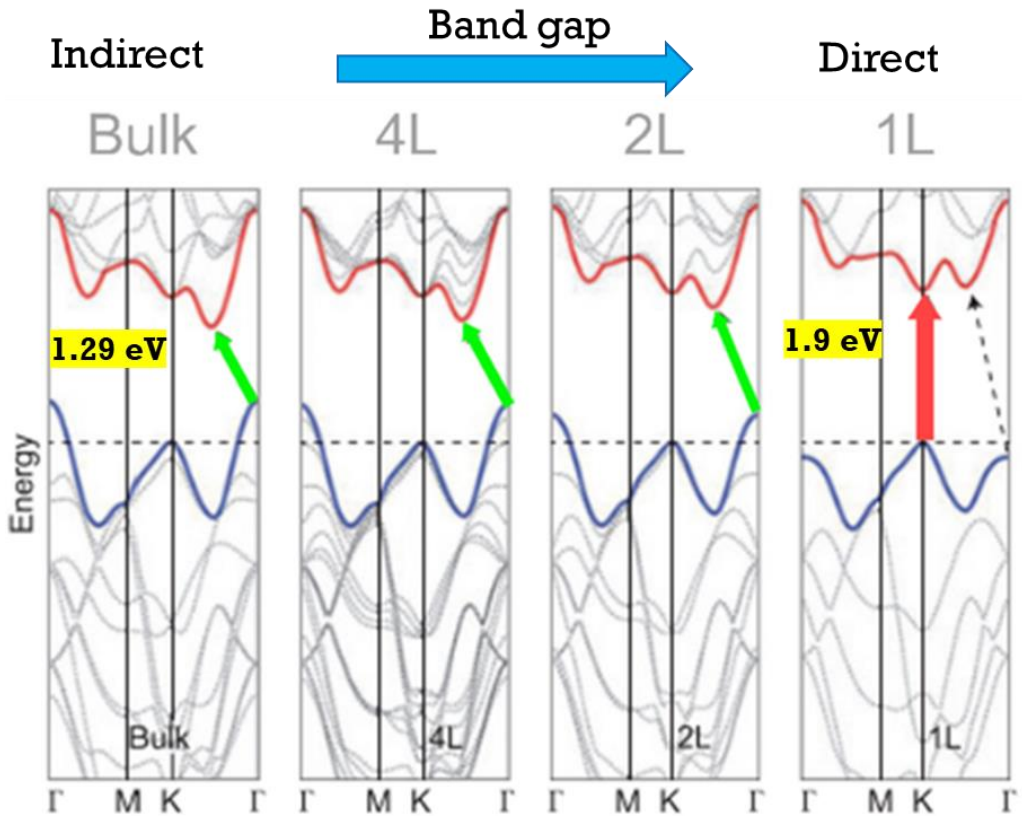

Figure 1.9. Electronic band structures of bulk, four-layer, two-layer, and single-layer MoS_2 (from left to right). Black arrows indicate the fundamental transitions. The horizontal dashed lines demonstrate the energy of the highest occupied states at the K point, which becomes the VBM in single layers. As the number of layers decrease, the energy at the Γ point reduces, and becomes lower than K point state in single layers, leading to direct gap transition. [53]

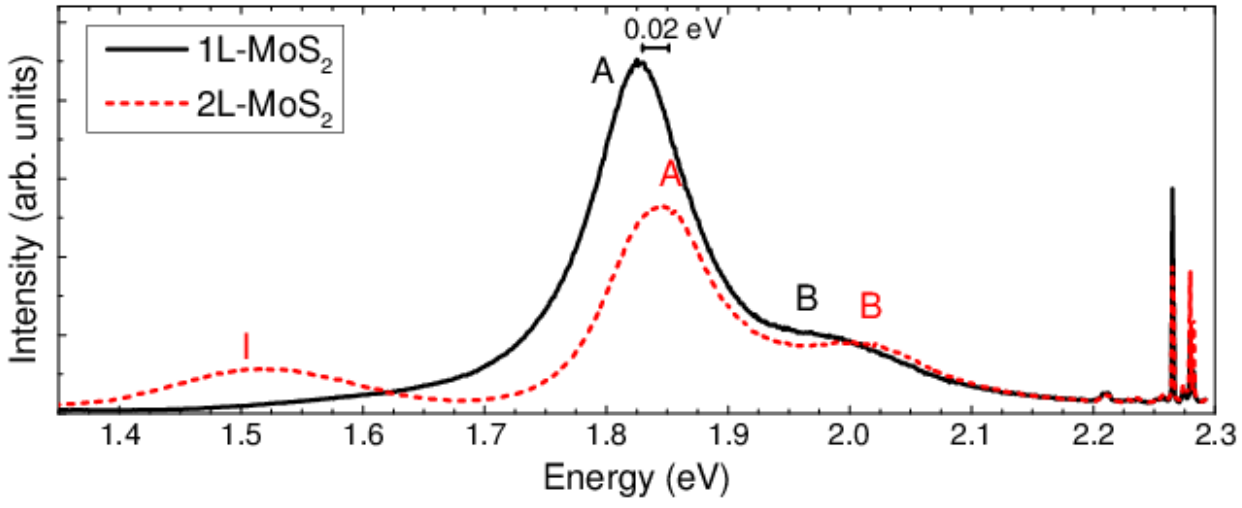

Figure 1.10 Photoluminescence spectra of mono-and bilayer MoS_2 on Si/SiO_2 substrates at an excitation energy of 2.33 eV. The sharp peaks just below 2.3 eV are the Raman modes[54].

Molybdenum disulfide (MoS_2) exhibits exceptional electrical and optical properties due to its unique electronic structure [32,55]. In bulk form, MoS_2 is an indirect bandgap semiconductor, meaning that the transition from the valence band to the conduction band requires energy transfer through a

phonon, or lattice vibration. However, when MoS_2 is thinned to the monolayer regime, it undergoes a remarkable transformation becoming a direct bandgap semiconductor. This direct bandgap property is crucial for optoelectronic applications, as it allows for efficient absorption and emission of light.

The transition from indirect to direct bandgap in monolayer MoS_2 arises from two factors:

- Quantum confinement effects: As the thickness of MoS_2 is reduced, the energy levels of the electrons are confined, leading to a shift in the band structure (Figure 1.9).
- Interaction of S orbitals: The p_z orbitals of S atoms from neighboring layers interact, contributing to the indirect bandgap in bulk MoS_2. However, in the monolayer, these interactions are significantly reduced, resulting in the direct bandgap at the K point [53,54,56,57].

The direct bandgap at the K point in monolayer MoS_2 is further influenced by spin-orbit coupling (SOC), which splits the valence band maximum (VBM) at the K point into two distinct energy levels [58–60]. This splitting has significant implications for the valley-dependent properties of MoS_2, which are highly sought after for potential applications in valleytronics.

The electronic structure of molybdenum disulfide (MoS_2) has a significant impact on its optical properties. In the optical absorption and reflectance spectra of MoS_2, three primary peaks are observed within the energy range of ~1.8 to 3eV as shown in Figure 1.10:

- Peaks A and B: These low-energy peaks correspond to excitonic transitions at the K point from the spin-split bands. Their positions are relatively insensitive to the number of MoS_2 layers.
- Peak I: This higher-energy peak is associated with interband transitions around the Γ point [61–63].

Due to the transition from an indirect to a direct bandgap in the monolayer regime, photoluminescence (PL) properties exhibit a strong dependence on the number of layers. In bulk MoS_2, PL is negligible, but it emerges as the number of layers decreases, approaching the monolayer [53,54].

Mak et al. [54] demonstrated a remarkable enhancement in the quantum yield (QY) of PL for monolayer MoS_2 compared to the bulk case. The PL spectra for the monolayer exhibited a single peak at 1.90 eV, corresponding to the direct optical bandgap. For few-layers MoS_2, three peaks were observed: two (A and B) related to the direct gap and a third (I) attributed to the indirect bandgap.

The splitting of the valence band at the K point due to interlayer coupling and spin-orbit coupling (SOC) gives rise to two excitons associated with peaks A and B.

Adsorption of gases on monolayer MoS_2 can enhance the PL due to charge transfer between MoS_2 and the adsorbed molecules. This PL modulation is reversible, offering potential applications in gas sensing devices [64]. The combination of the optical direct bandgap and semiconducting properties of MoS_2 makes it a promising material for optoelectronic applications, including photodetectors and light-emitting devices [32,47].

The number of layers in molybdenum disulfide (MoS_2) has a significant impact on its Raman spectra and electronic bandgap properties.

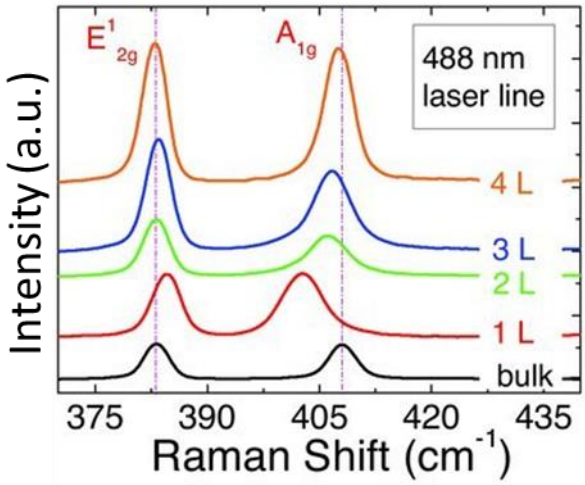

Figure 1.11 Raman spectra of different locations with various thicknesses. The left and right dashed lines indicate the positions of the E^1_{2g} and A_{1g} peaks in bulk MoS_2 respectively [65].

- Raman Spectroscopy: The difference in Raman shift between the two characteristic modes E^1_{2g} and A_{1g} varies with the number of layers, providing a convenient method for determining layer thickness as shown in Figure 1.11 [65].
- Electronic Bandgap: Monolayer MoS_2 exhibits a larger electronic bandgap than its optical bandgap due to its high exciton binding energy [47,56,59,62,66]. Theoretical calculations estimate the electronic bandgap for monolayer MoS_2 to be around 2.80 eV, while experimental measurements using scanning tunneling spectroscopy (STS) have reported a value of 2.16 eV for monolayer MoS_2 on graphite [67,68].
- Substrate Effects: The substrate upon which MoS_2 is deposited can influence the value of its electronic bandgap. Theoretical studies suggest that the bandgap tends to decrease as the environmental dielectric constant increases [67]. This effect could be exploited for bandgap tuning in Field-Effect Transistors (FETs).

Monolayer molybdenum disulfide (MoS_2) has emerged as a promising material for next-generation ultrathin electronic devices due to its unique bandgap and promising electrical properties [32,47].

- Theoretical Carrier Mobility: Theoretical calculations predict a room-temperature carrier mobility of approximately 410 cm2V-1s-1 for monolayer MoS_2, limited by optical phonon scattering (Figure 1.11) [69].
- Experimental Carrier Mobility: Early experiments on MoS_2 field-effect transistors (FETs) demonstrated mobilities ranging from 0.5 to 3 cm2V-1s-1 [47,57].
- Dielectric Engineering: Dielectric engineering using high-κ dielectric materials can significantly enhance carrier mobility [69,70].
- Ambipolarity: MoS_2 FETs can be fabricated in n-type, p-type, or ambipolar configurations [32,47].
- High-Performance FETs: Radisavljevic et al. demonstrated an n-type MoS_2 FET using HfO2 as the gate dielectric, achieving high current on/off ratio (>108), room-temperature mobility of 200 cm2V-1s-1, and a subthreshold swing of 74 mV per decade [20].

Molybdenum disulfide (MoS_2) exhibits unique properties arising from its symmetry, particularly the presence or absence of an inversion center.

- Even-Layered MoS_2**:** Few-layer MoS_2 with an even number of layers possesses inversion symmetry.
- Odd-Layered MoS_2**:** Few-layer MoS_2 with an odd number of layers lacks inversion symmetry [32].
- Spintronics and Valleytronics Applications: Monolayer MoS_2, lacking inversion symmetry, exhibits a combination of spin-orbit coupling (SOC) and valley-coupling, making it a promising material for spintronics and valleytronics applications [46,48].
- Spin Splitting: SOC in monolayer MoS_2 induces a spin splitting of the valence band, with a value around 150 meV [55,58,60,71].
- Piezoelectricity: Monolayer and odd-layered MoS_2 exhibit piezoelectricity due to the absence of inversion symmetry, while even-layered and bulk MoS_2 do not [72].
- Strain Engineering: Applying strain, particularly uniaxial tensile strain, can induce a decrease in the optical bandgap and a transition from direct to indirect bandgap in MoS_2 [61,73–75].
- Gating: Gating using electric fields can modulate the electronic properties of MoS_2.
- Alloying: Alloying MoS_2 with other materials can alter its bandgap and electronic characteristics.

- Heterostructures: Combining MoS_2 with other materials to form heterostructures can introduce new functionalities and enhance its properties.
- Nanosheet Dimensions: Modifying the dimensions of MoS_2 nanosheets can influence their electronic properties.
- Defects and Doping: Introducing defects or intentional doping can tailor the electronic properties of MoS_2 [61,76].
- Edge Effects: The edges of MoS_2 nanosheets play a significant role in its properties, particularly in catalytic reactions. Different edge morphologies can exhibit distinct properties, such as metallic character or magnetism [77,78].

Despite their many promising properties, 2D materials still face several challenges that need to be addressed before they can be widely adopted in commercial applications. One of the primary challenges is developing an optimal, efficient, and scalable fabrication process. The synthesis of high-quality, pristine 2D material samples consistently and reliably is a complex task. Additionally, the introduction of new materials and fabrication techniques can be a lengthy and costly endeavor, requiring significant time and financial investments. Overcoming these challenges will require continued research and development efforts to refine existing fabrication methods, explore novel synthesis techniques, and optimize processing parameters. By addressing these limitations, researchers can pave the way for the widespread adoption of 2D materials in a variety of applications across various industries.

The distinction between a small incremental step and a groundbreaking advancement in technology can be difficult to discern at the moment. The invention of the field-effect transistor, initially perceived as a minor improvement, has revolutionized electronics. Similarly, the discovery of graphene, initially regarded as a mere curiosity, has sparked a revolution in materials science and related fields. Despite the remarkable properties of graphene and other 2D materials, their ultimate impact on society remains uncertain. To fully realize their potential, researchers must deepen their understanding of their properties and working principles, enabling the development of innovative applications and transformative technologies. The journey from a scientific curiosity to a societal impact is often a protracted and challenging one. Only time will tell whether 2D materials will follow a similar trajectory to the field-effect transistor, fundamentally altering the landscape of technology and shaping our future.

1.3 Aims and Goals of the Thesis:

The realm of nanotechnology has witnessed a surge of interest in two-dimensional (2D) materials, exemplified by the widespread applications of graphene. These materials hold immense promise for revolutionizing fields ranging from electronics to civil engineering (cementitious composites enable smarter functionality of buildings). While carbon-based structures like graphene and nanotubes have garnered significant attention, other elements, and compounds, such as molybdenum disulfide (MoS_2), offer exciting possibilities for the creation of novel 2D nanostructures.

A critical challenge lies in the design of stable configurations for these new MoS_2-based 2D nanostructures. While stable configurations are known for typical structures, predicting them for new designs remains an intricate task. This research proposes a new approach to address this challenge: the intelligent design of new 2D atomically stable MoS_2-based nanostructures with prescribed properties.

The cornerstone of this intelligent design approach is the utilization of bioinspired global optimization techniques, specifically memetic algorithms. These algorithms represent a recent frontier in evolutionary computation, and their power lies in their ability to synergistically combine the strengths of evolutionary algorithms (mimicking natural selection) with local improvement procedures. This synergy empowers memetic algorithms to excel at searching for new solutions, making them ideally suited for the task of designing stable and functional 2D nanostructures.

To achieve the goal of creating new stable nanostructures, the work uses a powerful computational tool in identifying configurations that possess minimal potential energy while adhering to additional constraints that guarantee the desired material properties of the structure. The efficacy of the methods employed within this work is meticulously evaluated using established techniques: LAMMPS, a software package for molecular dynamics simulations, and a custom-built Evolutionary Algorithm optimization software.

A crucial aspect of this research involves the accurate description of interatomic interactions within MoS_2 nanostructures. To achieve this, the Stillinger-Weber potential is employed. The optimization process itself will encompass two key steps. First, the distribution of MoS_2 atoms within a periodic cell is optimized by leveraging the aforementioned optimization technique and molecular simulations. Second, algorithms that are adept at avoiding entrapment in local optima is utilized to ensure the identification of the true global minimum energy configuration. The objective function guiding the optimization process will be tailored to either minimize energy or achieve a specific set of desired properties for the microstructure.

The research leverages LAMMPS for modeling MoS_2 flat structures. Notably, the optimization process is conducted using a bespoke intelligent bioinspired algorithm, which incorporates both evolutionary and conjugate gradient-based algorithms. While achieving a stable structure is a significant accomplishment, the research vision extends beyond this. It aspires to design structures that not only exhibit stability but also possess prescribed properties, such as specific stiffness characteristics or anisotropic/orthotropic behavior.

Molecular statics and dynamics simulations are integral to the success of this work. The accuracy of the atomic structure modeling has a profound impact on the functionality used during optimization. Validating and simplifying MoS_2 nanostructure models will provide invaluable input for the final designs and influence the overall computational cost associated with the design of these nanomaterials.

In essence, this research ushers in a new paradigm for the design of MoS_2-based 2D nanostructures. By harnessing the power of bioinspired optimization techniques, the work paves the way for the creation of novel materials with tailored properties, opening avenues for new advancements in the field of nanomaterial science.

1.3.1 Overview of the Proposed Technique

To illustrate the motivation behind this investigation and to give a basis for understanding the information in the following chapters, following is an overview of how an evolutionary process might serve as a natural framework for an intelligent design process.

1.3.2 Modelling Strength of Molybdenum disulfide (MoS_2)

Molybdenum disulfide (MoS_2) stands out with its impressive electronic and mechanical properties, making it a promising candidate for future devices. However, a major hurdle exists simulating MoS_2 is computationally expensive. Additionally, our knowledge of MoS_2's strength under different processing conditions is limited and the details of the modelling strength is discussed in chapter 3.

This research tackles these challenges with a two-fold approach, focusing on the mechanical response of monolayer MoS_2 and the influence of defects. The main goal is to understand how defects affect MoS_2's mechanical behavior and the mechanisms that strengthen pristine MoS_2. This knowledge is crucial for designing high-performance 2D MoS_2 devices.

The first step involves developing efficient models to accurately capture MoS_2's mechanical behavior. This is achieved in two stages. First, a detailed Molecular statics simulation is performed to gain a

fundamental understanding of how MoS_2 behaves at the atomic level. Then, using this knowledge, computationally efficient nanostructured models are built for further investigation of MoS_2-based systems.

The second stage explores the mechanical properties of MoS_2, particularly how defects within the monolayer structure affect its strength. Simulations are conducted on MoS_2 monolayers with randomly distributed defects at varying concentrations (0% to 25%). By analyzing the response of these structures, the research reveals a detrimental effect of defects on the material's elasticity, especially at higher defect concentrations. This information is valuable for developing design principles that create robust 2D MoS_2 devices with superior mechanical properties.

1.3.3 Evolutionary Algorithms in Design

Evolutionary algorithms have become a cornerstone of global optimization techniques. Inspired by the natural world and the process of evolution, these algorithms excel at finding global solutions across a vast search space. The core elements and mechanisms used within these algorithms mirror biological principles, creating a truly bioinspired approach.

The optimization process works on a population of potential solutions, often referred to as "individuals" with "chromosomes" that contain design variables. These variables, called "genes," are typically represented by floating-point numbers. The quality of each individual is evaluated using a "fitness function," which considers the objective function alongside any additional problem-specific factors.

Memetic algorithms take this approach a step further by combining the strengths of evolutionary algorithms with local improvement methods. These hybrid algorithms, sometimes called "hybrid evolutionary algorithms," leverage the global search capabilities of evolutionary techniques alongside targeted refinements from local optimization methods.

In this work, a memetic algorithm is implemented that couples a global evolutionary algorithm with a local conjugate gradient algorithm. The evolutionary algorithm remains the driving force, maintaining a population of potential solutions that evolves over time. Standard operators like mutation and crossover are employed when modification is necessary, and the selection process is also preserved. However, the local conjugate gradient algorithm steps in before fitness functions are calculated. It modifies the genes in each chromosome, subtly influencing the evolutionary algorithm's search process. This modification guides the evolutionary process towards optimal solutions by balancing exploration (finding new search areas) and exploitation (refinement around promising

solutions). This approach is particularly well-suited for problems with highly multimodal fitness landscapes, where traditional evolutionary algorithms might struggle to escape local optima.

chapter 4 delves deeper into the specifics of this memetic algorithm and its integration with molecular dynamics simulations using LAMMPS software.

1.3.4 Summary

In this introduction, a general flavor of the work motivating this thesis has been presented. The idea of EA optimization is discussed, and the short brief procedure of nano-level optimization is explained. The similarity between successful long term product development and Darwinistic evolution is motivation to investigate design methods based on an evolutionary principle. For this purpose, a heuristic search routine known as the evolutionary algorithm is introduced, and some indications of the potential for the use of evolutionary algorithms in design optimization are discussed. This provides the background for the application of evolutionary principles to the automated topological design of structures.

1.3.5 Scope of Thesis:

The objective of this doctorate project is to create a method for intelligent design of 2D nanostructures with prescribed properties based on molybdenum. The nanostructures obtained during the intelligent designed based on a memetic optimization process should have stable configuration (minimum energy) and subsequently study the mechanical properties of nanostructure for the prescribed properties (e.g., mechanical, and thermal properties of material).

The thesis covers the research that has been implemented over the course of Poland PhD degree at the information and computational sciences of IPPT, PAN and Mechanical Engineering division of Politechnika Slaska (SUT), Gliwice. It unfolds with summarizing the recent progress of the study of the structures, properties of monolayer MoS_2. These contents are the cornerstone for my following investigation, which set up the fundamental knowledge and indicate the gaps needed to be filled in this research field. Subsequently, the series of characterization techniques with molecular simulation and typical data processing methods employed in my research are introduced in Chapter 3, The detail can be found in corresponding published papers.

The general structure of my results is summarized in Figure 1.12. My work starts with the study of atomistic modelling monolayer MoS_2, based on the above literature review, it is clear that computational cost in modelling MoS_2 is a fundamental challenge, and the current knowledge on the mechanical properties of MoS_2 under various processing conditions (e.g. defects, inclusions and temperature) is limited. Therefore, the objective of the thesis is to develop computationally efficient

molecular-based models to analyze the mechanical stiffness of pristine and defective MoS_2. In order to achieve this objective, a two-step approach is employed:

First, a comprehensive MD simulation studies is conducted to gain insight basic understanding of the mechanics of MoS_2 mechanism of monolayer MoS_2 by modeling performed on suspended free-standing membrane with comparison to experiment and to explore the influence of structural defects on the mechanical properties of monolayer MoS_2 by modelling monolayer MoS_2 membranes with defects and simulating the same.

Then, using this knowledge, Evolutionary optimization is used to design computationally efficient molecular-based MoS_2 nanostructures models that are developed based on prescribed mechanical properties. The purposes of this work are to establish practical synthesis strategies, which can design MoS_2 monolayers for further property investigations, and to have a universal and in-depth understanding of the design and optimization process, which has a potential of being expanded to other 2D materials.

The research focus to understanding the atomic structure of monolayer MoS_2 by employing the large-scale atomistic massive molecular parallel simulator (LAMMPS), which models and stimuli to modify the intrinsic periodicity of the MoS_2 lattice, thus tailoring its properties from the bottom level. defects were first investigated by introducing a mild concentration of S vacancies, which are prone to migrating and aggregate into vacancies lines (Chapter 3). Both lattice distortions for defects and anti-site defects have been modelled with LAMMPS. The calculations were conducted to predict the mechanical properties evolution as the defects extend and broaden. Prolonged focus of defects triggers the voids in suspended monolayer MoS_2, which provides an opportunity to design the material behavior down to the atomic level (Chapter 4). Large-scale molecular dynamics (MD) simulations were applied to predict the toughness of defective monolayer MoS_2 compared with that of pristine.

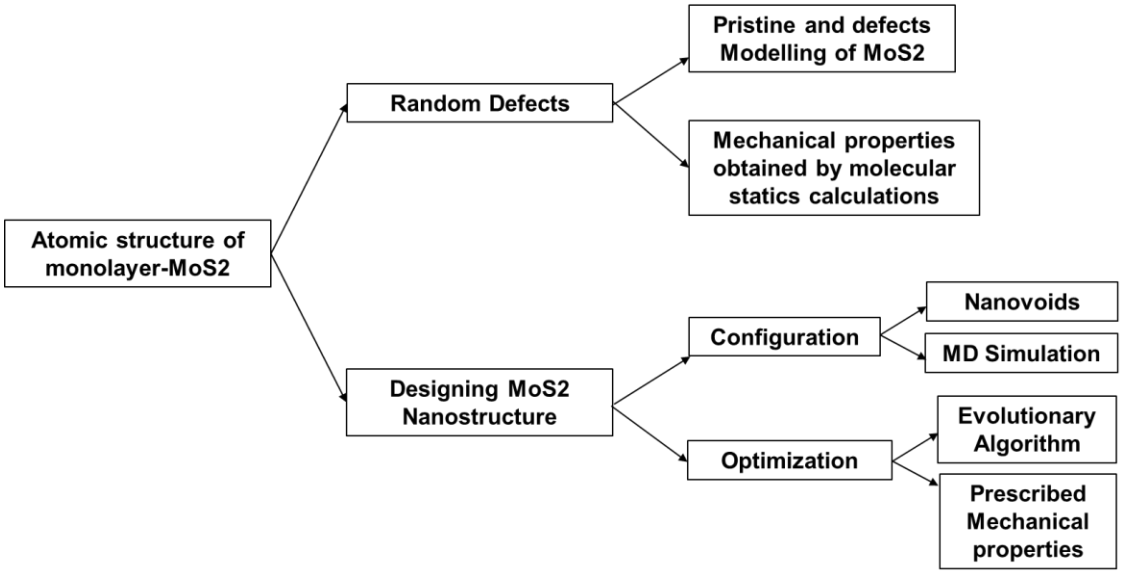

Figure 1.12. Schematic illustration showing the overall structure of my thesis.

Chapter 2

Molecular Dynamics Simulations

Molecular Dynamics (MD) is a computer simulation method that uses the principles of mechanics to track the time evolution of a system of interacting atoms. The interactions between the atoms are described using molecular mechanics potential fields. MD was first developed in the late 1950s [79] and has since become a widely used tool in many fields, including materials science, chemistry, biophysics, and drug discovery. One of the most popular MD simulators is Large-scale Atomic/Molecular Massively Parallel Simulator (LAMMPS), which is designed to simulate large-scale systems and can run in parallel on high-performance computing architectures. OVITO is a software that is used to visualize and analyze MD simulations. By using MD, researchers can gain insights into the behavior and properties of molecular systems, such as the motion of atoms, energy transfer, and structural changes. MD simulations have been used to study a wide range of phenomena, including the properties of materials, the behavior of biomolecules, and the mechanism of chemical reactions.

2.1 Molecular Dynamic simulations Basic Theory

2.1.1 Equation of Motion

Molecular dynamics can be divided into two basic steps.

Step 1: Calculate the interacting forces between the atoms.

The first step in an MD simulation is to calculate the forces acting on each atom in the system. These forces are determined by the potential energy of the system, which is typically described by a molecular mechanics (MM) potential field. The MM potential field considers the various types of interactions between atoms, such as bond stretching, bond bending, and van der Waals interactions.

Step 2: Integrate Newton's equations of motion.

Once the forces acting on each atom have been calculated, the next step is to integrate Newton's equations of motion to update the positions and velocities of the atoms. Newton's second law of motion states that the force acting on an object is equal to the mass of the object times its acceleration. The interacting force acting on atom i, denoted as f_i, is obtained from the gradient of the molecular mechanics' potential field. The force acting on atom i (f_i) is given by [80]

$$f_i = \frac{-\partial E_i}{\partial r_i} \tag{2.1}$$

where E_i and r_i are the potential energy and position of atom i, respectively. Potential energy of atoms is given by a molecular mechanics potential field. The specific mathematical formulation for the force calculation depends on the chosen molecular mechanics potential field. Some common MM potential fields include Lennard Jones (LJ), Reactive force fields (ReaxFF), Morse and Stillinger Weber (SW). These potential fields typically incorporate parameters that describe the interactions between different atom types, including bond stretching, angle bending, torsional rotation, and non-bonded interactions such as van der Waals forces and electrostatic interactions. The mathematical formulation for the force calculation for some common types of interactions are shown in Table 2.1:

Table 2.1 Examples of interatomic interactions

Interaction type	**Mathematical formulation**
Bond stretching	$f=-k(r-r_0)$
Angle bending	$f=-k(\theta-\theta_0)$
Torsional rotation	$f=-k(\phi-\phi_0)$
Non-bonded interactions	$f=-C/r^6+D/r^8$

where:

- f is the force, k is the force constant, r is the distance between the atoms, r_0 is the equilibrium bond length, θ is the angle between the atoms, θ_0 is the equilibrium angle, ϕ is the dihedral angle, ϕ_0 is the equilibrium dihedral angle, C and D are constants that depend on the atom types.

Once the interacting forces have been determined, they are used in the integration of Newton's equations of motion. This integration scheme allows for the prediction of the positions and velocities of the atoms over time. By iteratively updating the atom positions based on the calculated forces, the trajectory of the system can be simulated and analyzed. Overall, the combination of determining interacting forces from a molecular mechanics potential field and integrating Newton's equations of motion enables the simulation of molecular dynamics, providing insights into the behavior and properties of the system under study.

There are several molecular mechanics (MM) potential fields available that are suitable for simulating various systems. In Section 2.3, an overview of these potential fields is provided. Once the force acting on an atom is determined, it is possible to calculate the acceleration of the atom using Newton's second law of motion.

$$f_i = m_i \frac{\partial^2 r_i}{\partial t^2} = m_i a_i \tag{2.2}$$

where m_i, r_i, and a_i are the mass, position, and acceleration of atom i, respectively.

A system of atoms is allowed to move under these accelerations for a time period called time step. The new positions and velocities of the atoms are obtained using a numerical integration method such as velocity Verlet method [80]. According to the velocity Verlet method,

$$\begin{aligned} v\left(t_0 + \tfrac{\Delta t}{2}\right) &= v(t_0) + a(t_0)\tfrac{\Delta t}{2} \\ r(t_0 + \Delta t) &= r(t_0) + v\left(t_0 + \tfrac{\Delta t}{2}\right)\Delta t, \\ v(t_0 + \Delta t) &= v\left(t_0 + \tfrac{\Delta t}{2}\right) + a(t_0)\Delta t, \end{aligned} \tag{2.3}$$

Where r, v, *and* a, are the position, velocity, and acceleration of an atom, respectively; t_0 is the initial time; Δt is the time step. Variation in r and v with Δt is graphically presented in Figure. 2.1. In molecular dynamics (MD) simulations, controlling temperature and pressure is crucial to mimic real systems that are under constant temperature or pressure conditions. Temperature control is typically achieved by modifying the velocities of atoms, while pressure control involves adjusting the size of the simulation box. A review of commonly used techniques to control temperature and pressure follows next.

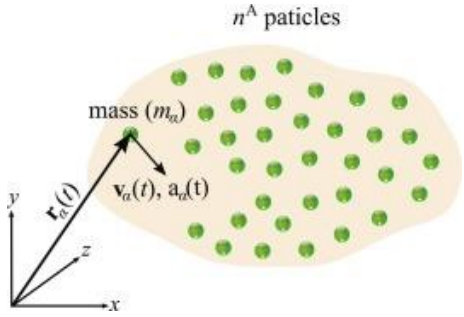

Figure 2.1 Change in positions and velocities of atoms with time.

2.1.2 Thermostat

The temperature of a system of atoms is defined as the average kinetic energy of all particles. The instantaneous temperature can be given as

$$T = \frac{1}{N_f K_B} \sum_{i,\alpha} m_i (v_i^{\alpha})^2 \tag{2.4}$$

where, N_f is the total translational degrees of freedom of the system, k_B is Boltzmann's constant, m_i is the mass of atom i and v^{α}_i is the velocity of atom α *in* i direction. The value of α can be 2 or 3 depending on the dimensionality of the system. It is not possible to keep the temperature at a fixed value during the simulation due to the fluctuations in velocities. Therefore, only the average value of temperature can be maintained at a constant value during simulations. The temperature of a system depends only on the velocities of atoms as given in Eq. (2.4). Therefore, the temperature of a system can be controlled by scaling the velocities of atoms, which is achieved using a thermostat. Anderson, Berendsen, and Nose-Hoover thermostats are the most commonly used thermostats.

Andersen thermostat: The Andersen [81] thermostat is a stochastic thermostat that works by randomly selecting a particle and assigning it a new velocity drawn from the Maxwell-Boltzmann distribution corresponding to the desired temperature. This method ensures that the system's temperature is maintained at the desired value. However, the Andersen thermostat can be computationally expensive due to the need for random selection and velocity updates for each particle at every time step [82].

Berendsen thermostat: The Berendsen thermostat [83] is a deterministic thermostat that works by scaling the velocities of all atoms in the system proportionally to control the temperature. By adjusting a coupling parameter, the velocities are rescaled such that the total kinetic energy of the system remains constant. The Berendsen thermostat is easy to implement and widely used in MD simulations, especially for equilibration and initial relaxation stages.

Nose-Hoover thermostat: The Nose-Hoover thermostat is considered to be one of the best thermostats [84]. It uses a friction factor (μ) to modify the equation of motion so that the system temperature converges to the desired temperature. The Nose-Hoover thermostat is more computationally expensive than the Berendsen thermostat, but it is also more stable and accurate [85–87]. The μ is defined as

$$\frac{d\mu(t)}{dt} = \frac{N_f K_B}{Q}(T(t) - T_o) \tag{2.5}$$

where T_0 and $T(t)$ are the desired and the current temperatures, respectively; Q is the effective mass of the thermostat, which determines the strength of thermostat, and is given as

$$Q = N_f K_B T_0 \tau_T^2 \tag{2.6}$$

where τ_T is the specified time constant for temperature fluctuations. The value of τ_T is generally in the order of hundred-time steps to achieve a smooth temperature transition.

The modified Newton's equation of motion is given by,

$$a = \frac{f_t}{m} - \mu(t)v(t) \tag{2.7}$$

Table 2.2 The key differences between the three thermostats:

Thermostat	**Type**	**Advantages**	**Disadvantages**
Andersen	Stochastic	Simple to implement	Can be computationally expensive
Berendsen	Deterministic	Easy to implement	Less accurate than Nose-Hoover
Nose-Hoover	Deterministic	Most accurate	More computationally expensive than Berendsen

2.1.3 Pressure Regulation

The pressure of a system of atoms is defined as

$$P_{ij} = \frac{1}{V}\sum_{\alpha}\left[\sum_{\beta=1}^{N}\left(r_i^{\beta} - r_i^{\alpha}\right)f_j^{\alpha\beta} + m^{\alpha}v_i^{\alpha}v_j^{\alpha}\right] \tag{2.8}$$

where, (i, j) are directional indices and β is a number, assigned to the neighboring atoms that goes from 1 to the number of neighboring atoms N; r_i^{α} is the position of atom α along the direction i, and

$f_j^{\alpha\beta}$ is the force along direction j on atom α due to atom β; $m^\alpha v_i^\alpha$ are the mass and velocity of atom α, respectively. V is the total volume of the system.

The Berendsen barostat [83] and the Nosé-Hoover barostat [88] are two commonly used methods to control pressure in molecular dynamics simulations.

The Berendsen barostat is a simple and widely used method that scales the simulation box dimensions to control the system pressure. It operates by adjusting the size of the simulation box to achieve the desired pressure. However, the Berendsen barostat is known to be less accurate and physically realistic compared to other methods, as it does not fully sample the correct statistical ensemble and may lead to artificial equilibration behavior.

On the other hand, the Nosé-Hoover barostat is a more sophisticated and accurate method based on extended Hamiltonian dynamics. It introduces additional degrees of freedom to the system to control the pressure. The Nosé-Hoover barostat maintains the system pressure at the desired value by periodically rescaling the momenta of the fictitious degrees of freedom. This approach more closely follows the statistical mechanics principles and provides a more accurate sampling of the isothermal-isobaric ensemble.

Both barostat have their advantages and limitations (Table 2.3). The choice of barostat depends on the specific requirements of the simulation, such as the desired accuracy, computational efficiency, and the nature of the system being studied. Researchers often select the most appropriate barostat based on their specific needs and the trade-offs between accuracy and computational cost.

Table 2.3 Advantages and disadvantages of each barostat

Barostat	Advantages	Disadvantages
Berendsen	Simpler, more computationally efficient	Less accurate, more likely to exhibit artificial equilibration behavior
Nosé-Hoover	More accurate, better sampling of statistical ensemble, less likely to exhibit artificial equilibration behavior	More complex, less computationally efficient

2.2 Statistical Ensembles

Statistical ensembles represent collections of possible states of a system under specific macroscopic constraints, such as fixed temperature and pressure. These constraints dictate the characteristics and behavior of the system in statistical equilibrium. The microcanonical ensemble (NVE) is used when the number of atoms (N), volume (V), and energy (E) of the system are kept constant. This ensemble is particularly useful for studying isolated systems where no exchange of energy or particles occurs with the surroundings. In contrast, the canonical ensemble (NVT) is employed when both the number of atoms and the volume are fixed, but the system is allowed to exchange energy with the surroundings. This is useful for simulating systems under constant volume and temperature conditions, which is often encountered in laboratory experiments. Lastly, the isothermal-isobaric ensemble (NPT) is used when both the temperature and pressure are fixed, making it suitable for simulating systems at a specific temperature and pressure, resembling many real-world experimental conditions. Figure 2.2 graphically demonstrate the characteristics of NVE, NVT, and NPT ensembles.

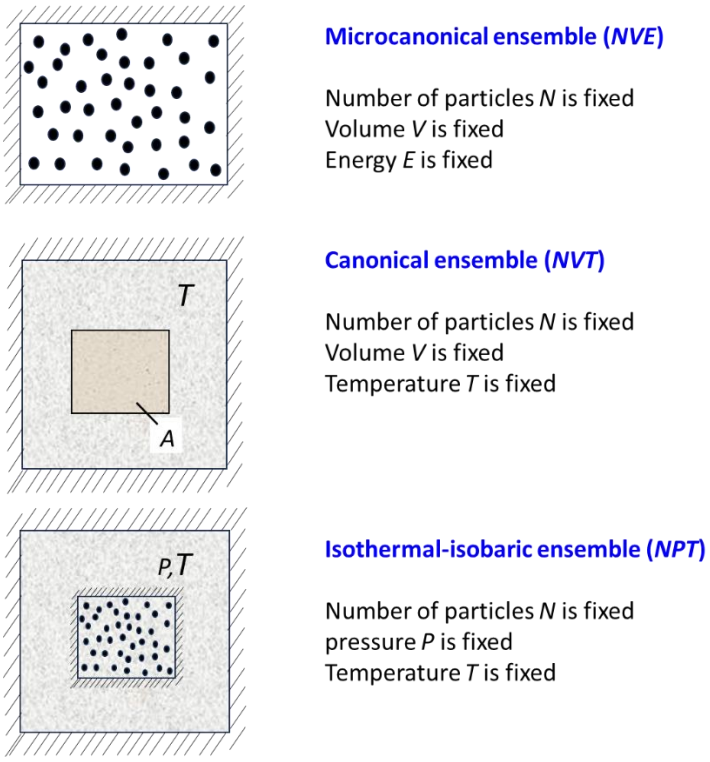

Figure 2.2 Graphical representation of the microcanonical (NVE), the canonical (NVT), and the isothermal-isobaric (NPT) ensembles [91].

In NPT ensemble, temperature and pressure can be controlled by modifying the equation of motion according to the Nosé-Hoover thermostat and barostat [89,90]. The resulting system of equations of NPT ensemble can be expressed as

$$\frac{d\mu(t)}{dt} = \frac{1}{\tau_T^2}\left(\frac{T(t)}{T_o} - 1\right),$$

$$\frac{d\eta(t)}{dt} = \frac{1}{N_f K_B T_0 \tau_P^2} V(t)[P(t) - P_0],$$

$$\frac{dV(t)}{dt} = [3\eta(t)]V(t), \tag{2.9}$$

$$\frac{dr(t)}{dt} = v(t) + \eta[r(t) - R_0],$$

$$\frac{dv(t)}{dt} = \frac{f(t)}{m} - [\mu(t) + \eta(t)]v(t),$$

where, μ is the friction factor to modify the equation of motion; T_0 and $T(t)$ are the desired and current temperatures, respectively; τ_T is the time constant for temperature fluctuations. P_0 and $P(t)$ are the instantaneous and desired pressures, respectively; τ_P is the time constant for pressure fluctuations; η is the volume scaling factor; R_0 is the center of mass of the system; $f(t)$ is the force acting on an atom, which is calculated from the gradient of the potential energy as given in (Eqn. 2.1), where the potential energy is obtained from a potential field.

2.3 Stillinger Weber Potential:

A potential field, also known as a force field, is a mathematical representation of the potential energy of a system of interacting atoms in molecular dynamics (MD) simulations. It is a crucial component of MD simulations as it determines the forces between atoms, which in turn govern their movements and interactions. In a potential field, various parameters such as bond lengths, bond angles, dihedral angles, and non-bonded interactions (van der Waals and electrostatic forces) are defined based on empirical data and/or quantum mechanical calculations. These parameters are usually derived from experimental data and theoretical calculations and are often optimized to reproduce specific properties or behaviors of real materials. The accuracy of the MD simulation results heavily relies on the accuracy of the potential field used in the simulation. If the potential field accurately describes the interactions between atoms, the simulation can provide meaningful and reliable insights into the behavior of the system being studied. On the other hand, an inaccurate or poorly parameterized potential field can lead to unrealistic or misleading simulation results.

The Stillinger-Weber (SW) potential is a widely used empirical interatomic potential model for describing the interactions between atoms in certain materials. It was introduced by Frank H. Stillinger and Thomas A. Weber in 1985 and has been applied to various systems, including semiconductors, metals, and covalent-bonded materials like silicon and diamond.

The SW potential is a many-body potential, meaning it accounts for interactions between more than two atoms at a time (one-, two-, and three-body terms). It is typically used to study materials with tetrahedral bonding configurations, such as silicon-based materials and some transition metal dichalcogenides (TMDs) like MoS_2.

The general form of the Stillinger-Weber potential is given by:

$$V_{SW} = \sum \left[Ae^{(-\lambda r_{ij})} - Be^{(-2\lambda r_{ij})} + \frac{q_{ij} * q_{ji}}{r_{ij}} \right] \quad (2.10)$$

where:

- A, B, and λ are fitting parameters that determine the strength and range of the interactions, r_{ij} is the distance between atoms *i* and *j*, q_{ij} and q_{ji} are the charges of atoms *i* and *j*, respectively.

The first two terms represent the short-range repulsive and attractive forces, while the third term represents the Coulombic interaction between charges. The Stillinger-Weber potential has been used in molecular dynamics simulations to study the mechanical, thermal, and electronic properties of materials, particularly those with tetrahedral bonding structures.

2.3.1 Stillinger Weber (SW) for MoS_2:

Several efforts have been made to obtain the parameters of SW potential for MoS_2 from different experiments and purely atomistic simulations. The parameters of SW potential are found by fitting to the experimentally obtained phonon spectrums [91], the energies obtained from molecular dynamics simulations based on valence force-field [92], the lattice geometry, elastic constants and phonon frequencies obtained from First Principal calculations [93], and the lattice geometry and atomic forces obtained from ab-initio molecular dynamics simulations [94].

This study focuses on investigating the mechanical properties of pristine and defective monolayer MoS_2 structures, including their relaxation behavior, using molecular static simulations. The SW potential considers all possible interactions between Mo and S atoms [93,94]. It is a many-body potential, consisting of one-, two-, and three-body terms, and has been well-fitted to accurately represent monolayer MoS_2. The main goal of this work is to obtain the elastic constants of monolayer MoS_2 through molecular static simulations. The accuracy of the computed results depends on the parameters used in the simulation. Therefore, the study uses well-parameterized molecular simulation techniques that can effectively describe a variety of bulk material properties. By understanding the

physical properties and having accurate interatomic potentials, researchers can gain insights into the behavior of monolayer MoS_2 and potentially control these properties for specific applications.

The bond interaction by two-body interaction acts towards the bond deformation while the three-body interaction conducts itself towards the angular rotation. The total potential of a system ϕ_{tot} can be written as

$$\phi_{tot} = \sum_i \sum_{i<j} Q_2(r_{ij}) + \sum_i \sum_{j \neq i} \sum_{k>j} Q_3(r_{ij}, r_{ik}, \alpha_{ijk}) \tag{2.11}$$

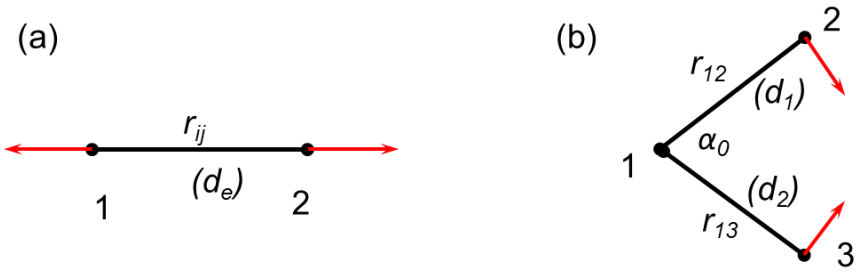

Figure 2.3 Two typical interactions in covalent materials. Each interaction term is described using the SW potential. (a) Two-body bond stretching interaction. (b) Three-body angle bending interaction. Atom moving directions are depicted by red arrows. r_{ij}, r_{12} and r_{13} are the distances between particles, while d_e, d_1 and d_2 are the bond length, respectively.

The two-body interaction potential, as shown in Figure 2.3, Q_2 takes the following form,

$$Q_2(r_{ij}) = X_{ij}\left(\frac{Y_{ij}}{r_{ij}^4} - 1\right) e^{\left(\frac{\sigma_{ij}}{r_{ij} - r_{ij}^{max}}\right)} \tag{2.12}$$

The three-body interaction potential Q_3 in Equation (2.11) is modeled as

$$Q_3(r_{ij}, r_{ik}, \alpha_{ijk}) = Z_{ijk} e^{\left(\frac{\sigma_{ij}}{r_{ij} - r_{ij}^{max}} + \frac{\sigma_{ik}}{r_{ik} - r_{ik}^{max}}\right)} * \left(cos\alpha_{ijk} - cos\alpha_{0,ijk}\right)^2 \tag{2.13}$$

where exponential function gives a smooth decay of the potential to zero at the cut-off, which is essential to save the energy. Q_2 and Q_3 represent the two body (bond stretching) and three body (bond bending) interactions. The r_{ij}, r_{ik} and α_{ijk} are the pair separations and angle between the separation on atom i respectively. The potential parameters are X, Y, Z, σ, along with r^{max} cutoff radii and

equilibrium angles and they rely upon on the atoms interacting with each other, for instance, X_{ij} is the parameter for X for the pairwise interaction between atom i of category I and atom j of category J.

There are five unknown geometrical parameters, i.e., Y_{ij} and σ_{ij} in the two-body Q_2 term and σ_{ij}, σ_{ik}, and α_0 in the three-body Q_3 term, and two energy parameters ι and υ.

The parameters Y_{ij} and σ_{ij} in Q_2 can be described as

$$\sigma_{ij} = \frac{-4Y_{ij}(d_e - r_{max})^2}{Y_{ij}d_e - {d_e}^5} \tag{2.14}$$

where d_e is the equilibrium bond length from experiments. Hence, there is only one free geometrical parameter left in Q_2. In other words, (Eqn 2.14) ensures that the bond has an equilibrium length of d_e and the Q_2 interaction for this bond is at the energy minimum state at the equilibrium configuration.

The energy parameters X_{ij} and Z_{ij} in the SW potential are.

$$X_{ij} = \frac{{Z_{ij}}_{r_{ij}}}{\varsigma e^{\left[\frac{\sigma_{ij}}{d_e - r_{ij}^{max}}\right]}} \tag{2.15}$$

and

$$Z_{ij} = \frac{{Z_{ij}}_{\alpha} d_1 d_2}{2sin^2\alpha_0 e^{\left[\frac{\sigma_{ij}}{d_1 - r_{12}^{max}} + \frac{\sigma_{ik}}{d_2 - r_{13}^{max}}\right]}} \tag{2.16}$$

where the coefficient ς in Eqn 2.15 is

$$\varsigma = \left[\frac{\sigma_{ij}}{\left(d_e - r_{ij}^{max}\right)^2}\right]^2 \left(\frac{Y_{ij}}{r_{ij}^4}\right) + \left[\frac{2\,\sigma_{ij}}{\left(d_e - r_{ij}^{max}\right)^3}\right]^2 \left(\frac{Y_{ij}}{r_{ij}^4} - 1\right) + \left[\frac{\sigma_{ij}}{\left(d_e - r_{ij}^{max}\right)^2}\right]^2 \left(\frac{8Y_{ij}}{d_e^5}\right) + \left(\frac{20Y_{ij}}{d_e^6}\right) \tag{2.17}$$

The bond length of the arms for the angle are d_1 and d_2, which are from experiments or other theoretical calculations.

In the SW potential, bond stretching interaction is described by (Eqn 2.12), and angle bending interaction is described by (Eqn 2.13). The potential parameters are determined in three steps:

1. the interaction cut-offs (r_{ij}^{max}, r_{12}^{max}, *and* r_{13}^{max}) are determined geometrically by the equilibrium configuration of the material. The bond length (d_e, d_1, and d_2) and the angle (α_0) are also from the experiment or other theoretical calculations.

2. the geometrical parameters σ_{ij} in the two-body term and σ_{ij} and σ_{ik} in the three-body term are determined by Equation (2.14), by assuming that each two-body SW term is at equilibrium separately.

3. the energy parameters (X_{ij} and Z_{ij}) are determined by Eqn. 2.15 and 2.16, based on the Valence-force-field (VFF) model [95].

The above derivation shows that there is no constraint imposed on the parameter Y_{ij} in the linear regime. The only condition for χ to satisfy is that $Y_{ij} < d_e^4$, so that $\sigma_{ij} > 0$.

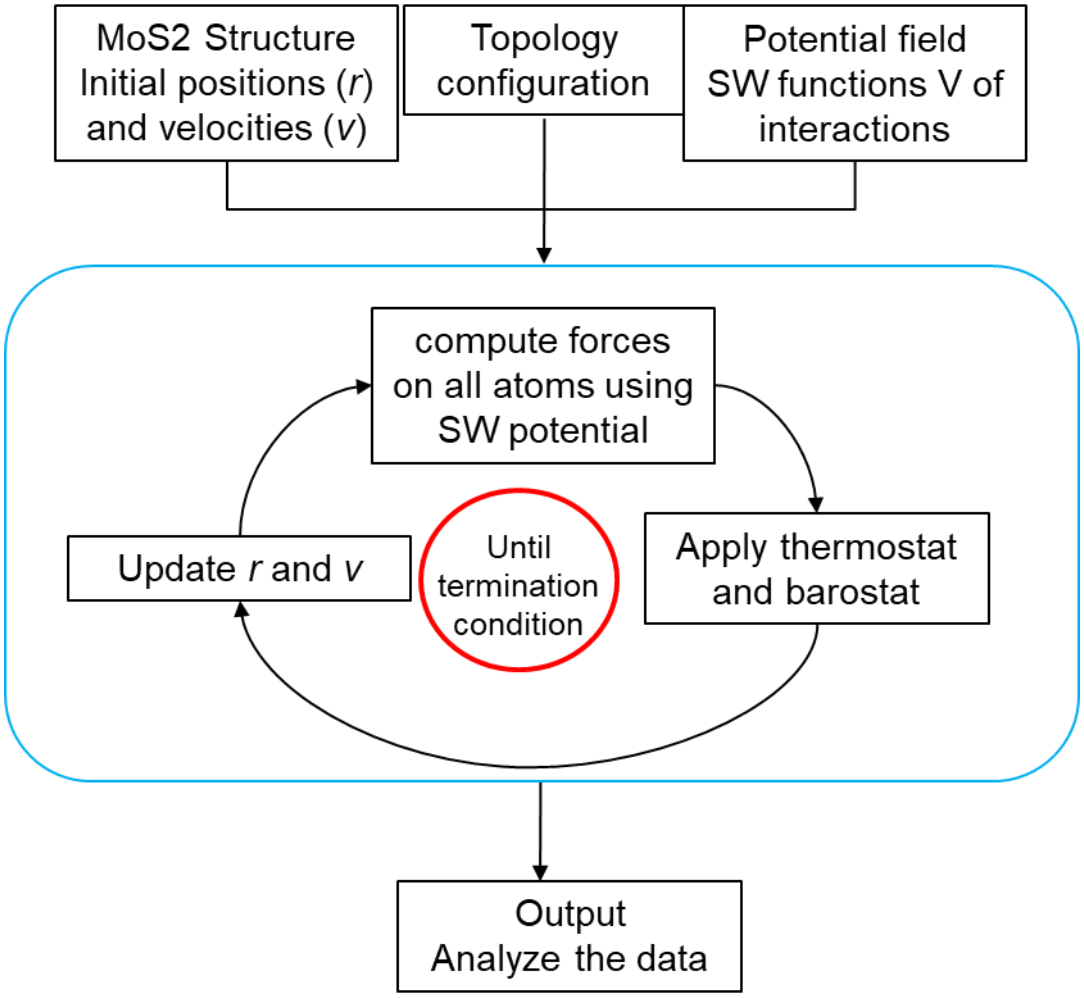

Figure 2.4 Graphical representation of the MD simulation procedure.

Figure 2.4 graphically demonstrates the procedure of Molecular Dynamics (MD) simulation. In MD simulations, the initial positions of atoms are defined such that they are slightly away from their known equilibrium positions. This initial displacement allows the atoms to explore different configurations and eventually reach their global equilibrium positions during the relaxation period. Additionally, the initial velocities of atoms are typically assigned randomly to simulate the thermal motion of the atoms at the desired temperature. However, the velocities are later rescaled by the thermostat during the simulation to achieve and maintain the desired temperature throughout the simulation.

The MD simulation loop, as shown in Figure 2.4, continues to run until a termination condition is met. The termination condition is often set as the number of iterations or time steps specified for the

simulation. During each iteration, the positions and velocities of the atoms are updated based on the equations of motion, which are typically Newton's equations of motion in classical MD simulations. The simulation proceeds by calculating the forces acting on each atom based on the interactions defined by the interatomic potential, such as the Stillinger-Weber potential mentioned earlier. The forces determine how the atoms move, and the integration of the equations of motion allows the atoms to propagate in time. The trajectory of the atoms' positions and velocities is continuously updated throughout the simulation.

2.5 Molecular Dynamics Simulator

All the molecular dynamics simulations in this thesis are performed using the large-scale atomic/molecular massively parallel simulator (LAMMPS) [107]. LAMMPS is a free and open-source package developed by Sandia National Laboratories. The package can be used as a parallel particle simulator in the atomic, meso, or continuum scales [108]. The simulation procedure in LAMMPS can be divided into four sections: (i) Initiation (ii) Atom definition (iii) Simulation settings, and (iv) Running. Under initiation, units and boundary conditions of the simulation are defined. Various unit systems, such as SI, cgs, and metal, are available in LAMMPS. The metal unit system is used in SW potential field. In metal units, the units of distance, time, and energy are Angstroms, picoseconds, and electron-volts, respectively. Boundary conditions can be defined as either periodic or non-periodic. The input file should be named as in.filename. Coordinates of the atoms (x, y and z) and the atom types (e.g., molybdenum, sulfur) are defined under atom definition part. Atom coordinates can also be defined in a separate file, which is generally named as data.filename. This file is called when the main input file (named as in.filename) is executed.

Under the third section, potential field coefficients, simulation parameters, and output options are defined. The basic simulation parameters, such as time-step, temperature, and pressure control, are defined in this section. Many commonly used pressure and temperature controlling algorithms, such as Berendsen and Nosé-Hoover are implemented in LAMMPS. In addition, Microcanonical, Canonical, and isothermal-isobaric ensembles are also implemented in the package. During a simulation, time, and spatial averages of physical quantities, such as temperature, pressure, and energies, can be calculated. These quantities can be taken as outputs in a separate output file at specified time intervals. The final section is running the simulation. During a simulation, the simulation domain can be deformed by appropriately changing the dimensions of the domain, and the simulated nanostructure can also be attached to the simulation box. Therefore, with the simulation domain, the nanostructure also deforms, providing a method to apply strain into a nanostructure. Output of the simulation (e.g., stress, energy, temperature) is written to an output file named as log.lammps.

2.5.1 Molecular statics

Molecular statics is a branch of classical atomistic simulations that focuses on studying the relaxed configuration of atoms in a system at zero temperature [96]. In molecular statics simulations, the equilibrium structure of atoms is determined by minimizing the potential energy of the system. The goal is to find the most stable arrangement of atoms in the absence of thermal motion. There are several energy minimization methods used in molecular statics simulations, including conjugate gradient, steepest descent, and Newton-Raphson. These methods are employed to iteratively adjust the positions of atoms in order to reach the minimum energy state. The minimization process continues until a stable configuration is obtained where the forces on each atom are close to zero, indicating that the system has reached a local minimum on the potential energy surface.

In the context of the thesis, both the conjugate gradient and steepest descent methods are utilized to relax the defect containing monolayer MoS_2 sheet generated in Chapter 3. These methods are commonly used in molecular statics simulations to efficiently find the equilibrium structure of atoms with defects. The conjugate gradient method is an optimization technique that uses conjugate vectors to iteratively update the atomic positions in a way that converges to the minimum energy configuration. It is known for its rapid convergence and efficient utilization of computational resources. On the other hand, the steepest descent method is a simple and straightforward optimization approach that involves taking steps in the direction of the steepest energy decrease. Although it may take more iterations to converge compared to the conjugate gradient method, it is still a widely used method due to its simplicity and ease of implementation.

Graphically, energy minimization is the process of searching for the configuration of atoms (x) from initial configuration (x_0) that minimizes the potential energy function, $U(x)$. There are two major components of this searching process that differentiate between energy minimization methods. The first component is the direction of the search, d, and the second component is where to stop searching along that direction and look for a new direction. The first component, direction of the search, is the main difference between conjugate gradient and steepest descent methods. However, the search direction at the first step of both methods is identical. From calculus, the gradient always points toward the direction of steepest increase of that function. Therefore, the negative of the gradient points in the direction that steepest decrease of that function. For atomistic simulations, the negative of the gradient of the potential energy, $U(x)$, is the force vector, F. Thus, the position after the first searching step can be expressed as,

$$x_1 = x_0 + \alpha f_0 \tag{2.18}$$

where x_0, x_1 are the configuration at step *0 and 1*, f_0 is the force unit vector at step 0, α is the distance travel along the force vector direction, which is the second component. In both methods, α is chosen to minimize the potential energy along the force vector direction via a line search algorithm. There are three different line search methods incorporated in LAMMPS: backtrack, quadratic, and force zero, which the backtrack line search algorithm set as default. The result of choosing α that way is the orthogonality of the previous search direction with the gradient direction of the next step. For steepest descent method, the search direction is always defined as the force vector direction. As a result, shown in Figure 2.5, their successive search directions are always orthogonal, which potentially leads to slow convergence for ill-conditioned systems. To avoid the repetition in the search direction, new search directions are constructed in a way that they are conjugate with previous search direction,

$$d_{m+1} = f_m + \beta_{m+1} d_{(m)} \tag{2.19}$$

where β is the parameter to ensure the conjugate among all of the search directions. For nonlinear conjugate gradient method, there are 3 well known ways to compute β: Fletcher-Reeves, Polak-Ribiere, and Hestenes-Stiefel. The Polak-Ribiere formula has a faster rate of convergence [79] and is the method incorporated in LAMMPS:

$$\beta_{m+1}^{PR} = \frac{f_{m+1}^T (f_{m+1} + f_m)}{f_m^T f_m} \tag{2.20}$$

However, the Polak-Ribiere could cycle infinitely in some cases [78]. Typically, when $\beta_{m+1}^{PR} < 0$, the conjugate gradient method is restarted with the first direction search using the steepest descent.

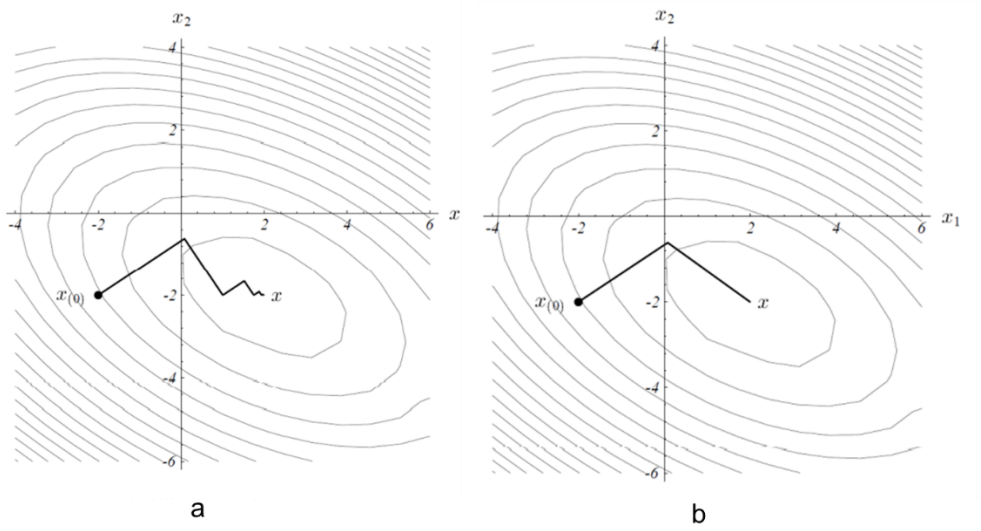

Figure 2.5 Graphical representation of (a) steepest descent method and (b) conjugate gradient method [99]

2.5.2 Uniaxial Tensile Test/ Molecular mechanics method of generating elastic tensor for MoS_2.

In this section, a uniaxial tensile test is performed on the MoS_2 sheet shown in Figure 2.6 to demonstrate the simulation procedure of LAMMPS. The size of the MoS_2 sheet is ~50Å × 50 Å with 1008 carbon atoms.

The coordinates of the Mo and S atoms in MoS_2 sheet are obtained from the crystallographic information file. The simulation temperature is 300 K, and the MoS_2 sheet is allowed to relax for 30 *ps* before applying strain. The strain rate and time-step are 0.001 ps^{-1} and 1 *fs*, respectively.

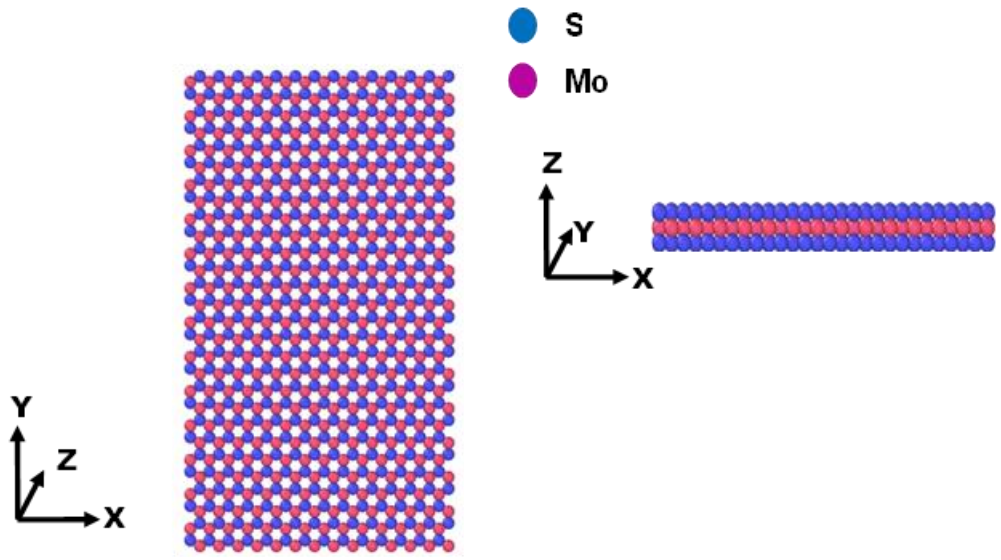

Figure 2.6 MoS_2 sheet used to demonstrate the simulation procedure in LAMMPS.

Figure 2.7 shows the MD simulation results, where Figure 2.7(a) shows the variation of potential energy per atom during the relaxation period. Potential energy significantly changes at the beginning, and the system reaches equilibrium after about 10 ps. Even after reaching the equilibrium, the potential energy fluctuates around a central value due to kinetic energy of atoms. The average potential energy during 20 ps to 30 ps could be taken as the equilibrium potential energy, which is -7.389 eV. Figure 2.7(b) shows the variation of potential energy per atom during the tensile test. Fracture occurs at a strain of 0.217, and the potential energy per atom at fracture is -2.71 eV.

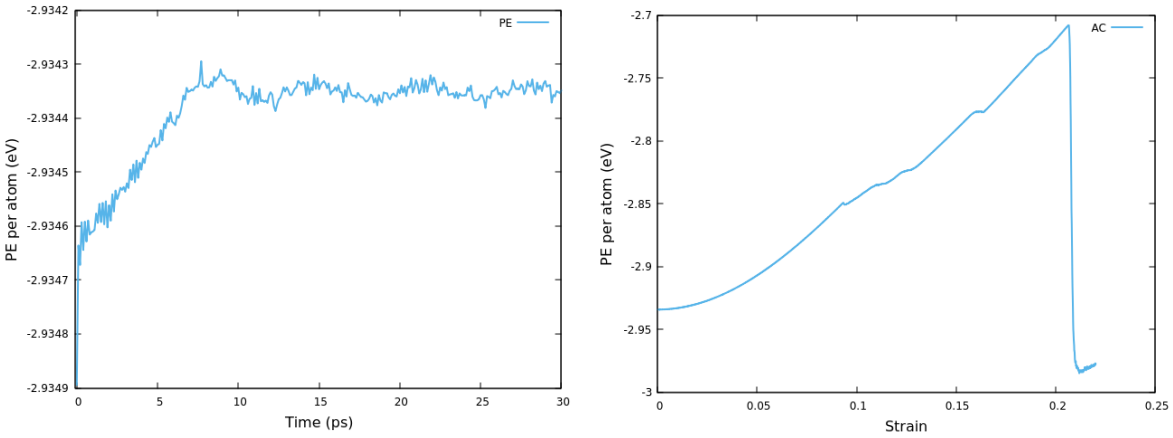

Figure 2.7 (a) Variation of potential energy (PE) per atom during relaxation period. (b) Change of PE per atom with strain.

As discussed in Chapter -1, The family of 2D materials offers a full spectrum of physical properties, from conducting graphene to semiconducting MoS_2 and to insulating h-BN. Moreover, the 2D crystal structures render a unique combination of mechanical properties, with high in-plane stiffness and strength but extremely low flexural rigidity. Together, the 2D materials are promising for a wide range of applications. Here we study related to mechanical properties of 2D monolayer MoS_2 material. We emphasize how mechanics is indispensable in the study of mechanical properties including defects and antisite defects which influence and help to design the nanostructures. During synthesis defects are bound to happen and the relationships between the MoS_2 nanosheet (pristine and with defects) are of structural features of interest, the effect of defects is crucial to study for the designing of nanomaterial. In this work, quantitative values for mechanical properties are predicted as a function of these structural features in the atomistic models. Although time dependence is not considered directly here, these molecular structural features are known to vary with defects and exposure considered. Therefore, effects of defects on these monolayer MoS_2 models are studied.

The atomistic modeling of materials for calculating mechanical properties has been researched for several decades. A static method was developed early on using molecular mechanics (MM)

techniques [13]. Stress-strain simulations in molecular dynamics (MD) have been employed for some time [14]. However, performing these simulations is not a trivial task. It can be difficult to obtain mechanical properties from atomistic simulation that compare well with experimentally measured values due to the difficulty of preparing the models and the various parameters involved [15, 16]. A comparably high rate of strain is necessary in these simulations due to the short time scales of MD simulations as compared to experimentally accessible time scales. Atomistic MD simulations typically employ the integration of time steps 1 fs (femtosecond) in duration. A feasible (computationally affordable) run might employ 10^5 to perhaps 10^6 - time steps, which would be a duration of 10^2 -10^3 ps.

At 0 K, all 2D relative components of the stiffness matrix can be determined from the static method using eqn.

$$\frac{\partial^2 U}{\partial \varepsilon_{ij} \partial \varepsilon_{kl}} = \frac{\partial \sigma_{ij}}{\partial \varepsilon_{kl}} \tag{2.21}$$

where *U* is the potential energy.

This approach requires a deformation of an energy-minimized structure in the direction of interest followed by a second energy minimization. Deformations of 1.0×10^{-6} S^{-1}, 5.0×10^{-7} S^{-1}, and 1.0×10^{-7} S^{-1}, were tested to ensure the deformation choice did not affect the final results. Elastic properties were obtained using a value of 5.0×10^{-7} S^{-1}.

2.6 Evolutionary Optimization

Optimization, at its core, involves the process of selecting the most favorable choice from a range of available options according to specific criteria. There are primarily two categories of optimization methods: local optimization methods and global optimization techniques.

- Local Optimization Methods**:** These methods typically converge to a local optimum. They heavily rely on the initial values provided to the optimization algorithm. Consequently, the results achieved are greatly influenced by the starting point chosen.
- Global Optimization Techniques: In contrast, global optimization methods, often based on heuristics, are more inclined to search for the global optimum. These techniques are particularly suitable for multimodal functions where there are multiple peaks or valleys, making it challenging for standard algorithms to pinpoint the global optimum.

Many optimization techniques are derived from biological principles, such as natural selection, learning processes, and probabilistic rules. Evolutionary algorithms, proposed by Michalewicz in

1996 [97], and particle swarm optimization (PSO) developed by Kennedy and Eberhart in 2001 [98], are examples of such techniques. These bioinspired approaches are adept at handling multimodal optimization problems in various fields, including mathematics and engineering.

However, there is no one-size-fits-all solution when it comes to selecting the best optimization technique. Each algorithm possesses its own set of strengths and weaknesses. The performance of these algorithms is heavily reliant on the nature of the optimization problems, the constraints involved, and the specific parameters of the algorithms used.

For instance, the evolutionary algorithm (EA) is inspired by the mechanisms observed in the evolution of species. It simulates the natural process of evolution—like selection, crossover, and mutation—to explore and search the solution space for optimal solutions.

Selecting the most appropriate optimization technique depends on the specific problem at hand. Understanding the characteristics of the problem, the nature of the constraints, and the behavior of different algorithms is crucial in deciding which optimization method might be the most effective for a given scenario. Tailoring the choice of method to suit the unique features of the problem often yields more successful optimization outcomes.

The implementation of the Evolutionary Algorithm (EA) used in this work is outlined in the provided flowchart shown in Figure 2.8. The algorithm initiates by creating an initial population of individuals, each representing a potential solution. These individuals are generated in a manner that aligns with the specific needs of the problem. The creation of the initial population can occur in a random or ordered manner, based on the requirements of the problem being addressed.

An individual within this EA framework consists of chromosomes, with each chromosome representing a single solution. Typically, in applications of EA, individuals are composed of one chromosome, denoted as **ch**, with arrays of genes (g_i) representing design variables. These genes often carry coded design variables, but in this particular approach, floating-point genes were utilized. As a result, additional coding to represent these design variables was not necessary, as the floating-point representation sufficed for the purpose of the algorithm.

This means that the genetic structure within this EA directly represents the parameters of the problem without the need for additional encoding or transformation of the genes. Consequently, the floating-point representation of genes enables a more direct translation and manipulation of the parameters, simplifying the implementation of the EA for this specific problem context.

In this particular implementation of the Evolutionary Algorithm, after the creation of individuals and the establishment of their genetic structure representing the solution space, the next step involves the evaluation of these individuals.

- **Molecular Dynamics (MD) Simulations and Fitness Evaluation:** For each individual within the population, MD simulations are conducted based on the atomic structure defined by their genes. Subsequently, individual fitness functions are calculated, reflecting the suitability or quality of the solution represented by each individual.
- **Selection Process:** The selection phase involves choosing individuals for the next iteration based on their fitness values. The probability of an individual's survival in the selection process is directly linked to the value of their fitness function. Higher fitness indicates a higher likelihood of survival and reproduction for the next generation.
- **Ranking Selection:** Ranking selection is performed by assigning a rank value to each individual based on their fitness score. Better fitness scores correspond to higher rank values, while lower fitness scores are assigned lower ranks. This step segregates individuals based on their fitness performance.
- **Offspring Generation:** New individuals for the offspring generation are drawn based on their rank value. Individuals with higher ranks have a higher probability of being selected to produce the next generation.
- **Termination Condition and Evolutionary Operators:** The iterative process continues until the termination condition is met, often specified by a maximum number of iterations. If the termination condition is not satisfied, evolutionary operators are used to modify the genes of the individuals. The evolutionary operators utilized in this implementation include uniform and Gaussian mutation, as well as simple and arithmetic crossovers. These operators allow for the introduction of genetic diversity by altering the genetic structure of individuals, creating new variations that might potentially improve the solution space.

This iterative process—consisting of selection, reproduction, and genetic alteration—is repeated until the termination condition is reached, thereby evolving, and refining the population of individuals with each iteration. The introduced genetic variations allow for exploration of the solution space, enhancing the likelihood of finding optimal or near-optimal solutions to the optimization problem at hand.

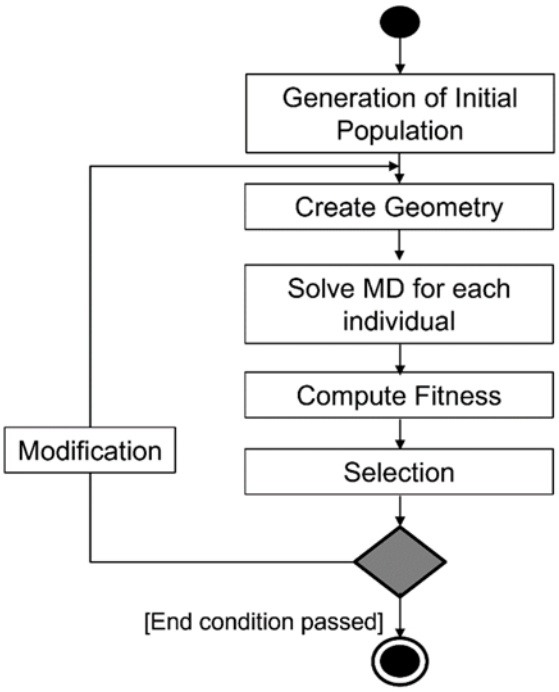

Figure 2.8 Evolutionary algorithm flowchart.

In the context of the EA discussed, the objective function, also known as the fitness function, is calculated for each chromosome or individual in the population. The fitness function is derived from the direct problem solution provided by each individual, reflecting the optimization goal of the problem at hand.

Given the substantial number of chromosomes within the population and the numerous iterations of the evolutionary algorithm, there is a considerable volume of direct problems that need to be solved during the optimization process. This extensive computation demands a significant amount of computational resources and time.

To minimize the overall optimization time or wall time, a parallel computing approach was employed. This parallel approach involves splitting the computational workload across multiple processors or computational units, running simultaneous calculations, and aggregating the results.

By utilizing parallel computing, the computation time can be significantly reduced. This strategy allows for more efficient use of computational resources, accelerating the optimization process by distributing the workload across multiple cores, processors, or even separate computational systems. As a result, it enables quicker computation of the fitness function for each individual in the EA, ultimately contributing to faster convergence and optimization of the solution space.

2.7 Evolutionary Optimization as a Paradigm for Computational Search

Inspired by the Darwinian principle of natural selection, Evolutionary Computation (EC) has emerged as a powerful optimization technique, demonstrating remarkable success in tackling complex real-world problems [99,100]. A diverse range of engineers and scientists have harnessed the potential of Evolutionary Algorithms (EAs), a promising set of stochastic search algorithms, to address some of the most challenging optimization problems. EC has firmly established itself as a prominent area of computer science and optimization, gaining significant traction in recent years. Within the past decade, solving optimization problems using EAs has evolved into a crucial application area of EC. EC's inherent parallelism, coupled with intelligent attributes such as self-organization, adaptation, and self-learning, has enabled its successful application to a wide spectrum of problems where classical approaches are either impractical or yield suboptimal results. The growing interest in EC has been particularly pronounced in recent years [101,102].

The remarkable success of EC gained widespread recognition in the 1980s, when it was employed to solve exceptionally complex optimization problems across various disciplines, cementing its undeniable breakthrough as a problem-solving methodology [103]. This breakthrough has been manifested in the burgeoning number of publications in the field, accompanied by a corresponding surge in specialized conferences and journals. Despite the existence of these dedicated venues, a substantial body of application-specific EC research remains scattered across the publications of diverse disciplines, including Operations Research (OR) / Optimization, and is often presented at their respective conferences, further highlighting the general applicability and success of EC methods.

The application of EC to optimization problems is known as Evolutionary Optimization (EO). The widespread popularity of EO across various disciplines has prompted us to bring it to the attention of the OR/optimization research community. Our experience indicates that OR/Optimization researchers and practitioners hold diverse views on the utilization of EC methods for solving optimization problems. OR/Optimization researchers and practitioners frequently employ heuristics to identify near-optimal solutions for a multitude of large and complex problems. EC methods, at their core, are heuristic. Unlike conventional optimization techniques, EC methods lack a strong mathematical foundation, and guaranteeing algorithm convergence (for all problems) within a finite number of steps poses a challenge.

2.7.1 Evolutionary Computation as a Search Paradigm

Evolutionary computation (EC) is an interdisciplinary field that draws inspiration from biological evolution to design computational algorithms. It encompasses techniques that mimic natural processes like selection, mutation, and recombination to solve complex optimization problems. EC has borrowed terminology from fields like molecular evolution, population genetics, and immunology to reflect its connections. However, its primary goal is not to create biologically accurate models but rather to develop robust and efficient computational systems for solving real-world problems. Evolutionary algorithms (EAs) are a type of stochastic search procedure that iteratively generates and tests candidate solutions until a satisfactory solution is found. They differ from conventional generate-and-test algorithms in that they maintain a population of solutions and apply operators like selection, mutation, and recombination to improve the solutions over time [104].

- **Initialization:** Generate an initial solution and set it as the current solution.
- **Perturbation:** Generate a new solution from the current solution by making a small change.
- **Evaluation:** Test whether the new solution is better than the current solution.
- **Selection:** If the new solution is better, accept it as the current solution. Otherwise, keep the current solution unchanged.

  Repeat steps 2-4 until a satisfactory solution is found.

Different algorithms use different strategies for the generation of the initial solution, the perturbation and acceptance of the current solution.

EAs have two prominent features which distinguish themselves from other search algorithms. First, they are all population-based (consider a set of possible solution points in contrast to single solution point in conventional optimization). Second, there is communications and information exchange among individuals in a population. A general framework of evolutionary algorithms can be summarized as follows.

1. Set i = 0.
2. Generate the initial population P(i) at random.
3. REPEAT
   (a) Evaluate the fitness of each individual in P(i).

(b) Select parents from P(i) based on their fitness.

(c) Apply search operators to the parents and produce generation P(i+1).

4. UNTIL the population converges, or the maximum time is reached

Evolutionary algorithms (EAs) are population-based search algorithms that mimic natural selection to solve complex problems. They use operators like crossover and mutation to generate new solutions and selection to choose the best ones. EAs offer flexibility in search operators and selection procedures, providing opportunities for researchers in Operations Research and Optimization to contribute to the field of evolutionary computation [104]. Evolutionary computation can be divided into four major branches which are briefly discussed in the following section.

2.7.2. Evolutionary Algorithm Variants

Evolutionary computation (EC) encompasses a diverse range of algorithms inspired by the principles of natural evolution, encompassing four major branches: evolution strategies, evolutionary programming, genetic algorithms, and genetic programming. These branches differ in their fundamental design principles, leading to variations in their representations of potential solutions and the operators used to modify these solutions. Representation and search are two fundamental aspects of EC that significantly influence the effectiveness of these algorithms. Different EC algorithms employ distinct representations for individuals, the entities that represent potential solutions to the problem being addressed. These representations can broadly be categorized into three main types: lists, trees, and graphs. For mathematical optimization problems, lists are the most prevalent representation scheme. Lists encompass various forms, including binary strings, real-valued vectors, integer vectors, and symbolic strings. The choice of representation significantly impacts the problem-solving capabilities of EC algorithms [97].

Search operators play a pivotal role in the reproduction of offspring, the process of generating new solutions from existing ones. These operators mimic the mechanisms of natural selection, driving the search towards improved solutions. Common search operators include crossover, mutation, and selection. Crossover combines two parent solutions to create a new offspring solution, inheriting characteristics from both parents. Mutation introduces random modifications to a solution, potentially leading to novel and beneficial changes. Selection determines which solutions are more likely to be selected for reproduction, ensuring that the search focuses on promising areas of the solution space. The judicious selection of representation, search operators, and selection scheme is crucial for the success of EC algorithms. The interplay between these elements determines the effectiveness of the algorithm in navigating the search space and ultimately converging to optimal solutions. The

appropriate choice of these components depends on the specific problem being addressed, its characteristics, and the desired outcomes.

There are four main branches of EAs: evolution strategies (ES), evolutionary programming (EP), genetic algorithms (GAs), and genetic programming (GP). Each branch has its own unique characteristics, but they all share a common framework based on the principles of natural evolution.

Evolution Strategies (ES): ES was first introduced by Rechenberg and Schwefel in 1965 as a numerical optimization technique. They are similar to EP in that they use real-valued vectors to represent individuals and Gaussian mutation. However, they differ in their selection and recombination operators. ES uses deterministic selection and discrete or intermediate recombination, while EP uses probabilistic competition and forgoes recombination [105,106].

Evolutionary Programming (EP): EP was developed by Fogel and others in the mid-1960s as a means to achieve artificial intelligence [107]. It has been applied to combinatorial and numerical optimization problems. EP is similar to ES in its algorithmic structure, using real numbers as individuals, Gaussian mutation, and self-adaptation. However, EP differs in its selection and recombination. EP employs probabilistic competition (tournament selection) as its selection mechanism and forgoes recombination [108].

Genetic Algorithms (Gas): GAs were pioneered by Holland and his student Jong in 1975 [109,110], although some ideas emerged earlier in the context of genetic system simulation. They were initially proposed as adaptive search algorithms but are now primarily used for global optimization in combinatorial and numerical problems. GAs are the most widely known branch of EAs. They differ significantly from ES and EP in individual representation and search operators. GAs emphasizes genetic encoding of potential solutions into chromosomes and apply genetic operators to these chromosomes. This effectively transforms the original problem from one space to another. Genetic representation is crucial for the success of GAs. While a simple GA employs binary representation, one-point crossover, bit-flipping mutation, and roulette-wheel selection, numerous variations exist. Recombination (crossover) plays a major role in GAs, while mutation serves as a background operator [97].

Genetic Programming (GP): GP is considered a specialized sub-branch of GAs. It was developed by Koza in 1992 as an application of GAs to evolve tree-structured chromosomes [111]. Historically, these trees represented LISP programs. GP utilizes both crossover and mutation. Due to its infrequent application in mathematical optimization, GP is not a primary focus of this discussion.

The term "evolutionary algorithms" has gained traction among researchers to encompass ES, EP, and GAs, given their shared computational framework. This perspective is adopted in this work.

2.7.3 Harnessing Nature's Design Principles: Why Evolutionary Algorithms Excel at Optimization

EC is a powerful tool for optimization, especially for problems that conventional methods struggle with. It offers robustness, versatility, parallelism, and adaptability, but lacks a rigorous theoretical foundation and can be computationally expensive. The choice between EC and conventional techniques depends on the specific problem requirements.

Properties of Functions: In EC, the properties of functions, such as convexity, concavity, and continuity, are not crucial considerations. Unlike conventional mathematical programming techniques, EC does not rely on these properties for optimization. Instead, EC randomly generates an initial population of solutions and iteratively produces new generations of solutions using simple rules [112]. This approach is applicable regardless of whether the function is differentiable or not.

While EC and conventional search procedures share the concept of generate-and-test algorithms, their specific search techniques differ significantly. EC's search mechanism is not directly comparable to conventional methods like the cyclic coordinate method, the method of Hooke and Jeeves, and Rosenbrock's method. However, EC allows for the incorporation of conventional search procedures to enhance its efficiency. This approach is known as hybrid EC.

Single best solution: Unlike conventional mathematical programming techniques that provide a single best solution, EC offers the flexibility to explore multiple solutions, including the second best, third best, and so on. This is particularly beneficial in scenarios where decision-makers need to evaluate a range of potential solutions rather than just the absolute optimum [113]. For instance, in bidding problems, decision-makers may be interested in considering the second best and third best bids alongside the optimal bid. EC's ability to provide multiple solutions allows for a more comprehensive evaluation and decision-making process.

Infeasibility: In contrast to mathematical programming techniques, which struggle with infeasible optimization problems, EC offers a more flexible approach. EC can identify infeasible constraints and suggest minimal changes to the problem structure, effectively making it feasible. While penalty function approaches are commonly used in EC for constrained optimization problems, alternative

methods such as repairing or rejecting infeasible solutions are also available [114]. EC's ability to handle infeasibility makes it a valuable tool for a wider range of optimization scenarios [115,116].

Domain Knowledge: EAs are relatively easy to implement due to their lack of reliance on extensive domain knowledge. However, incorporating domain knowledge into EAs can further enhance their performance [104]. This can be achieved by replacing the search component in EAs with conventional search techniques, refining the final EA solutions using local search techniques, or redesigning the initial population generation and selection procedures based on conventional optimization concepts.

Robustness of EC Algorithms: A common framework for evolutionary algorithms can be applied to a wide range of single-objective constrained mathematical programming models. A single penalty function-based evolutionary algorithm can be used to solve various types of linear, integer, and nonlinear programming models [114,117]. However, the optimal algorithmic parameters for the evolutionary algorithm may vary depending on the specific model being solved. In contrast, conventional optimization theory requires learning numerous specialized techniques to solve different classes of optimization problems. For instance, linear programming problems require methods like the simplex method or the interior point method [118,119], while integer programming problems often involve the branch-and-bound method or the cutting plane method [120]. Nonlinear programming problems also have their own set of solution techniques, with different methods applicable to different classes of nonlinear problems [121].

In essence, evolutionary algorithms offer a more versatile and adaptable approach to solving a broad range of optimization problems compared to conventional optimization theory, which often requires specialized techniques for specific problem types.

Constrained Handling and Penalty Methods: Conventional optimization using the penalty function method involves repeatedly solving a modified version of the original problem, with the penalty parameters constantly changing [112]. This process can be computationally expensive. In contrast, EC utilizes the penalty function method more efficiently by solving the modified problem only once and adapting the penalty parameters throughout the generations. This approach significantly reduces computational overhead [114].

Table 2.4 Differences between conventional optimization and EC in using the penalty function method:

Feature	Conventional Optimization	Evolutionary Computation (EC)
Computational efficiency	Less efficient	More efficient
Number of times modified problem is solved	Repeatedly	Only once
Penalty parameter adjustment	Requires repeated problem-solving	Adaptive adjustment during generations

Exploration and Exploitation: EAs are a versatile class of search algorithms that effectively balance exploration and exploitation of the search space [see p-15 of [114]]. This balance enables them to efficiently navigate complex landscapes and avoid getting trapped in local optima, making them particularly well-suited for solving multimodal optimization problems.

Computational Time: EAs are particularly advantageous for their ability to provide quick approximate solutions to optimization problems. They typically exhibit rapid improvement in the initial generations [122], leading to near-optimal solutions within a reasonable timeframe, even for challenging problems [123]. This makes EAs a valuable tool for tackling complex optimization tasks.

Multiobjective Optimization: EAs are particularly well-suited for multiobjective optimization due to their ability to simultaneously optimize conflicting objective functions and generate a diverse set of non-dominated solutions in a single run [124–126]. While conventional optimization techniques can be used to solve certain multiobjective problems by creating a composite objective function using weighted linear combinations of individual objective functions, this approach is limited to problems with continuous and monotonically increasing or decreasing Pareto frontiers. EAs, on the other hand, are more versatile and can handle a wider range of multiobjective problems, including those with non-continuous, non-uniform Pareto frontiers, complex, periodic, or multimodal functions [127].

Table 2.5 Differences between EAs and conventional optimization for multiobjective optimization:

Feature	Evolutionary Algorithms (EAs)	Conventional Optimization
Pareto frontier exploration	Capable of handling diverse Pareto frontiers	Limited to continuous and monotonically increasing/decreasing Pareto frontiers

Function complexity	Can handle complex, periodic, and multimodal functions	Limited to well-behaved functions
Solution diversity	Generates a diverse set of non-dominated solutions	Can be limited in generating diverse solutions

Starting Solution: Unlike conventional optimization techniques, which often require specific methods to generate initial solutions, EC algorithms generally rely on random population generation. This eliminates the need for specialized methodologies and simplifies the initialization process.

Harder Problems: Conventional optimization algorithms find integer programming and nonlinear programming to be more complex than linear programming, but EC algorithms can handle these problems with relative ease. Additionally, multi-modal problems are less likely to trap EC algorithms in local optima [128].

Optimization under Changing and Dynamic Environments: EC techniques are well-suited for handling optimization problems in changing environments, where the optimal solutions evolve over time. These problems, such as on-line data mining, job scheduling, investment portfolio evaluation, and robot path determination [129], cannot be effectively solved using conventional optimization methods. EC's ability to continuously adapt and learn from changing conditions makes it a valuable tool for optimization in dynamic environments [130].

2.7.4 Evoking Evolutionary Wisdom: Identifying the Ideal Conditions for Evolutionary Algorithm Application

While evolutionary computation (EC) methods may not be the most efficient approach for linear programming problems due to the existence of powerful conventional algorithms, they offer significant advantages in tackling complex real-world optimization problems. EC's ability to handle nonlinearity, multimodality, and dynamic environments makes it a valuable tool for solving problems that challenge conventional methods.

Knowledge of Optimization: Evolutionary computation (EC) offers a valuable approach to optimization problems even for users with limited or no mathematical knowledge. Unlike conventional optimization methods, EC doesn't require extensive mathematical expertise, making it more accessible to a wider range of users.

Ranked Solutions: Evolutionary computation (EC) is a powerful tool for generating ranked solutions, providing decision-makers with a range of optimal choices rather than just a single best solution. This

makes EC particularly valuable in scenarios where multiple perspectives or preferences need to be considered.

Multi-modal Problems: For multi-modal problems with multiple peaks, evolutionary computation (EC) methods have a lower chance of getting stuck in local optima compared to conventional optimization techniques. EC's ability to explore the search space effectively prevents it from getting trapped in suboptimal solutions.

Quick Approximate Solutions: Evolutionary computation (EC) shines in providing quick approximate solutions for large-scale, challenging optimization problems. In many scenarios, EC's ability to efficiently navigate the search space and converge towards satisfactory solutions proves advantageous over conventional optimization methods.

Multi-objective Optimization: EC holds promise for multi-objective optimization, where the goal is to find solutions that simultaneously optimize multiple conflicting objectives. EC's ability to handle trade-offs between objectives makes it well-suited for these complex optimization problems.

Optimization under Changing Environments: EC is a promising approach for optimization under changing environments, where the optimal solutions evolve over time. EC's inherent adaptability and ability to learn from changing conditions make it a valuable tool for dynamic optimization problems.

Hybrid Algorithms: EC can be effectively integrated with conventional optimization techniques and other modern methods to create hybrid algorithms capable of solving complex problems. By combining the strengths of different approaches, hybrid algorithms can achieve improved efficiency and performance in tackling challenging optimization tasks.

Computationally Cheaper: EC methods become an attractive choice when they demonstrate computational efficiency in solving any class of problems. The ability to balance exploration and exploitation of the search space, coupled with the potential for parallel processing, often leads to faster convergence and reduced computational costs compared to conventional optimization techniques. This advantage is particularly evident in handling large-scale, complex problems that involve multiple objective functions or dynamic environments.

Computational time: computational time is not a critical factor, EC methods can be employed to deliver near-optimal solutions. EC's ability to thoroughly explore the search space and converge towards optimal solutions makes it a valuable tool for problems that demand high-quality results without stringent time constraints.

Highly complex problem: Problems involving many complex features like multi-objectivity, multi-modality, changing environment, etc. would be suitable for EC techniques.

2.7.5. The Limitations of Evolutionary Computation

There are several drawbacks to using EC based methodology for solving optimization problems. They are briefly discussed below.

Table 2.6: Evolutionary Computation methodologies

Heuristics	EC-based optimization techniques are classified as heuristic search algorithms, which means they employ problem-specific rules of thumb to guide their search for optimal solutions. While these techniques often perform well in practice, they cannot guarantee that they will always find the absolute best solution. This is because they may get stuck in local optima, which are points in the search space that represent better solutions than their immediate neighbors but are not necessarily the globally optimal solution [114,117].
Parameters of EC	The performance of EC algorithms is heavily influenced by the choice of parameters, such as population size, selection pressure, mutation rate, and crossover rate. These parameters need to be carefully tuned for each specific optimization problem to achieve optimal results. Selecting inappropriate parameters can lead to poor convergence or premature convergence to suboptimal solutions [131].
Convergence of EAs	The convergence behavior of EC algorithms, meaning their ability to consistently find good solutions within a reasonable amount of time, is highly dependent on the problem being solved and the specific EC method being used. While theoretical bounds have been established for the convergence rate of certain EC algorithms, such as genetic algorithms, these bounds are often problem-specific and may not hold for all optimization problems ([132].
Mathematical Insight	EC algorithms primarily focus on searching for optimal solutions without providing much insight into the underlying mathematical structure of the optimization problem. This can be a limitation for decision-makers who may want to understand the problem's structure to make more informed decisions.
Sensitivity Analysis	Sensitivity analysis, which assesses how changes in the problem's parameters affect the optimal solution, is generally less efficient for EC models compared to linear programming (LP) models. This is because EC models are often more complex and less well-understood than LP models, making it more difficult to derive analytical expressions for sensitivity analysis.

Chapter 3

Simulation and Characterization of monolayer molybdenum disulfide with Random Defects

In this chapter, the focus is to simulate a suspended free standing nanosheet of monolayer MoS_2 with randomly distributed defects. There are 3 objectives of this chapter. First, by comparing the elastic properties of pristine MoS_2 from our simulations with experimental results, the accuracy of the SW style interatomic potential is assessed and validated. Second, the introduction of large and diverse number of defects into the crystal structure of MoS_2 material is a natural consequence of chemical growth. Therefore, understanding the nature of disorders and their role in the physical properties of MoS_2 is essential in its future developments. In this chapter we examine the roles of several parameters such as the shape of the membrane, the size influence of nanosheet by systematically varying the defects on the mechanical performance of monolayer MoS_2 are discussed in Section 3.2. Third and last, anti-site defects effects of monolayer MoS_2 are captured and described in Section 3.3 as two major sources of disorder in the atomic structure of MoS_2.

3.1 Introduction: Significance of Mechanical Properties in Materials

In the realm of materials science, mechanical properties reign supreme as a cornerstone for evaluating material performance. While the modern era has witnessed a surge in the discovery of innovative materials with diverse functionalities, mechanical properties remain indispensable, particularly in the pursuit of robust and rigid materials for applications ranging from everyday life to the vast expanse of space [133,134]. Mechanical attributes continue to hold sway in various domains, including semiconductors, where they complement the electrical and optical traits of materials [135,136]. Furthermore, in the burgeoning field of flexible, stretchable, and epidermal electronics, mechanical properties play a pivotal role in design and functionality, paving the way for the future of the electronics industry [137,138].

Over the past three decades, nanoscience and nanotechnology have captivated the scientific community, with two-dimensional (2D) materials emerging as a focal point [2,139–142]. In the realm of 2D materials, electrons and phonons are confined to a planar dimension, leading to properties that diverge from their three-dimensional counterparts [143]. Iconic examples include graphene, known for its massless Dirac fermions, and molybdenum disulfide (MoS_2), exhibiting an intrinsic direct band gap [54,144]. These distinctive features give rise to a fascinating array of electrical and optical characteristics [20,33,145,146]. An intriguing question arises: Does the mechanical behavior of 2D

materials also alter as they approach the monolayer limit? In the realm of three dimensions, properties like the elastic modulus (E) and Poisson's ratio (ν) serve as markers for determining a material's elastic properties. In the context of 2D materials, these parameters necessitate a renormalization by the planar elastic energy, resulting in units of J/m² or N/m. While the utilization of 2D modulus and strength is more fitting for describing 2D materials, a comparative analysis between 2D and 3D materials requires the conversion of these 2D parameters to their 3D counterparts by dividing the 2D values by the thickness of the 2D materials. Conventional elastic theory can be seamlessly applied to 2D systems, but numerous novel aspects of mechanical properties in 2D systems diverge from those in 3D systems. The initial step toward probing the mechanical properties of 2D systems involves precisely measuring the mechanical attributes of 2D materials.

3.2 Elasticity measurements by experimental methods and simulation

Measuring the mechanical properties of two-dimensional (2D) systems is challenging due to the difficulty in achieving uniform stretching of a 2D membrane as compare to one-dimensional (1D) systems like carbon nanotubes, because stretching the 1D structures directly provides insights into their mechanical properties [133,147]. In 2008, researchers at Columbia University, led by Lee et al., made a significant breakthrough by using atomic force microscopy (AFM) nanoindentation to investigate suspended circular graphene membranes [148]. In this method, the AFM tip is used to apply pressure on the center of the membrane (Figure 3.1). When the radius of the tip is much smaller than the radius of the hole ($r_{tip} << r_{hole}$), the force applied by the AFM tip can be approximated as a point load. A simplified continuum mechanics model relates the applied load to the deformation geometry of the membrane [148,149].

$$F = (\sigma_0^{2D}\pi)\delta + \left(E_0^{2D}\frac{q^3}{r^2}\right) \tag{3.1}$$

where F is the applied point load force, d is the indentation depth at the center of the membrane, r is the hole radius, $q = 1/(1.05-0.15v-0.16v^2)$ is a dimensionless constant determined by the Poisson's ratio, v, of the membrane, E^{2D} *and* σ_0^{2D} *are the 2D* modulus and the 2D pretension, respectively (Fig. 3.1).

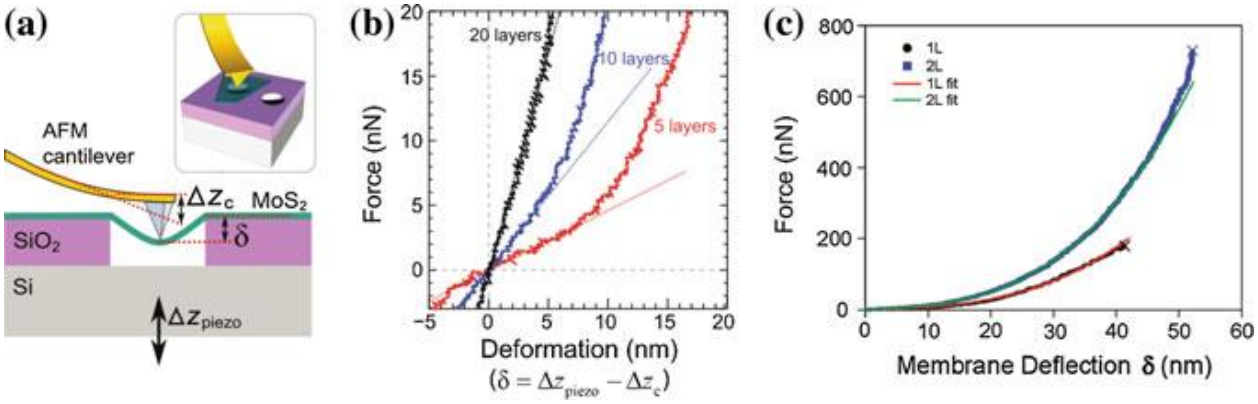

Figure 3.1 Illustration of probing mechanical properties of 2D materials by AFM nanoindentation. [156]. ***b*** *Force versus deformation traces measured at the center of the suspended part of MoS 2 nanosheets with 5, 10, and 20 layers in thickness.* ***c*** *Loading curves for single and bilayer* MoS_2*.; c Loading curves for single and bilayer* MoS_2 [18].

The Eqn 3.1 relates the applied load to the indentation depth, describes the mechanical behavior of ultrathin monolayer membranes. These membranes are indeed exceptionally thin, which makes contributions from bending or flexural rigidity negligible in many cases. In the early stages of indentation, the relationship between the applied load (F) and the indentation depth (δ) is approximately linear ($F \sim \delta$). The coefficient in this linear relationship is primarily influenced by the pre-tension in the membrane. As the indentation depth increases, the load becomes dominated by the stiffness of the membrane, leading to a cubic relationship ($F \sim \delta^3$). Graphene and TMDs exhibit nearly isotropic mechanical properties in the plane, due to their lattice structures with 6-fold or 3-fold symmetry.

Two studies have comprehensively investigated the elastic properties, stretching behavior, and fracture characteristics of ultrathin freely suspended MoS_2 [50,150]. In both studies, an atomic force microscopy (AFM) tip was used to apply force to a MoS_2 membrane suspended over a small hole in a SiO_2 substrate. The deflection of the membrane was measured, and the data was used to extract key mechanical parameters, such as the pre-tension (σ_0^{2D}) and the elastic modulus (E_{2D}). For samples with a thickness of 5–20 layers as shown in Figure 3.1 b, the pre-tension was determined to be 0.05 ± 0.02 N/m and Young's modulus (E Young) to be 350± 20 Gpa [150]. For monolayer thin membranes, the average elastic modulus (E_{2D}) was found to be 180 ± 60 N/m[1], with a pre-stress (σ_0^{2D}) ranging from 0.02 to 0.1 N/m. This yielded Young's modulus (E) of 270 ± 100 GPa, which is close to the Young's modulus of MoS_2 nanotubes (230 GPa) and is about four times smaller than that of graphene (1 TPa).

[1] 1 N/m = 1.55 Gpa

Young's modulus of bilayer MoS_2 was determined to be 200 ± 60 GPa, slightly lower than that of a monolayer due to "defects or interlayer sliding".

Chemical vapor deposition (CVD) methods have been developed to synthesized large-area and wafer-scale of MoS_2 [151,152]. These CVD-grown samples typically exhibit a distinct pattern of isolated triangular monolayer crystals at positions farther away from the precursors and a continuous film closer to the precursors (Figure 3.2 [a-c]). To investigate the mechanical properties of CVD-grown monolayer TMDs, atomic force microscopy (AFM) nanoindentation have been employed, a similar approach used for CVD graphene [153]. For CVD-grown monolayer MoS_2 and WS_2, have transferred onto holey substrates to eliminate complications arising from ripples during mechanical property measurements Figure 3.2 [d-e]. Using AFM nanoindentation, they determined the Young's modulus of monolayer CVD MoS_2 and WS2 as 171 ± 11 N/m (corresponding to 264 GPa) and 177 ± 12 N/m (272 GPa), respectively Figure 3.2 [f-g].

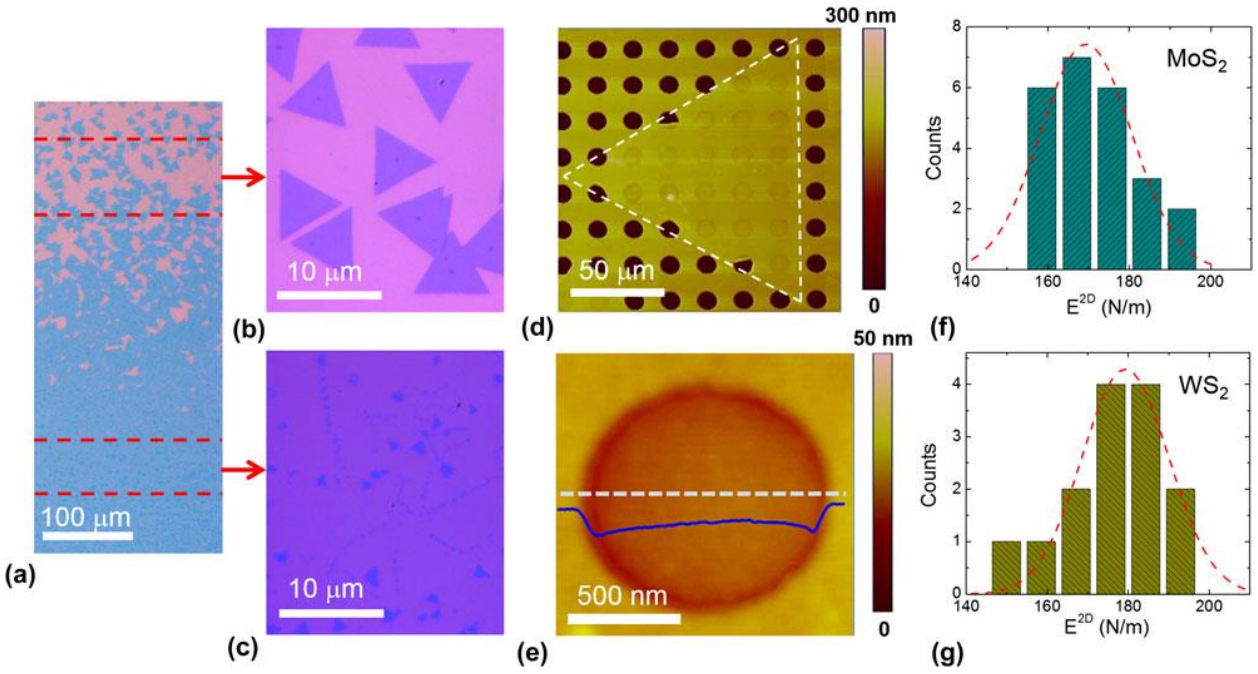

Figure 3.2 Measurements of CVD MoS_2: AFM image of an entire triangle transferred onto a holey substrate, histograms of E 2D for MoS_2 and the corresponding Gaussian distribution, [Ref from [156].

Theoretical calculations predict a 2D modulus of 123 N/m for MoS_2, falling short of experimental measurements. This discrepancy aligns with the tendency of DFT-GGA calculations to underestimate the bulk modulus of semiconductor materials. Experimental studies have revealed a modulus of ~170 N/m for CVD MoS_2, only marginally lower than that of exfoliated MoS_2 (~180 N/m) [50]. This observation suggests that point defects in CVD samples do not exert a significant influence on their

mechanical properties. All of the elastic moduli and break strengths for 2D materials ever measured are listed in Table 3.1.

Table 3.1. Elastic properties of 2D materials ever measured.

Materials	Young's modulus (Gpa)	Tensile strength (Gpa)
Exfoliated graphene (monolayer) [148]	1000	130
Bulk MoS_2 [154]	240	-
Exfoliated MoS_2 (monolayer) [50]	270	23
Exfoliated MoS_2 (ML) [155]	330	-
CVD MoS_2 (monolayer) [156]	264	-

Cooper et al. [157] introduced a multiscale constitutive model to accurately capture the nonlinear elastic behavior of monolayer MoS_2. This model, derived from a Taylor series expansion of the elastic strain energy density potential, incorporates 14 independent parameters determined through fitting to density functional calculations. The model's validity was confirmed by comparing simulated results to experimental data obtained from atomic force microscopy (AFM) indentation tests. The model accurately predicted the ultimate stress (16.5 N/m) and in-plane elastic modulus (130 N/m) of monolayer MoS_2, aligning with experimental findings reported by Bertolazzi et al. [50]. Cooper et al.'s model serves as a bridge between experimental observations and computational simulations, providing a valuable tool for large-scale simulations of monolayer MoS_2 under various conditions. Li et al. [158] conducted a study to map the in-plane Young's modulus of mono- and bi-layer MoS_2 on a substrate with high spatial resolution. They used a technique called bi-modal atomic force microscopy to accurately map the effective spring constant between the microscope tip and the sample. Additionally, they developed a finite element method to quantitatively account for the effect of substrate stiffness on deformation. As a result of their investigation, the in-plane Young's modulus of monolayer MoS_2 was determined to be approximately 265 ± 13 GPa. The in-plane Young's modulus of bi-layer MoS_2 could not be differentiated from that of monolayer MoS_2. The results of the study are consistent with previous reports and provide a more precise characterization of the Young's modulus of MoS_2. Peng and De [159] investigated the mechanical properties of g-MoS_2 (single-layer referred to as g-MoS_2) using density functional theory (DFT) simulations for elastic energy storage applications. They found that g-MoS_2 is mechanically stable and can withstand large strains (0.24 for armchair, 0.37 for zigzag, and 0.26 for biaxial deformation) before structural failure. The in-plane stiffness of g-MoS_2 is exceptionally high (120 N/m or 184 GPa), indicating excellent

mechanical strength. Higher-order elastic constants are crucial for accurately describing the material's response to large deformations. Kandemir et al. [93] investigated the lattice thermal conductivity of MoS_2 and MoSe2 using molecular-level theories. They developed an interatomic potential parameter set that accurately reproduces the lattice thermal transport properties of these materials when compared to first-principles calculations. The lattice length of MoS_2 was determined to be 3.2 Angstroms, and the distance between two chalcogen atoms, one above and one below the Mo layer (dX_u, X_d), was found to be 1.63 Angstroms. Additionally, the elastic constants, Young's modulus, and Poisson's ratio were calculated. For example, C_{11} was determined to be 133 N/m, C_{12} was 39.4 N/m, Young's modulus (E) was 121.4 N/m, and Poisson's ratio (ν) was 0.3. The study highlights the importance of accurately modeling these materials at the molecular level to predict their thermal transport properties.

3.3 Atomic defects in monolayer molybdenum disulfide (MoS_2)

Defects indeed play a crucial role in shaping the properties of two-dimensional materials like monolayer MoS_2. Structural defects in monolayer MoS_2 can take various forms, including point defects, line defects, and grain boundaries. These defects can significantly impact the material's properties. Point defects in monolayer MoS_2 can be generated during the growth process or by other means, such as electron irradiation in high-resolution transmission electron microscopy (HR-TEM) [160,161]. These defects can include vacancies, substitutions, or adatoms that replace or disrupt the regular arrangement of atoms in the lattice. The presence of defects can have a significant impact on the mechanical properties of monolayer MoS_2. For instance, defects can reduce the material's failure strain and intrinsic strength [162]. Both experimental and computational methods have been employed to characterize and visualize structural defects in monolayer MoS_2. Experimental techniques like HR-TEM can reveal the presence and distribution of defects, while computational simulations help understand their effects on material properties at the atomic scale. Hong et al. [163] investigated point defects in monolayer MoS_2 using a combination of experimental and theoretical methods. They used aberration-corrected scanning transmission electron microscopy (STEM) to systematically identify and quantify point defects in monolayer MoS_2 samples prepared by various methods, including mechanical exfoliation, physical vapor deposition (PVD), and chemical vapor deposition (CVD). They found that the defect density could be as high as 3.5×10^{13} cm^{-2} and that the dominant type of defect depended on the growth method. Interestingly, the dominant category of defects varied depending on the growth method. In mechanical exfoliation and CVD samples, sulfur vacancies were the predominant defects, while in PVD samples, molybdenum antisite defects were more common as shown in Figure 3.3. Ab-initio calculations and electric transport measurements revealed that point defects can introduce localized electronic states within the band gap, affecting

electronic properties and charge transport. The work highlights the importance of defect engineering in the growth of high-quality monolayer MoS_2 for high-performance electronic devices.

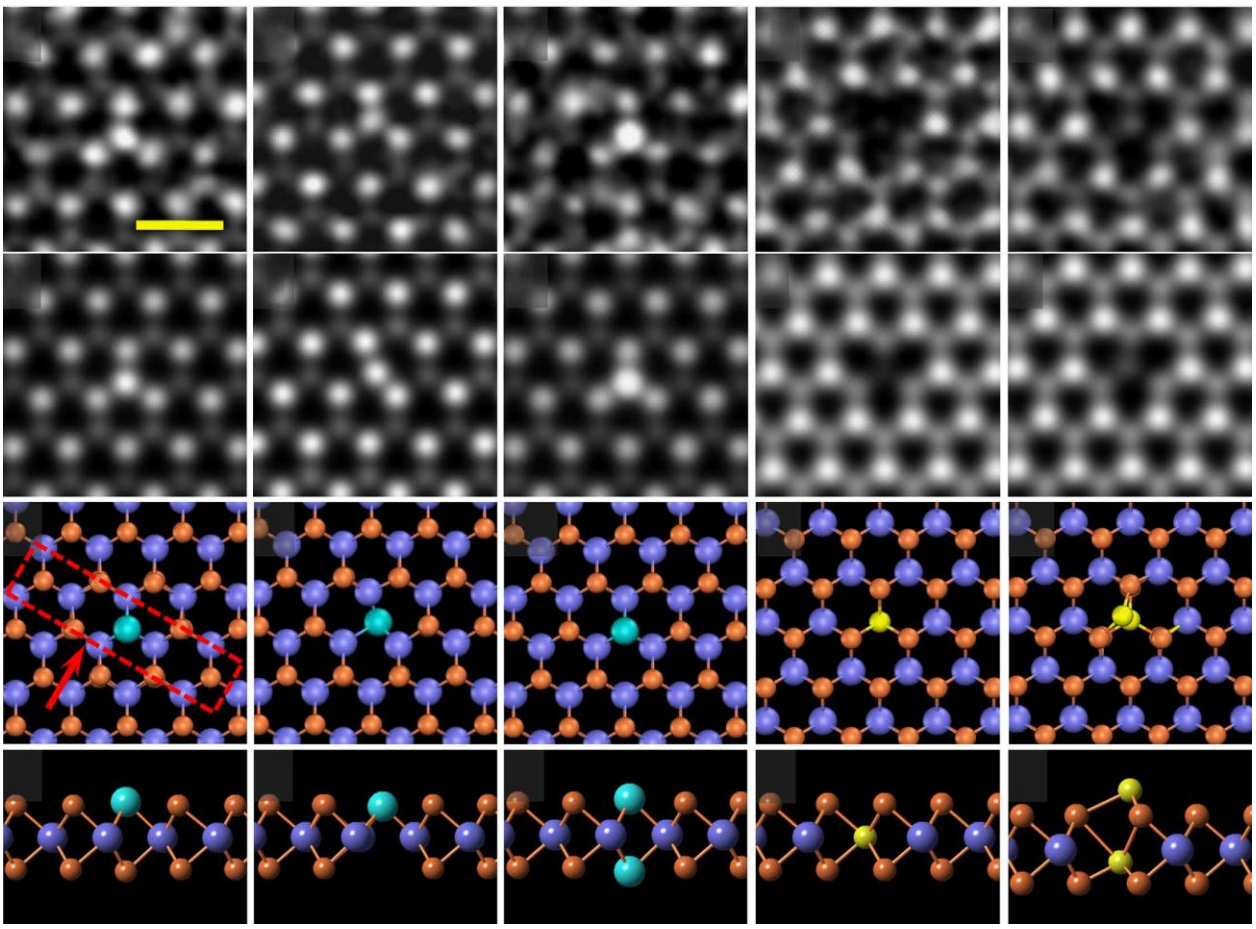

Figure 3.3 | Atomic structures of antisite defects. (a–c) High-resolution STEM–ADF images of antisite Mo S, Mo S2 and Mo2 S2, respectively. The former two antisites (highlighted by the red dashed rectangle in k) are dominant in PVD-synthesized MoS_2 single layers. Scale bar, 0.5 nm (d, e) Atomic structures of antisite defects S Mo and S2 Mo, respectively. (f–j) Simulated STEM images based on the theoretically relaxed structures of the corresponding point defects in (a–e), using simulation software QSTEM 49. (k–t) Relaxed atomic model of all antisite defects in a–e through DFT calculation, with top and side views, respectively. Light blue, Mo atoms; gold, S atoms. For ease of comparison, we have presented the simulated ADF images before the atomistic schematics of the DFT calculated structures [163].

Avik et al. [164] provides insights into the mechanical properties of single-layer MoS_2 with vacancy-induced defects. The study shows that the Young's modulus is significantly affected by different defect types and their density. However, temperature has a less pronounced impact. Interestingly, $SLMoS_2$ exhibits anisotropic mechanical behavior, with the zigzag direction being more sensitive to defects than the armchair direction. The study also indicates that vacancies have a greater influence on mechanical properties than phase transitions. W. Wang et al. [165] investigated the structural and electronic properties of monolayer MoS_2 with sulfur vacancies using density functional theory (DFT). They found that sulfur vacancies cause inward relaxation of the MoS_2 structure and reduce the

material's Young's modulus and ultimate strength. The weakening effect of vacancies on mechanical properties varies with different uniaxial tensile loading directions. Under tensile strain, the band gap of monolayer MoS_2 decreases regardless of the vacancy type or loading direction.

Nasiri [166] investigated the mechanical failure of graphene sheets with randomly distributed vacancies using atomistic simulations. They found that the failure stress of graphene sheets decreases with increasing defect concentration and sheet size, consistent with the Duxbury-Leath-Beale (DLB) theory of mechanical breakdown in random media. This theory deals with how disorder and connectivity affect transport properties and failure behavior in disordered materials. The study highlights the importance of statistical analysis and the complex energy landscape governing microstructure evolution in strongly defective graphene. Yan Chen's focuses on introducing lattice defects in monolayer MoS_2 through thermal annealing in a vacuum and Ar+ ion irradiation. These methods create different types and densities of lattice defects, allowing for the investigation of how defective nature affects the material's electronic structure. The findings indicate that lattice defects significantly impact the electronic structure of monolayer MoS_2, highlighting their importance in understanding and tailoring the material's electrical and optical properties.

In general, atomistic simulation software is employed to identify the structural strength of a material when subjected to external forces. This process typically begins by finding the configuration with the lowest energy, a procedure often initiated through conjugate gradient minimization. This technique provides valuable insights into the crystal lattice structure of materials under various phases and conditions. Molecular static simulations are specifically designed to investigate the mechanical properties of materials, with a particular focus on determining the independent elastic constants of monolayer Molybdenum disulfide ($MLMoS_2$). These simulations aim to understand how the material responds to mechanical stress, especially when it contains point defects, such as vacancies in the Sulfur (S) atoms. This study deliberately introduces random defects into the monolayer MoS_2. Simulating these intricate random defects accurately requires running numerous simulations using molecular statics. This approach effectively captures the elastic properties of the material. The methodology involves conducting multiple defect simulations, each with varying defect fractions ranging from 0% to 25%. For each defect fraction, the simulations provide valuable information about the material's elastic properties and how these properties relate to the topological characteristics of the monolayer nanosheet. Li et al. and Wang et al. [165,167] have previously explored low concentration defects in the topology, whereas our study encompasses defects spanning a range from low to high concentrations to replicate the monolayer structure of MoS_2. To achieve this, our approach involves introducing multiple defects with varying concentrations into the topology. We use conventional molecular static modeling to generate topology-based atomistic defects, employing a random equilibrium distribution of the domain in our research. In contrast, Hong et al. [163] have

highlighted the prevalence of antisite defects, where molybdenum replaces sulfur, in MoS_2 grown using physical vapor deposition (PVD), while sulfur vacancies are more common in MoS_2 obtained through mechanical exfoliation and chemical vapor deposition (CVD) methods. MoS_2 is a material of significant interest due to its unique electrical, thermal, and optical properties. Another study [168] has examined the influence of vacancies on the electrical properties of MoS_2. Our research, on the other hand, concentrates on investigating the mechanical properties of monolayer MoS_2 containing randomly distributed defects by systematically varying the concentration of vacancies. We present new results obtained for different defect levels and various random defect distributions. These findings have the potential to be valuable for future research involving the optimization of mechanical nanomachines and nanosystems based on MoS_2 sheets. The simulation methodology in detail is discussed and provides information on the theoretical framework used for analyzing defected sheets in chapter 2. The results and discussion are presented in Section 3.6 and summary is provided in Section 3.7

3.4 Elastic stability conditions in crystalline systems:

The fundamental principles governing the mechanical stability of stress-free crystalline structures were established through the groundbreaking work of Max Born and his colleagues in the 1940s [169]. Born's seminal contributions in this field were meticulously compiled and further elaborated upon in his influential book published in collaboration with Kun Huang in 1954 [170]. Building upon these foundations, subsequent textbooks, such as those authored by J. F. Nye and D. C. Wallace [171,172], have endeavored to simplify and clarify the stability criteria for specific crystal classes, bringing them within reach of a broader audience. In particular, for cubic crystals, the stability conditions assume a remarkably straightforward form:

$$C_{11} - C_{12} > 0; C_{11} + 2C_{12} > 0; C_{44} > 0 \qquad (3.2)$$

The cubic crystal system adheres to the well-known "Born stability criteria". This section outlines the general elastic stability conditions for crystals and presents necessary and sufficient conditions for cubic and hexagonal crystal classes. It also identifies crystal classes lacking analytical necessary and sufficient conditions.

3.4.1 General Stability Condition: Cubic crystal system

The elastic behavior of a lattice is described by its matrix of second-order elastic constants:

$$C_{ij} = \frac{1}{V_0}\left(\frac{\partial^2 E}{d\varepsilon_i d\varepsilon_j}\right) \tag{3.3}$$

The elastic energy (E) of a crystal can be expressed as a function of its equilibrium volume (V_0) and strain (ε). This energy is described by a 6 × 6 matrix, also known as the stiffness matrix, which contains 21 independent components. The specific crystal class of the material further imposes symmetrical constraints, reducing the number of independent elastic constants. For an arbitrary deformation represented by an infinitesimal strain, the crystal's energy can be represented by the following quadratic form:

$$E = E_0 + \frac{1}{2}V_0 \sum_{i,j=1}^{6} C_{ij}\,\varepsilon i \varepsilon j + O(\varepsilon^3) \tag{3.4}$$

A crystal is dynamically stable if the quadratic form representing its elastic energy is always positive ($E > 0, \forall\ \varepsilon \neq 0$) [173]. This is mathematically equivalent to the following Born stability criteria:

- The matrix C is positive definite.
- All eigenvalues of C are positive.
- All leading principal minors of C are positive (determinants of its upper-left k by k sub-matrix, $1 \leq k \leq 6$, Sylvester's criterion).

These conditions are valid for any crystal and are not linear. They imply some necessary but not sufficient conditions, such as all diagonal elements of C being positive ($C_{ii} > 0, \forall\ i$). Another example of necessary condition is.

$$(C_{ij})^2 < C_{ii}C_{jj} \forall i,j \tag{3.5}$$

This section focuses on expressing closed-form expressions for the necessary and sufficient elastic stability conditions for two Laue classes among seven. The Table 3.2 also provides the number of independent elastic constants for each class. The analysis is focused on three-dimensional crystalline systems but can be extended to one- or two- dimensions [174,175].

Table 3.2. Laue groups and number of independent second-order elastic constants C_{ij}.

Crystal system	Laue class	Point groups	C_{ij}'s
Cubic	m$\bar{3}$m	432, $\bar{4}$3m, m$\bar{3}$m	3
Hexagonal	6/mmm	6mm,622,$\bar{3}$2m,6/mmm	5
Rhombohedral	$\bar{3}$m	32,3m,$\bar{3}$m	6
Tetragonal	4/mmm	4mm,422,$\bar{4}$2m,4/mmm	6
orthorhombic	mmm	222,2mm, mmm	9
Monoclinic	2/m	2, m,2/m	13
Triclinic	$\bar{1}$	1,$\bar{1}$	21

The cubic crystal system has the simplest form of elastic matrix, with only *3* independent constants: C_{11}, C_{12} and C_{44}:

$$C_{cubic} = \begin{pmatrix} C_{11} & C_{12} & C_{12} & & & \\ . & C_{11} & C_{12} & & & \\ . & . & C_{11} & & & \\ & & & C_{44} & & \\ & & & & C_{44} & \\ & & & & & C_{44} \end{pmatrix} \tag{3.6}$$

(in this notation, dots are used to indicate nonzero elements constrained by the symmetric nature of the matrix). The three Born stability criteria for the cubic system are well-known: $C_{11} - C_{12} > 0; C_{11} + 2C_{12} > 0; C_{44} > 0$

They are necessary and sufficient. Here we merely note that the first two conditions imply that $C_{11} > 0$, so it needs not be noted as an extra condition, as is sometimes done. Also, the first condition can be equivalently stated as $C_{11} > |C_{12}|$.

3.4.2 Hexagon crystal system

The Laue class of the hexagonal crystal system, have the following form for the elastic matrix:

$$C_{hexagonal} = \begin{pmatrix} C_{11} & C_{12} & C_{13} & & & \\ . & C_{11} & C_{12} & & & \\ . & . & C_{33} & & & \\ & & & C_{44} & & \\ & & & & C_{44} & \\ & & & & & C_{66} \end{pmatrix} \quad (3.7)$$

Crystals of the hexagonal crystal system have only *5* independent elastic constants, due to the added relation:

$$C_{66} = (C_{11} - C_{12})/2 \quad (3.8)$$

By direct calculation of the eigenvalues of the stiffness matrix above, one can derive the following four necessary and sufficient conditions for elastic stability in the hexagonal and tetragonal (I) case:

$$C_{11} > |C_{12}|; 2C_{13}^2 < C_{33}(C_{11} + C_{12}) \quad (3.9)$$
$$C_{44} > 0; C_{66} > 0$$

(where the condition on C_{66} is redundant with the first one, for the hexagonal case).

3.4.3 Elastic stability in Two-Dimensional Materials

The elastic stiffness tensor relates the stress tensor and strain tensor through Hooke's law. The generalized Hooke's law expresses this linear relationship in terms of finite strain variables and elastic constants C_{ijkl} [172,176]

$$\sigma_{ij} = C_{ijkl}\epsilon_{kl} \rightarrow \sigma = C\epsilon \quad (3.10)$$

- σ represents the second-rank Cauchy stress tensor.
- C represents the fourth-rank anisotropic elastic stiffness tensor.
- ε represents the second-rank small strain tensor.

These equations are formulated in a three-dimensional (3D) context, where indices *i, j, and k* range from *1 to 3.* In a two-dimensional (2D) scenario, the indices *i, j, and k* would be limited to *1 and 2.* Additionally, it's worth noting that the Einstein summation convention is applied here, implying that repeated indices (in this case *i, j, and k*) are implicitly summed over in the calculations.

From the symmetry of *σ and ε* it follows that

$$C_{ijkl} = C_{jikl} = C_{ijlk} \tag{3.11}$$

and from the thermodynamic requirement of existing of a strain energy density function *U(ε)* (hyperelastic material) [177] such that

$$U = \frac{1}{2}\frac{\partial^2 U}{d\varepsilon_{ij} d\varepsilon_{kl}} \tag{3.12}$$

additionally

$$C_{ijkl} = C_{klij} \tag{3.13}$$

The number of independent components in the elastic stiffness tensor (C_{ijkl}) varies depending on the dimensionality.

- In 3D, the elastic stiffness tensor C is a fourth-rank tensor with 81 components. However, due to symmetries and relationships within the tensor, the number of independent components is reduced to 21 [178].
- In 2D, which is a plane stress or plane strain scenario, the elastic stiffness tensor C is a fourth-rank tensor with 36 components. Again, due to symmetries and relationships within the tensor, the number of independent components is further reduced to 6 [176,179,180].

Both the fourth-rank tensor notation and the Voigt notation can be used to represent the generalized Hooke's law, which relates stress and strain in elastic materials. In 2D, the Voigt notation uses a 3x3 matrix to represent the elastic stiffness.

The reduction in the number of independent components in lower dimensions simplifies the description of elastic behavior while capturing essential characteristics for the specific scenario (3D or 2D). This simplification is particularly valuable for analytical and computational purposes.

$$\begin{bmatrix}\sigma_{11}\\ \sigma_{22}\\ \sigma_{12}\end{bmatrix}=\begin{bmatrix}C_{1111} & C_{1122} & C_{1112}\\ C_{1122} & C_{2222} & C_{2212}\\ C_{1112} & C_{2212} & C_{1212}\end{bmatrix}\begin{bmatrix}\varepsilon_{11}\\ \varepsilon_{22}\\ 2\varepsilon_{12}\end{bmatrix} \tag{3.14}$$

or

$$\begin{bmatrix}\hat{\sigma}_1\\ \hat{\sigma}_2\\ \hat{\sigma}_3\end{bmatrix}=\begin{bmatrix}\hat{C}_{11} & \hat{C}_{12} & \hat{C}_{13}\\ \hat{C}_{12} & \hat{C}_{22} & \hat{C}_{23}\\ \hat{C}_{13} & \hat{C}_{23} & \hat{C}_{33}\end{bmatrix}\begin{bmatrix}\hat{\varepsilon}_1\\ \hat{\varepsilon}_2\\ \hat{\varepsilon}_3\end{bmatrix}\rightarrow \hat{\sigma}=\hat{C}\hat{\varepsilon} \tag{3.15}$$

The less popular is a second-rank tensor, called also orthonormal or Mandel, notation:

$$\begin{bmatrix}\sigma_{11}\\ \sigma_{22}\\ \sqrt{2}\sigma_{12}\end{bmatrix}=\begin{bmatrix}C_{1111} & C_{1122} & \sqrt{2}C_{1112}\\ C_{1122} & C_{2222} & \sqrt{2}C_{2212}\\ \sqrt{2}C_{1112} & \sqrt{2}C_{2212} & \sqrt{2}C_{1212}\end{bmatrix}\begin{bmatrix}\varepsilon_{11}\\ \varepsilon_{22}\\ \sqrt{2}\varepsilon_{12}\end{bmatrix} \tag{3.16}$$

Or

$$\begin{bmatrix}\sigma_1\\ \sigma_2\\ \sigma_3\end{bmatrix}=\begin{bmatrix}C_{11} & C_{12} & C_{13}\\ C_{12} & C_{22} & C_{23}\\ C_{13} & C_{23} & C_{33}\end{bmatrix}\begin{bmatrix}\varepsilon_1\\ \varepsilon_2\\ \varepsilon_3\end{bmatrix}\rightarrow \sigma=c\varepsilon. \tag{3.17}$$

The Voigt notation and the second-rank tensor notation differ in their fundamental representation of elastic properties. While the Voigt notation (Eqn 3.15), the elements of the matrix $\hat{C}$ are not the elements of a second-rank tensor, simplifies the mathematical representation of elastic properties in 2D dimensions, it does not adhere to the tensorial properties of a second-rank tensor. In contrast, the second-rank tensor notation (Eqn 3.17), the elements of the tensor *c* are indeed the elements of a second-rank tensor maintains the tensorial nature of the elastic properties, making it more suitable for representing elastic properties in higher dimensions.

The fourth-rank tensor notation (Eqn 3.10) and the second-rank tensor notation (Eqn 3.17) are mathematically equivalent [176,179,181], meaning they describe the same physical relationships and properties but use different mathematical representations. The choice between these notations depends on the specific problem and the desired analytical or computational convenience.

I. Oblique (parallelogram) ($a \neq b$, $\measuredangle \neq 900$),

II. Rectangular ($a \neq b$, $\measuredangle = 900$),

III. Centered rectangular or diamond ($a \neq b$, $\measuredangle = 900$),

IV. Square ($a = b$, $\measuredangle = 900$),

V. Rhombic or hexagonal ($a = b$, $\measuredangle = 1200$).

The intricate arrangement of atoms within a crystal, known as its crystallographic structure, gives rise to a fundamental property: symmetry. Symmetry dictates the geometric patterns and arrangements that characterize the crystal, and its influence extends to the material's physical properties.

- Symmetry Elements: The building blocks of crystal symmetry are symmetry elements, which include rotation axes, mirror planes, and inversion centers. These elements represent the ways in which the crystal structure can be transformed while preserving its overall form. The presence of these symmetry elements imposes constraints on the arrangement of atoms within the crystal lattice.
- Symmetry-Related Properties: The symmetry inherent in a crystal's structure extends to its physical properties. The electrical conductivity of a crystal, for instance, may exhibit directional dependence due to the crystal's symmetry. Similarly, optical properties like birefringence arise from the symmetry of the crystal lattice.
- Symmetry Constraints: Symmetry acts as a guiding principle, limiting the range of values that physical properties can assume. In crystals with high symmetry, certain components of the elastic stiffness tensor may become equal, reducing the number of independent elastic constants. Symmetry serves as a framework for understanding the range of possible physical properties for a given crystal.
- Curie's Principle: Curie's principle establishes a fundamental relationship between the symmetry of a physical property and the symmetry of the crystal. It states that the symmetry of a physical property cannot be lower than the symmetry of the crystal itself. In essence, the crystal's symmetry provides a lower bound for the symmetry of any physical property it exhibits.
- Higher Symmetry: While Curie's principle sets a lower bound, it is possible for physical properties to possess higher symmetry than the crystal itself. This occurs when the physical property, influenced by interactions or other factors, exhibits additional symmetries not explicitly present in the crystal lattice. For example, the optical properties of a crystal might exhibit higher symmetry due to the alignment of molecules or domains within the crystal.

Symmetry principles are fundamental in the study of physical properties in crystalline materials. They provide valuable insights into how the arrangement of atoms in a crystal lattice influences the behavior of physical properties of the material may not be lower than the symmetry of the crystal, but may be higher [182,183].

The classification of linear elastic materials is based on the mathematical properties of fourth-rank Euclidean symmetric tensors [184] which describe the linear relationship between stress and strain in these materials. This classification is independent of the crystal structure or symmetry of the material.

The behavior of linear elastic materials is governed by the symmetrical properties of their elastic stiffness tensor [184] This classification system, independent of material crystal structure or symmetry, categorizes three-dimensional (3D) materials into eight distinct elastic symmetry classes, each representing a unique response to mechanical deformation. In contrast to their 3D counterparts, two-dimensional (2D) linear elastic materials exhibit a reduced number of symmetry classes, with only four distinct categories recognized [179,184] This reduction stems from the inherent dimensionality difference between 2D and 3D materials, limiting the possible symmetries that the elastic stiffness tensor can possess. The Born stability conditions, a set of mathematical inequalities derived from the requirement of bounded total crystal energy, play a crucial role in assessing the stability of 3D crystals. These conditions ensure that the elastic constants of a crystal satisfy specific constraints, guaranteeing its mechanical stability [185]. While the Born stability conditions are well-established for 3D crystal systems, their extension to 2D systems remains an active area of research to necessitate further exploration and development of appropriate mathematical frameworks to accurately describe their mechanical and elastic behavior.

In general, an unstressed crystalline structure is considered stable, meaning it can maintain its shape without deformation and in the harmonic approximation when two conditions are met:

- All its phonon modes have positive frequencies $\boldsymbol{\omega}$ for all wave vectors $\boldsymbol{q}$ (dynamical stability):

$$\boldsymbol{\omega^2(q)} > 0 \tag{3.18}$$

- The strain energy density function, given by the quadratic form (Eqn 3.10), is always positive (elastic stability):

$$U(\varepsilon) > 0, \forall \varepsilon \neq 0 \tag{3.19}$$

In mathematical elasticity, the condition related to phonons in this context is referred to as "strong ellipticity." It's crucial to understand that strong ellipticity does not imply the positive definiteness of the strain energy density function (as represented in Eqn 3.9). In fact, the implication goes the other way. In simpler terms, while these conditions may appear similar or related, they actually have distinct implications and should not be confused with one another [178].

Determining the positive definiteness of the quadratic form in (Eqn 3.19) can be a complex task. However, there are alternative, equivalent conditions that offer simpler verification, as described by [185]

- Eigenvalue Criterion: All eigenvalues of the tensor $\boldsymbol{c}$, expressed in second-rank tensor notation (Eqn 3.17), must be positive.

- Sylvester's Criterion: All leading principal minors of the tensor c, as defined in (Eqn 3.17) (the determinants of its upper-left k by k submatrices), must be positive.

The elastic stiffness tensor $\boldsymbol{c}$ and the stability conditions for 2D materials vary depending on the symmetry class. Specifically, the independent elastic constants and Born stability conditions for five 2D plan Bravais (see Figure 3.4) lattices are listed as follow [176]:

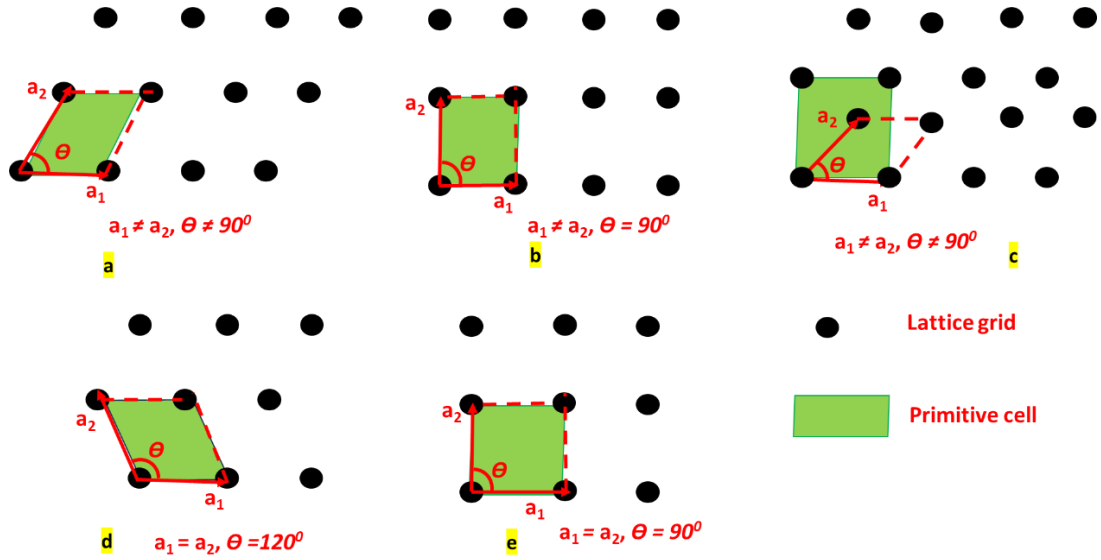

Figure 3.4 Five types of 2D Bravais lattices. (a–e) are oblique, primitive rectangular, centered rectangular, hexagonal, and square, respectively.

- Full symmetry (isotropy) → Hexagonal lattice (V) (2 elastic constants)

$$C_{ij} = \begin{bmatrix} C_{11} & C_{12} & 0 \\ C_{12} & C_{22} & 0 \\ 0 & 0 & C_{11} - C_{12} \end{bmatrix} \tag{3.20}$$

$$C_{11} > 0 \text{ and } C_{11} > |C_{12}|$$

- Symmetry of a square, (tetragonal) → Square lattice (IV) (3 elastic constants)

$$C_{ij} = \begin{bmatrix} C_{11} & C_{12} & 0 \\ C_{12} & C_{22} & 0 \\ 0 & 0 & C_{33} \end{bmatrix} \tag{3.21}$$

$$C_{11} > 0 \text{ and } C_{33} > 0 \text{ and } C_{11} > |C_{12}|$$

- Symmetry of a rectangle, (orthotropy)→ Rectangular (II) & centered rectangular lattice (III) (4 elastic constants)

$$C_{ij} = \begin{bmatrix} C_{11} & C_{12} & 0 \\ C_{12} & C_{22} & 0 \\ 0 & 0 & C_{33} \end{bmatrix} \tag{3.22}$$

$$C_{11} > 0 \text{ and } C_{33} > 0 \text{ and } C_{11}C_{22} > C_{12}^2$$

- No symmetry (anisotropy) → Oblique lattice (I) (6 elastic constants)

$$C_{ij} = \begin{bmatrix} C_{11} & C_{12} & C_{13} \\ C_{12} & C_{22} & C_{23} \\ C_{13} & C_{23} & C_{33} \end{bmatrix} \tag{3.23}$$

$$C_{11} > 0 \text{ and } C_{11}C_{22} > C_{12}^2 \wedge detC_{ij} > 0$$

After the theoretical introduction, I turn my attention to how to calculate elastic constant *C* via state-of-the-art atomistic based Molecular static calculation. Here, I take the hexagonal lattice as an example to show how to calculate the independent elastic constant based on the energy– strain approach. It should be noted that the nature of this problem is to solve the linear equation. For the squared lattice, there are 3 independent elastic constants (C_{11}, C_{12} and C_{66}), which means that we need at least 3 equations to solve this problem.

3.5 Elastic constants of monolayer MoS_2 using molecular statics (MS)

Molecular statics calculations have been performed using LAMMPS code to generate the elastic constants of MoS_2 at 0K. We know that the MoS_2 sheet consists of a tri-layer, and it experiences strong covalent bonding inward and weak van der Waal's interaction over the tri-layer due to the polarization effect [186]. The elastic properties of MoS_2 are determined as the derivative of the stress against the external strain according to Hooke's law. The generalized Hooke's law, for the number of independent elastic constants in MoS_2, is three and can be written as

$$\sigma_{ij} = C_{ijkl}\,\xi_{kl} \tag{3.24}$$

In Voigt notation, the stress–strain relation is.

$$\sigma_i = \sum_{j=1}^{6} C_{ij}\varepsilon_j \tag{3.25}$$

There are three independent elastic constants for MoS_2, i.e., C_{11} is the coefficient of elastic constant relations due to σ_{11} and ε_{11} similarly for C_{22}, and C_{12}. The C_{ij} values are correlated to the equal volume of the MoS_2 unit cell. Therefore, the vacuum space has been set up large enough in the z-axis to avoid the interlayer interactions in MoS_2 monolayer; the C_{ij} constants then have to rescaled z = t_0 to the actual thickness of monolayer MoS_2. So, we have set t_0 = 6.15 Å, i.e., one half of the out-of-plane lattice constant of bulk MoS_2. The MoS_2 structure is fully optimized to its minimum energy by conjugate gradient minimization until the energy is converged. The specific finite lattice distortion of the simulation box leads to a change in energy during convergence, and the respective final elastic constants are obtained [187,188].

The second-order elastic constants for elastic matrix express as:

$$C_{ij} = \frac{1}{A_0 t_0}\left(\frac{\partial^2 E}{d\varepsilon_i d\varepsilon_j}\right) \tag{3.26}$$

Where A_0 is the area of the sample, t_0 represents the thickness of MoS_2 monolayer, E is the elastic energy, and ε is the strain tensor. In polynomial form for 2D materials discussed in [185,188] the elastic energy $E(\varepsilon)$ of MoS_2 is expressed as

$$E(\varepsilon) = \frac{1}{2} C_{11} \varepsilon_{xx}^2 + \frac{1}{2} C_{22} \varepsilon_{yy}^2 + C_{12} \varepsilon_{xx} \varepsilon_{yy} \tag{3.27}$$

The ε_{xx} and ε_{yy} are the longitudinal strain in *x* and *y* directions and can also be represented as ε_1 and ε_2 respectively in terms of Voight notations, and ε_{xy} is the applied shear strain in *xy* plane. The MoS_2 sheet is arranged as zigzag and armchair in the x and y-axis. $\varepsilon_{ij's}$ and $C_{ij's}$ are the corresponding infinitesimal strain tensors and linear elastic constants [188,189]. Born set the benchmark mechanical stability for materials, which explains $C_{11} > 0$, $C_{11} > C_{12}$, and $C_{12} > 0$ and the condition to satisfy for the 2D materials to be isotropic is $C_{11} \approx C_{22}$ and C_{12}. The elastic energy in 2D materials for finite distortion is expressed as

$$\mathrm{E}\,(\varepsilon) = \frac{1}{2}(\varepsilon_1 \varepsilon_2 \varepsilon_6) = \begin{bmatrix} C_{11} & C_{12} & C_{16} \\ . & C_{22} & C_{26} \\ . & . & C_{66} \end{bmatrix} \begin{Bmatrix} \varepsilon_1 = \varepsilon_{11} \\ \varepsilon_2 = \varepsilon_{22} \\ \varepsilon_6 = 2\varepsilon_{12} \end{Bmatrix} \tag{3.28}$$

After the MoS_2 sheet is perfectly relaxed or energy is fully converged, the independent elastic constants are extracted for respective strains.

3.6 Results and Discussion

3.6.1 MoS_2 sheet with pristine and random vacancy defects

The findings show that the elastic constants for a MoS_2 sheet with an infinite system size are $C_{11} = C_{22} = 149.42$ *N/m*, $C_{12} = 52.29$ *N/m*, which interpret the isotropic nature of the material. One such example of MoS_2 microstructure with no defects is shown in Figure 3.5. The OVITO [190] was used for visualization of results.

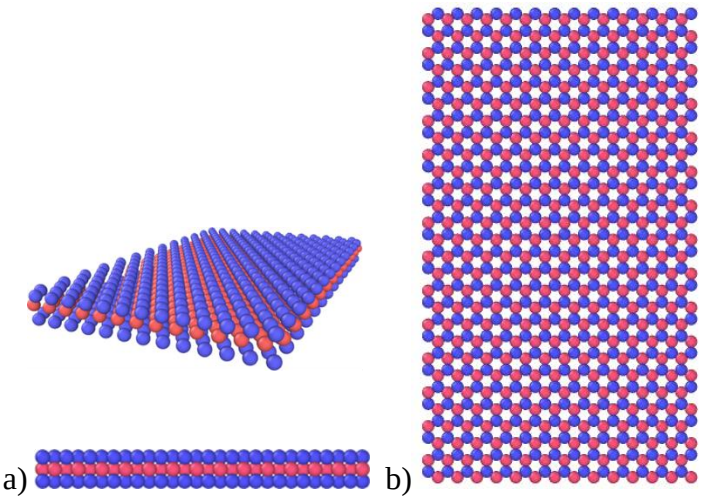

Figure 3.5 The atomistic model of monolayer MoS_2 without defects, blue balls represent Sulfur atoms top and bottom layers and red balls represent Molybdenum. The elastic constants for this pristine MoS_2 are $C_{11} = C_{22} = 149.42$ N/m, $C_{12} = 52.29$ N/m

Since the independent elastic constants for a 2D material MoS_2 are three within the notation employed, the constant elastic tensor is a 3x3 symmetric matrix. Due to symmetry, the nine matrix elements will get reduced to three independent elements. The calculated elastic constants of MoS_2 are shown in Table 3.3.

Table 3.3. Mechanical properties of MoS_2

	C_{11} (N/m)	C_{22} (N/m)	C_{12} (N/m)
This work	149.42	149.42	52.29
Bertolazzi et al. [8]	180±60	180±60	-
Li. M *et al* [19]	148.4	148.4	42.9
Nguyen *T.H et al* [28]	130.4	130.4	26.5

All elastic constants C_{ij} calculated by conjugate gradient minimization using molecular statics simulation in comparison with literature results are given in Table 3.3. Due to symmetry $C_{11} \approx C_{22}$ the obtained elastic constants marginally diverse from the reference data. We can see that $C_{11} = 149\ N/m$, which corresponds to a good Young's modulus of 242 Gpa. Bertolazzi et al. [50] reported the elastic stiffness of MoS_2 monolayer is 180 ± 60 N/m, which corresponds to a good Young's modulus of 270±100 GPa by atomic force microscope (AFM) experiment method. The experimental results are higher than our simulation results from this study because in AFM method, tip enforced on the sheet consists of monolayer or multilayer MoS_2 suspended on the layer incorporate with an array of circular holes are under biaxial tensile stress whereas we have applied uniaxial stress to the monolayer. Li et al. [167] performed MD simulation under the uniaxial test presented that C_{11} is found to be 199 GPa for the 1H MoS_2, our results are while Nguyen T.H. [191] obtained an average young's modulus of 201 GPa for monolayer MoS_2. Note that the deviation is because they performed DFT calculations which are derived from finite difference approach by Thermo-pw code, and we have used the latest SW potential which can be used for higher temperature as well. A comparison of elastic constants from this work is consistent with the experimental and simulation results. Regardless of vacancies, the average value of C_{12} and C_{21} is used to assess the physical properties of MoS_2. It is apparent that $C_{12} \approx C_{21}$ due to the symmetric stiffness matrix.

I now describe the effects of modeling monolayer MoS_2 sheet with randomly distributed defect fraction presented in Figure 3.6 The geometry optimized average elastic constants for MoS_2 under different defect fractions are given in Table 3.4. The elastic constants of monolayer MoS_2 vs. the defect percentage are illustrated in comparison to the perfect MoS_2 sheet. The MoS_2 monolayer sheet is arranged as zigzag and armchair in x & y directions, which denotes the C_{11}, C_{22} *and* C_{12} elastic

moduli, respectively. It is clear that chirality slight effect on elastic constants irrespective of defect ratios. The elastic constants C_{ij} nonetheless started dwindling as the defect fraction piling up from 0 to 25%. Its reduction becomes more expeditious as the defects grow in the sheet. I kept piling up the defect fraction and maximum ratio up to 25% results in a considerable decline in the elastic constants, which implies the impact is significant.

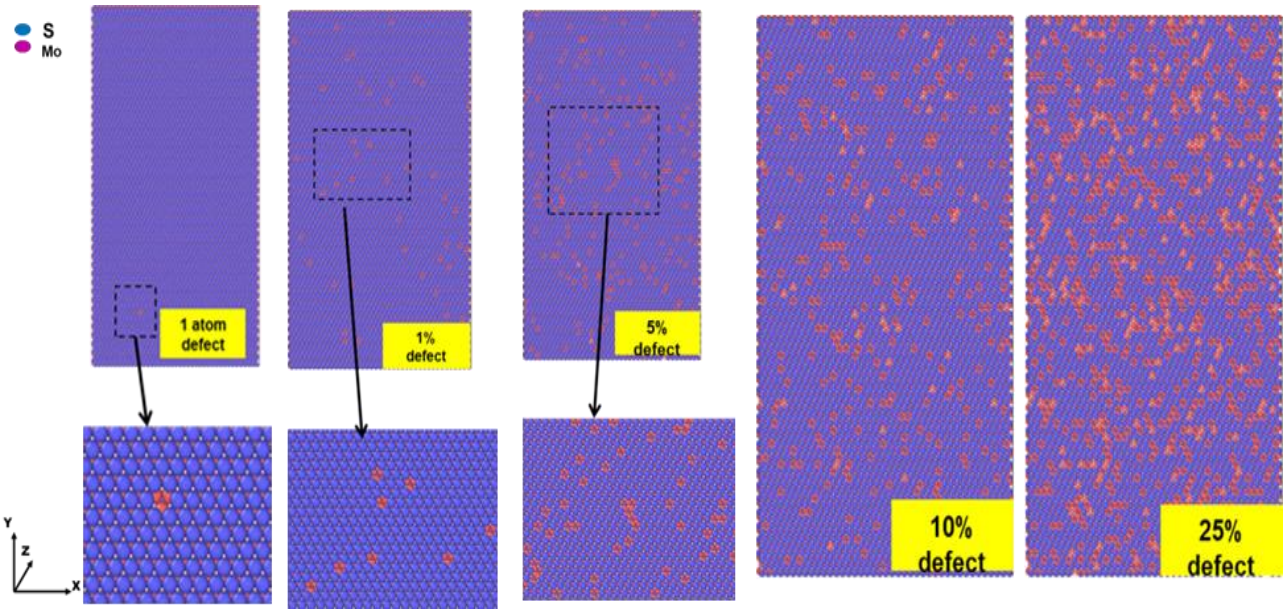

Figure 3.6 The atomistic model of monolayer MoS_2 with different percentage of defects.

Table 3.4. The mechanical parameters for MoS_2 for different defect fractions along with Standard Deviation (SD).

% of Defects	C_{11} [N/m]	SD of C_{11}	C_{22} [N/m]	SD of C22	C_{12} [N/m]	SD of C12
Pristine MoS_2	149.42		149.42		52.29	
Only 1-atom defect	149.11	0.1070	149.04	0.1075	52.23	0.0460
1%	149.01	0.4758	148.85	0.4935	52.15	0.2185
2%	140.70	0.7898	141.51	0.7638	48.52	0.3836
5%	128.89	1.0179	128.89	1.1328	43.25	0.5485
10%	108.30	1.5842	107.94	1.7279	33.70	1.0182
15%	94.21	2.2419	93.47	2.2325	28.75	1.4486
20%	80.99	3.5597	78.46	3.2201	23.16	2.4461
25%	61.15	3.2207	51.52	3.2868	10.67	2.2325

The elastic constants of monolayer MoS_2 nanosheet vs. the defect percentage are presented in Figure 3.7. The dots denote average values of defects fraction with the fluctuating bar represents the standard deviation that shows maximum and minimum values for hundreds of cases with random distributed defects. The result of chirality on the elastic properties of MoS_2 is negligible, despite the prevailing circumstances of the defect fraction. The elastic constants dwindle faster with the increase in the defect fraction, the maximum reduction of elastic constants is at 25%, more significant than 15%, 10%, 5%, this implies the influence of defect fraction on the elastic constants is found to be substantial.

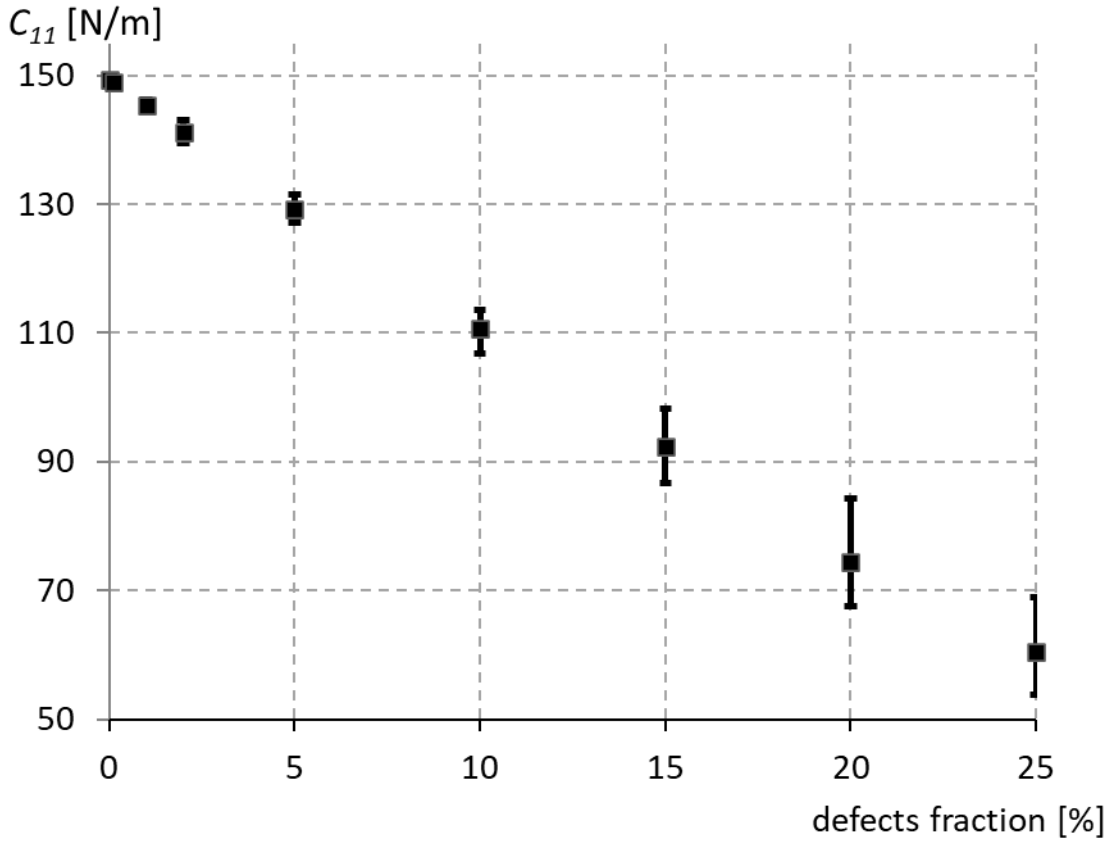

a)

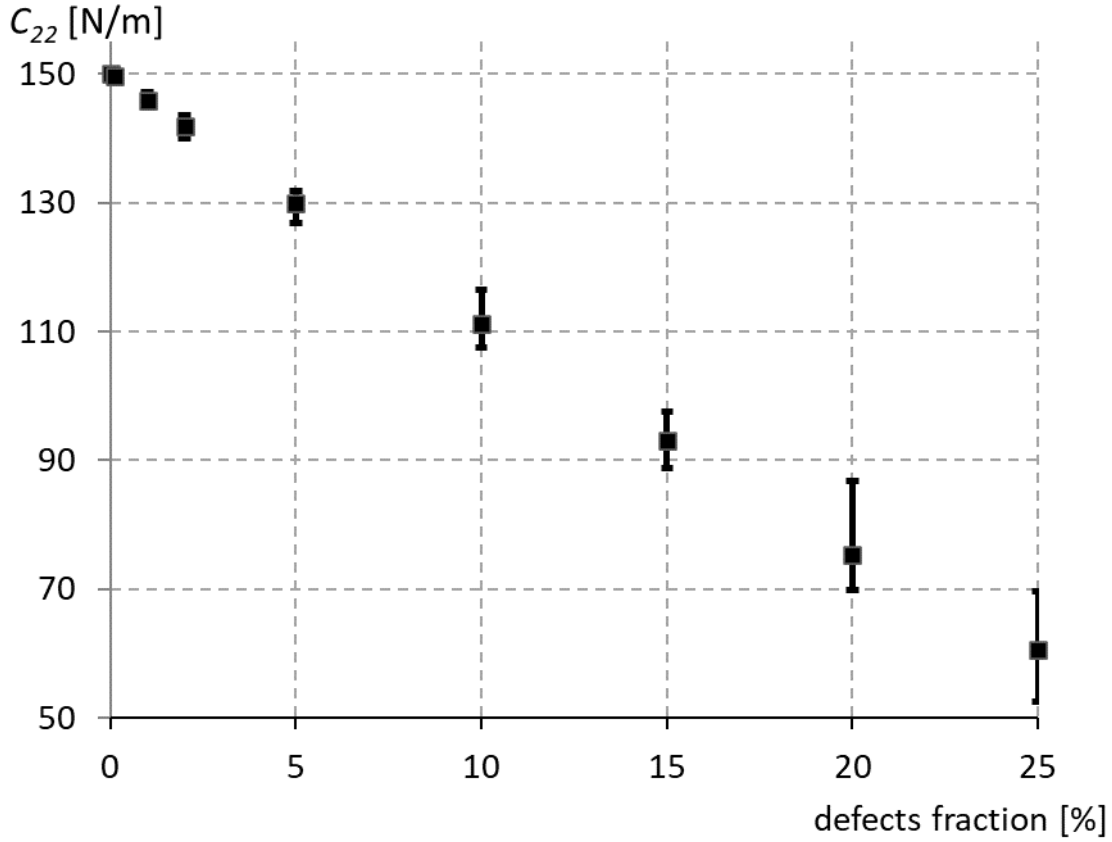

b)

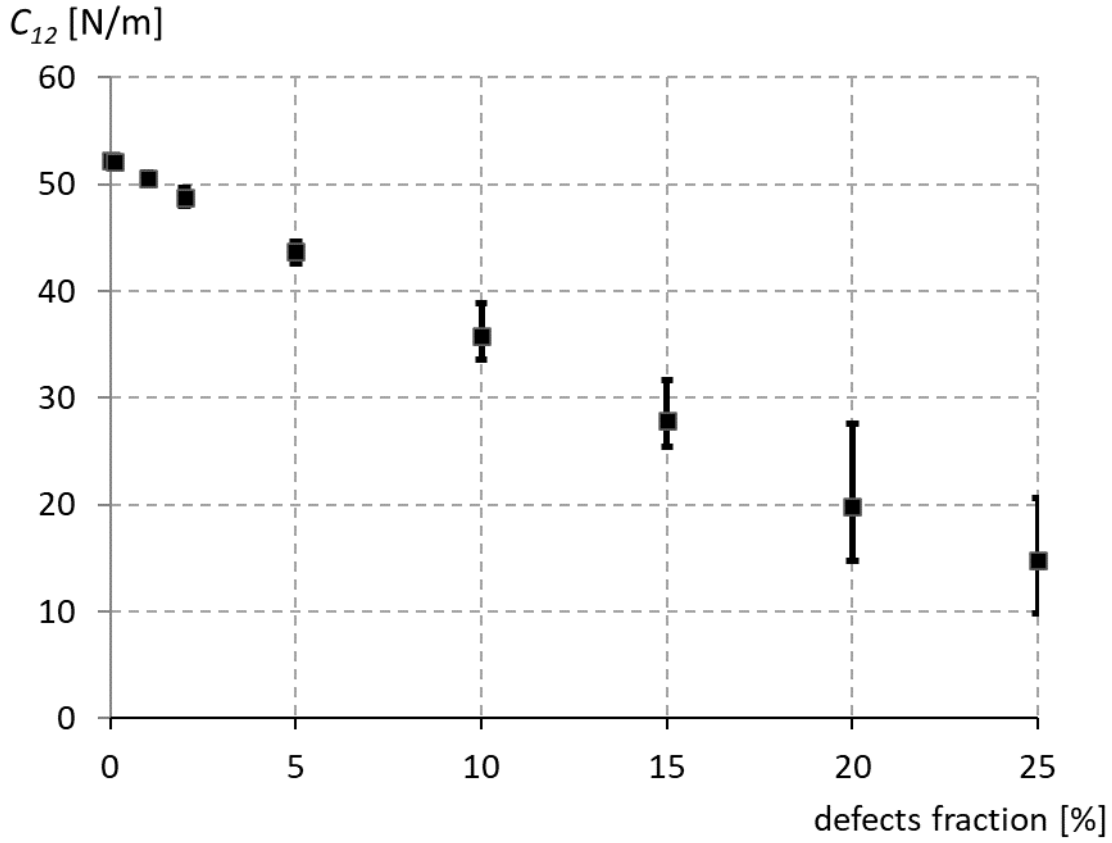

c)

Figure 3.7 The elastic constants of MoS_2 as a function of the defect fraction: a) C_{11}, b) C_{22}, c) C_{12}

To give comprehensive and comparable studies of elastic properties of randomly distributed defects, the elastic constants of MoS_2 with varying defect ratios have been studied. The elastic constants of this defective MoS_2 versus defect fraction are shown in Figure 3.7. For comparison, the elastic constant of pristine MoS_2 is also included in the plots. Figure 3.7 shows the effect of defects on the elastic constants of MoS_2 along with the individual independent elastic constants by comparing that of the pristine MoS_2. It will be hard to conclude the locations of the unperturbed vacancies as they are distributed randomly throughout the layer. We took an interest in determining that these vacancies need to formed everywhere in the sheet irrespective of defect fraction ratio. So, to achieve this, we repeated with different random seeds for a sufficient number of times and estimated the elastic constants for each seed.

Table 3.4 displays the average values of the outcomes of the built-in elastic test after repeating the simulation. These results will also motivate us to study the tensile and other properties of MoS_2 with the defects. With the increase in defect ratio, we observe the difference in the elastic constants nonlinearly as expected. It was found that up to 1% of defects had little impact as it trims down to 2.1% rate of elastic constants when compared to defect-free MoS_2 and the impact of this vacancy defects on the elastic constants was not that obvious and can be neglected. When the defect fraction surpasses to 2% and beyond, the elastic constants start trimming down at a rapid rate. Nevertheless, when defect ratios were 2%, 5%,10 %, and 25%, the decrease of the elastic constants was 4.02%, 13.42%, 28.8% and 56.5%, respectively, compared with MoS_2 with no defects. This result showed that after exceeding some defect density, the vacancy had a substantial effect and damages the robustness and uniform symmetry of MoS_2 and has a full impact on the elastic tensile behavior of MoS_2. It was also found that from Figure 3.7 as the elastic constants fluctuate within a certain range, this fluctuation occurs due to the locations of the defects placed randomly and changes its location with each test. These results draw attention towards the foundation in randomly distributed vacancies in MoS_2 sheets.

3. MoS_2 sheet with randomly diffusing sulfur to molybdenum (S→Mo)

The concentration of antisite defects, i.e., sulfur atoms to molybdenum atoms, are also randomly distributed in sulfur layers of the MoS_2 sheet.

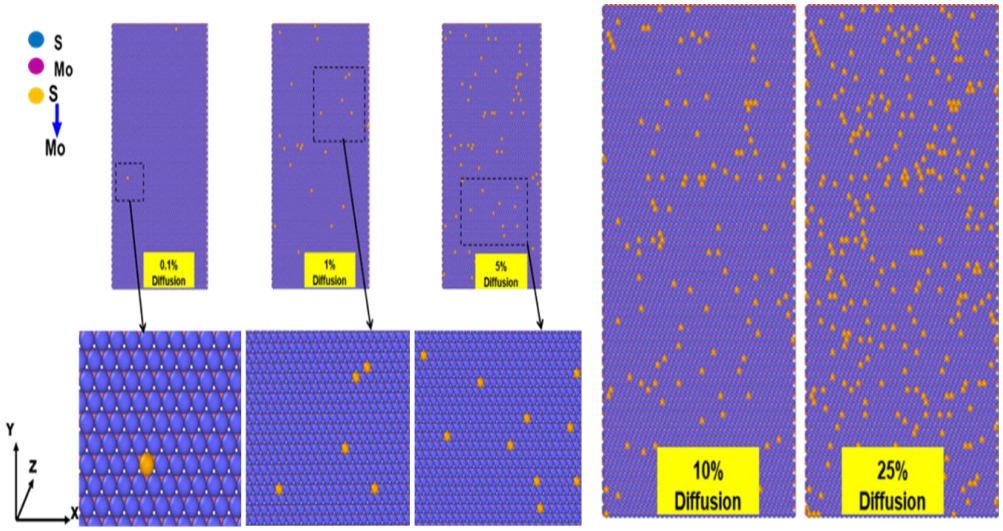

Figure 3.8 The atomistic model of monolayer MoS_2 with different percentage of antisite defects

Table 3.5. The geometry optimized structural parameters for MoS_2 for different defect fractions of antisite defects along with Standard Deviation (SD)

% of Diffusion	C_{11} [*N/m*]	SD of C11	C_{22} [*N/m*]	SD of C22	C_{12} [*N/m*]	SD of C12
% w/o diffusion	149.42		149.42		52.14	
0.1% S→Mo	147.03	0.0996	147.77	0.2300	51.29	0.0658
1% S→Mo	145.82	0.3224	146.60	0.5541	50.77	0.1621
2% S→Mo	143.98	0.4166	145.24	0.5991	50.38	0.1886
5% S→Mo	139.69	0.6203	140.10	0.6698	48.39	0.2296
10% S→Mo	133.91	0.8259	136.61	0.9077	46.04	0.2725
15% S→Mo	127.40	0.9695	128.76	0.9829	41.25	0.3107
20% S→Mo	118.75	0.9553	121.41	0.9556	36.62	0.3009
25% S→Mo	61.15	1.016	51.52	0.9981	10.67	0.3607

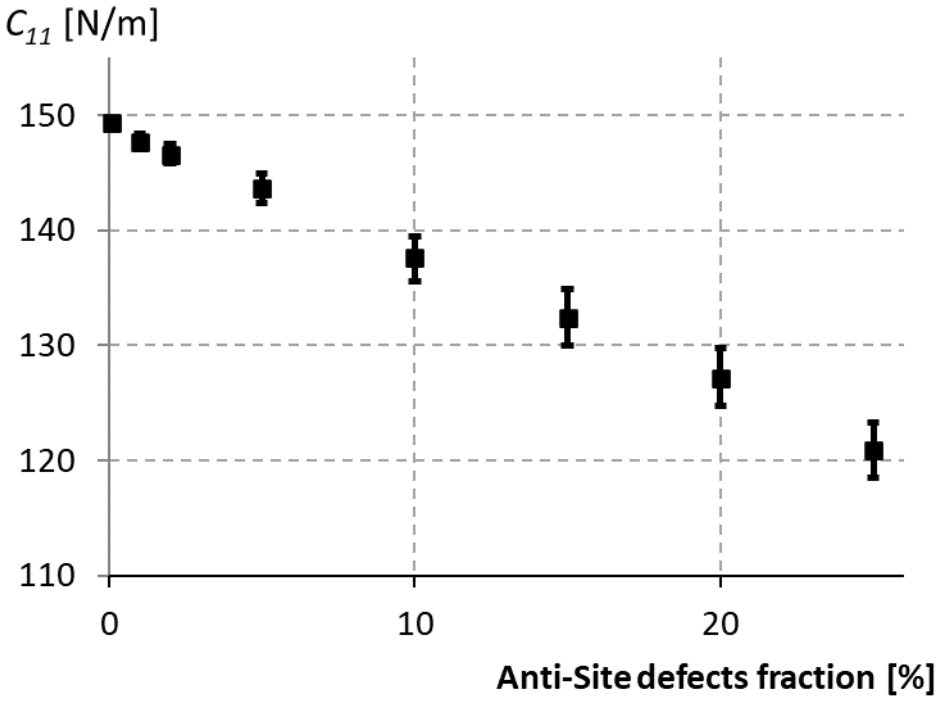
C_{11} [N/m]
150
140
130
120
110
0
10
20
Anti-Site defects fraction [%]

a)

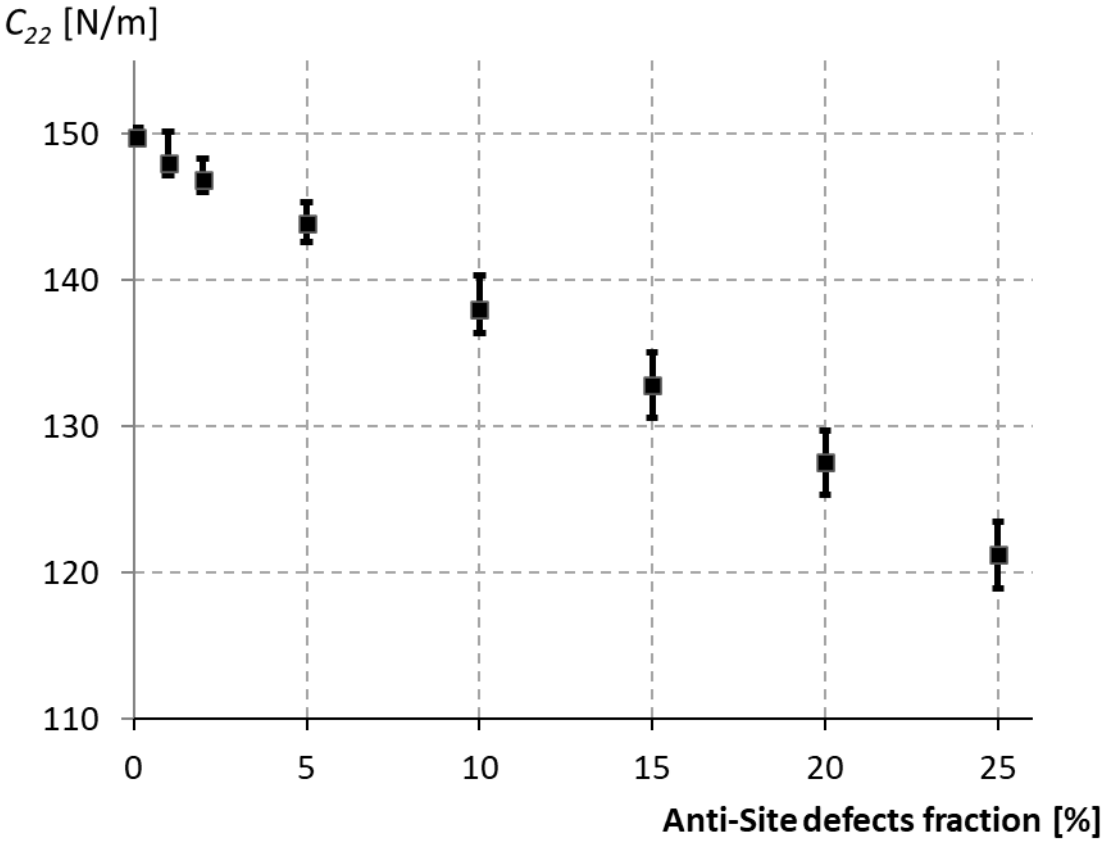
C_{22} [N/m]
150
140
130
120
110
0
5
10
15
20
25
Anti-Site defects fraction [%]

b)

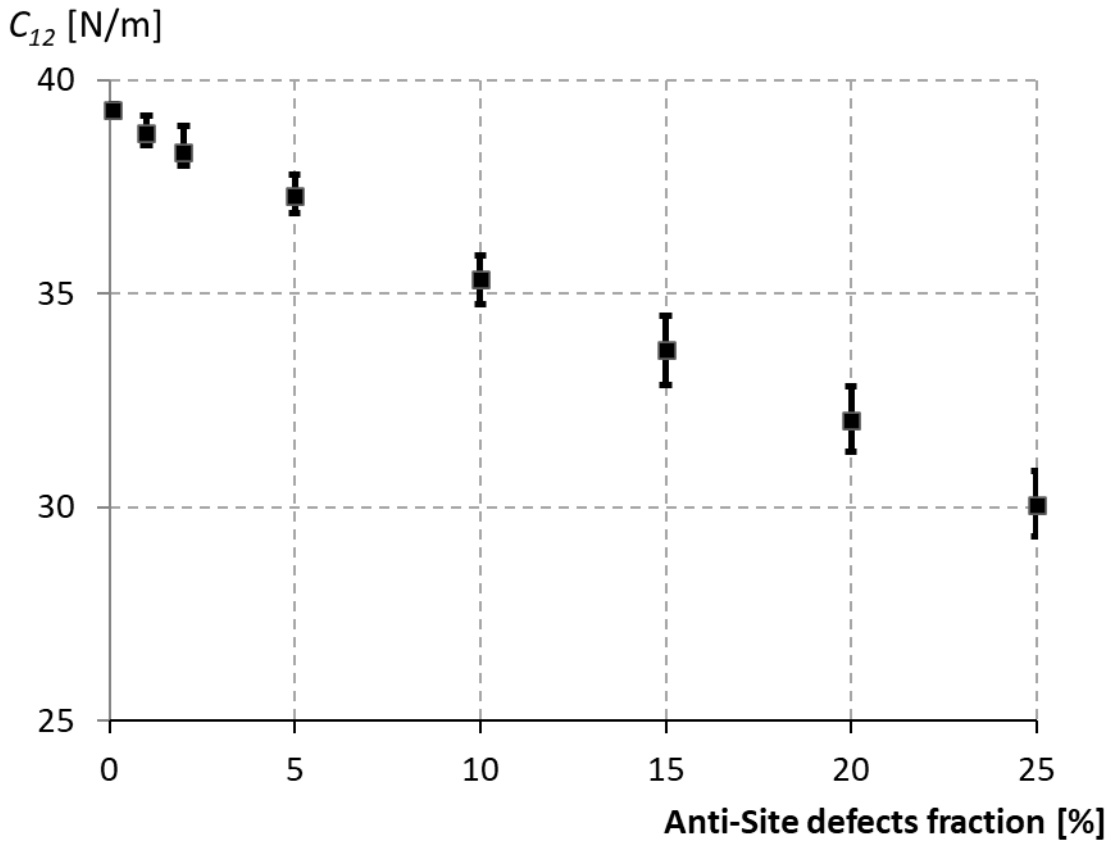

c)

Figure 3.9 The elastic constants of MoS_2 as a function antisite defect fraction: a) C_{11}, b) C_{22}, c) C_{12}

Figure 3.8 shows the diffusion of sulfur to molybdenum as antisite defect for different percentages of sulfur diffused in monolayer MoS_2 for 25000 atoms nanosheet size. Table 3 shows that the elastic stiffness strengths of 0% to 25% molybdenum doped in sulfur layers in monolayer MoS_2 for sheet size of 65 Å x 65 Å (25000 atoms) increase by about 0.1%, 2 %, 1 %, 5% and an impressive peak of 25% when compared with the MoS_2 is observed. The independent elastic constants of 1%, 2%, 5%, 10% as well as 15% sulphur doped molybdenum in MoS_2 drops by about 1%, 1.5%, 4%, 8%, 11.%, 15%, 19% in comparison to the pristine MoS_2. Increasing the percentage of sulfur doping in the MoS_2 sheet, the elastic properties decrease. Further, it is found that the elastic properties due to sulfur vacancy defects with different percentages drop in great detail when compared the elastic properties due to diffusion at the respective percentage as deduce from Table 3.4 and Table 3.5.

Figure 3.9 shows the effect of antisite defects molybdenum diffusion in sulfur, also dwindle the elastic constants of MoS_2 for the different defect fractions. The change of fractions was in ranges from 0.1 to 25% antisite defects. We started to pile-up the antisite defects and observed the elastic constants becomes more efficient and started to hinder further with the increase in the diffusion, unlike in case of pure defects where we see the elastic properties drop dramatically with each defect fraction. The

elastic constants C_{ij} of antisite defect also shows the trend of decrease in nature when compared to defect-free structure, it decreases from 139.69 N/m for 5% defects to 113.83 N/m for 25 % defects when compared to the of pure defects as seen in Table 3.5. In order to provide the results of impact of the antisite defect in MoS_2 sheet, again we prepared the random antisite defects models. The hundreds of replications were considered for MoS_2 with 0 to 25% antisite defects.

3.7 Summary

The elastic constants for MoS_2 monolayer using molecular statics simulation in great detail were investigated. MoS_2 is flexible and isotropic for small deformations and the results obtained from this study are compared with the previous literature for defect-free MoS_2 and progress towards higher defect fractions. he random distribution of defects in the MoS_2 sheet in addition to antisite defects were also discussed in great detail.

We have seen that the elastic constants of MoS_2 started dwindling at a rapid rate with the defects pile-up. It started to dwindle at a slow rate of up to 1% of defects. Just as the defects increased to 2% and beyond, its reduction began dramatically. Hence when the defect percentage reaches 10%, the reduction in elastic constants was as huge as 28.8%. These vacancies defects greatly influenced the elastic behavior of the MoS_2 lattice. With the increase in defects fraction, the vector sum of displacement has affected the geometrical symmetry of the MoS_2 sheet. Moreover, in this study, we review the possibility of physical properties improvement and strengthening the elastic stiffness properties due to defects in MoS_2 was confirmed.

Chapter 4

Bioinspired Evolutionary Algorithm in Optimization of monolayer MoS_2

The challenges in technology often boil down to the quest for materials with specific and often undiscovered properties. Experimentation is one way to seek out and understand these new materials. However, it can be an arduous, expensive, and sometimes unfeasible process. Computational methods offer a valuable alternative to traditional experimentation for discovering new materials with desired properties [192]. They provide several advantages, including reduced time and cost, improved understanding of materials, and exploration of new conditions. Chapter 3 discussed the influence of point defects on the mechanical properties of monolayer MoS_2, highlighting the importance of computational methods for understanding and designing new 2D materials.

The chapter focuses on the design of nanostructures with prescribed mechanical properties, utilizing an approach that integrates Evolutionary Algorithms (EAs) with molecular dynamics for optimizing the design of nanomaterials. The study aims to determine the optimal size of voids within monolayer 2D MoS_2 nanostructures to achieve prescribed elastic properties. The approach integrates Evolutionary Algorithms with molecular dynamics simulations to optimize the material design. The Evolutionary Algorithm, a metaheuristic optimization technique inspired by natural selection, is used for solving complex problems related to the design of nanomaterials. In this case, it is employed to guide the identification and sizing of voids within 2D MoS_2 nanosheets.

The significance of this study lies in the demonstrated capability of the proposed method to accurately achieve nanostructures with predefined mechanical material properties by strategically introducing elliptical voids within the 2D MoS_2 nanosheets. This method enables the controlled manipulation of the mechanical properties of these materials, offering potential advancements in tailoring material behavior for specific applications.

4.1 Introduction

In the realm of nanotechnology, the demand for materials with tailored properties is ever-increasing. Monolayer 2D molybdenum disulfide (MoS_2) nanomaterial has emerged as a promising candidate due to its exceptional mechanical, electrical, and chemical properties. Researchers are actively exploring MoS_2's potential applications in various fields, including desalination, DNA sequencing, and power generation [193–199].

Understanding the properties and behavior of monolayer MoS_2 is crucial for introducing this material into novel applications. However, one of the challenges is that fabricated MoS_2 sheets often contain defects, including nanopores [200,201]. The presence of defects can significantly influence the material's properties and performance, making it essential to study and account for these defects in practical applications. Researchers are working to accurately predict and control MoS_2 behavior, considering these defect-related factors.

4.1.1 Void Defects in MoS_2: Toward Nanopore Devices

Two-dimensional (2D) materials containing void defects are a promising substitute for conventional nanopore membranes like silicon nitride. void defects on 2D materials, as atomically thin nanopore devices, have been used in such as DNA sensor, gas sensor and purifier at lab-scale.

Molybdenum disulfide (MoS_2) due to its semiconducting properties, making it favorable for various applications in sensing and electronics [202–204]. MoS_2 nanopore membranes, particularly in the 2H structure, have shown promise as DNA detection sensors. Unlike graphene nanopore membranes, MoS_2 nanopores demonstrate superior performance in transverse DNA detection without requiring specific surface treatment processes to prevent interaction between DNA and the surface.

MoS_2 is commonly found in nature in 2H form, among other polytypes such as 1T and 3R [205]. Synthesized MoS_2 films might possess 3R structures, but most studies on MoS_2 defects have been performed using exfoliated MoS_2, typically in the 2H structure. The top and side views of 2H MoS_2 illustrate its atomic arrangement. The creation of the smallest void in 2H MoS_2 can be achieved by the removal of one Mo atom or two S atoms. However, it's noted that a higher concentration of sulfur site (S site) Nano-voids compared to molybdenum site (Mo site) Nano-voids is observed in transmission electron microscopy (TEM) due to different knock-on thresholds between sulfur and molybdenum atoms [163].

Figure. 4.1 displays sequential images showing MoS_2 void defects created by an 80 kV electron beam in a transmission electron microscope (TEM). Notably, the knock-on thresholds for S and Mo atoms are 80 kV and 560 kV, respectively. Consequently, S vacancies are formed first due to the slightly focused electron beams, as Mo atoms are less likely to be ejected by an 80 kV electron beam. This leads to the agglomeration of Mo atoms at the edge of the void defects. The images in Figure illustrate the increasing aggregation of Mo atoms at the void's edge under continued electron beam irradiation. While a few papers have reported the phenomenon of Mo atom agglomeration [206,207], none have detailed the corresponding effects on electrical or magnetic properties at the edge.

Theoretical calculations suggest that at S vacancy sites, Mo-Mo metallic bonds are formed, canceling the magnetism by pairing the unsaturated spin electrons [160]. Therefore, the degree of Mo atom

agglomeration might affect the material's metallicity and, consequently, the electrical performance, such as the current signals when DNA or molecules traverse the Nano-voids. Consequently, to optimize MoS_2-based nanopore devices, a comprehensive understanding of the edge configuration of MoS_2 void defects and their impact on electrical and magnetic properties is essential.

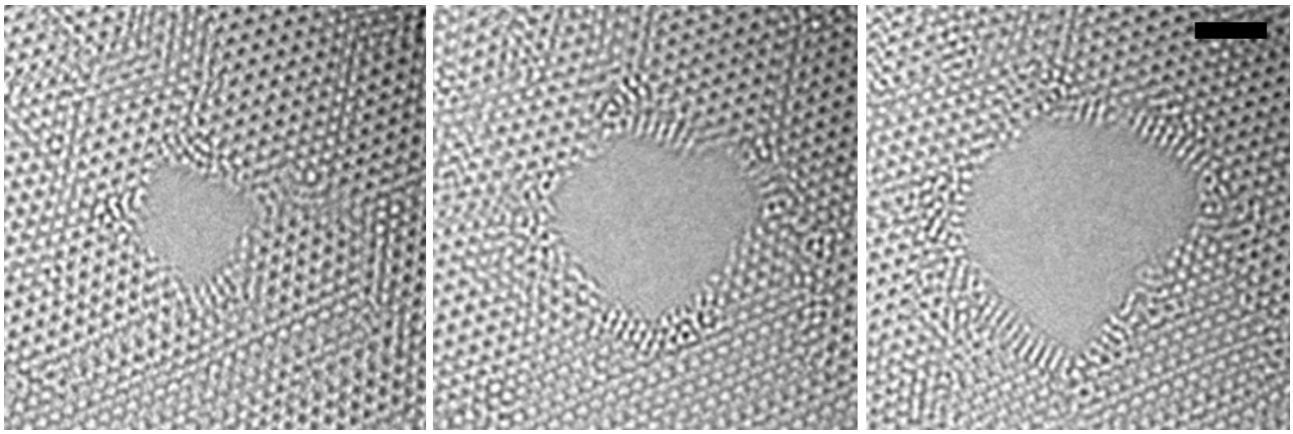

Figure 4.1 The sequential growth process of a void defect on molybdenum disulfide (MoS_2) by electron beam irradiation in monolayer MoS_2 sheet. Mo atoms aggregate at the edge. Scale bar=2 nm.

Thus, microstructural voids and various topological defects greatly influence the properties of MoS_2. Understanding these factors is crucial for designing and optimizing nanomaterials and, by extension, the performance of MoS_2-based devices. As MoS_2 is grown and processed, it is prone to developing different types of defects, including vacancies, inclusions, dislocations, grain boundaries, nanovoids, and nano-cracks. These defects can impact the anticipated performance of MoS_2-based nanodevices, affecting their preparation, handling, and overall functionality [163].

Moreover, the conditions in which MoS_2-based devices are employed can also lead to the formation of defects [208]. Functionalizing 2D MoS_2 sheets by introducing voids of specific sizes enables the tailoring of the material's mechanical properties. Recent research has focused on investigating the mechanical performance of monolayer MoS_2, delving into how defects, inclusions, strength, damage, debonding, and failure impact its properties [165,193]. Understanding these effects is crucial for optimizing and harnessing the potential of MoS_2 in various applications.

Although the above monolayer MoS_2 intriguing properties can feasibly be synthesized nowadays, they face different key challenges for industrial use, such as, the Synthesis and Scalability: to produce large, high-quality, single-layer samples, Bandgap Engineering: Tuning the bandgap to make it direct is important for improving its performance in electronic and optoelectronic devices. Integration: Integrating single-layer MoS_2 with other materials and existing semiconductor technologies is a challenge. Thermal Management: Developing effective thermal management strategies for single-layer MoS_2 devices, which can become hot during operation. Overcoming these challenges is pivotal in order to harness the full potential of 2D materials and to explore their novel properties for various

applications. Given the vast number of possible configurations for 2D materials, numerous unexplored configurations may have exciting applications. Traditional trial-and-error experimental approaches require substantial time, effort, and cost, particularly when pursued without clear guidelines or specific targets. Computational design and prediction processes can significantly expedite the exploration of new 2D configurations. They enable the prediction of new materials and properties, forecast novel 2D structures and their growth routes, and provide ideal research platforms for controlling studies on 2D nanostructures under varying environmental conditions.

The work focuses on addressing the identification problem to determine the parameters that define the void's shape concerning the material's properties. This approach holds potential for applications involving functional graded materials, nanomaterials, and the design of materials with prescribed properties. The concept involves crafting materials with predetermined characteristics through the introduction of voids. The method detailed in the chapter revolves around two main components: an optimized algorithm for solving problems and a solver for the direct problem.

Nanostructures are simulated using the molecular dynamics (MD) method, enabling the computation of monolayer MoS_2 with a spectrum of mechanical properties. These properties can be calculated via MD methodologies and involve a series of numerical tests, such as uniaxial tension, compression, and shear to assess the material's behavior [164,167,193,209].

The research involved the utilization of the well-established molecular dynamics (MD) code, LAMMPS, for resolving the direct problem. In recent times, inverse methods have gained significant traction for predicting structural and material properties. These methods facilitate the solution of parameter-related problems by employing optimization techniques and a series of solutions from direct problems.

Inverse methods have been extensively used in addressing mechanical and thermomechanical problems, particularly in the search for material properties and their corresponding structures [210]. These problems are often tackled by formulating inverse problems based on direct problem solutions computed through numerical methods like the finite element method (FEM), boundary element method (BEM), and molecular dynamics (MD). The objective function involved in optimization algorithms within inverse methods typically exhibits multimodal characteristics, prompting the utilization of global optimization techniques throughout the problem-solving process.

The utilization of evolutionary algorithms combined with boundary element method (BEM) computation in optimizing and identifying cracked structures and internal void defects subjected to thermomechanical and dynamical loading conditions are demonstrated in [210–212]. Sigmund [213] introduced the inverse homogenization method, leveraging it to adjust the elastic properties of

materials for various periodic truss, frame, and continuum structures. This method also aided in designing microstructures with prescribed elastic properties and negative Poisson's ratios. Additionally, an in-house implementation of evolutionary algorithms was applied to explore and identify new stable molecular graphene-like 2D materials [214,215].

In Chapter 3, The focus is on computing the mechanical properties, specifically the independent elastic properties, of monolayer MoS_2 with both single and multiple random defects. These computational results underscored the substantial impact of defects on the elastic material properties of MoS_2 nanosheets [193]. In this chapter, the objective is to determine the void size that corresponds to predefined elastic properties, which are user-defined. We have established the criteria for these prescribed elastic properties by assuming that the material contains a void, and these properties should be different from those of the material without a void. To achieve this, we have applied an evolutionary algorithm (EA) in conjunction with LAMMPS to find the size of the void that fulfills these prescribed elastic properties. This approach is a creative way to control and design materials with prescribed mechanical characteristics.

This study aims to investigate the impact of void defects on the mechanical stiffness of MoS_2. The computational expense involved in simulating disordered MoS_2 with a void and random defect distribution using molecular methods can be quite high. Instead, this study employs an alternative approach: examining the lattice and prescribed stiffness of disordered layered MoS_2 through the use of Evolutionary Algorithm optimization integrated with Molecular Dynamics [97]. This method offers the advantage of conducting extensive numerical calculations on large systems at a comparatively lower computational cost. As a result, the subsequent pages will detail a comprehensive set of results concerning the system's properties.

The upcoming sections are structured as follows: Section 4.2 will discuss about the Evolutionary Computation for 2D material design. In section 4.3 will discuss evolutionary optimization techniques and how the objective function is evaluated within this context. Additionally, this section will include the specifics of the molecular dynamics modeling of 2D MoS_2 with voids. It will outline the evolutionary identification of voids aimed at achieving prescribed properties by minimizing the objective function. Section 4.4 will delve into numerical identification examples showcasing the iterative capability of this method in solving the optimization problem. The ensuing pages will present a precise compilation of results for the system's properties. This organization will allow for a comprehensive exploration of the evolutionary optimization approach employed in achieving the specified material properties.

4.2. Empowering Nanostructure Design with Evolutionary Computation for 2D material design

Optimization plays an important role in the design and numerical modelling of existing macro and nanomechanical systems. By appropriately formulating the optimization problems, including the objective function, constraints, and design variables, it is possible to obtain new solutions with better tailored mechanical properties which are less energy-consuming, more durable, or lighter. A special case of the optimization problems associated with materials science is the design of new two-dimensional (2D) nanomaterials and nanostructures.

Optimization is a critical aspect in the design and analysis of macro and nanomechanical systems. By formulating the optimization problems effectively, one can target improved mechanical properties in terms of energy efficiency, durability, or weight reduction. Design of two-dimensional (2D) nanomaterials and nanostructures, optimization becomes particularly crucial. Important points regarding the optimization process for these materials:

- **Objective Function:** The objective function in the optimization problem is typically focused on specific mechanical properties tailored to the intended application. For 2D nanomaterials, properties such as strength, elasticity, conductivity, or other material-specific characteristics might be optimized.
- **Constraints:** Constraints can involve limitations on the design space, ensuring that the resulting structure or material meets certain criteria. This might include geometric constraints, material properties, or even manufacturing limitations.
- **Design Variables:** These variables encompass the parameters that can be modified within the design to achieve the desired objectives. For 2D nanomaterials, this could involve factors like layer thickness, chemical composition, interlayer interactions, or defect engineering.
- **Simulation and Modelling:** Numerical simulations and models, often involving computational tools like molecular dynamics simulations, density functional theory calculations, or finite element analysis, play a significant role in predicting the behavior and properties of these materials.
- **Trade-offs:** Optimization often involves trade-offs. For instance, increasing strength might reduce flexibility or vice versa. Balancing these trade-offs is a critical aspect of the optimization process.

- **Novel Material Design:** Optimization techniques can be used to propose and identify entirely new materials or structures that possess specific and desirable properties, which might not exist naturally.
- **Energy and Resource Efficiency:** Optimization in material design can also lead to more energy-efficient manufacturing processes or materials that are lighter and require fewer resources, contributing to sustainability efforts.

The integration of optimization techniques with advanced material science is leading to the creation of innovative and purpose-built materials. The exploration of 2D materials, particularly carbon-based graphene allotropes, has indeed been a thriving area of research over the past decade. These materials exhibit extraordinary properties, ranging from mechanical strength to thermal and electronic characteristics [216–220]. Some of the prominent carbon-based graphene allotropes include graphene itself and variations such as graphene oxide, graphene nanoribbons, and graphene quantum dots.

Besides graphene, several other monoatomic 2D materials have garnered attention due to their unique structures and properties. Some examples include:

- **Bismuthine:** This is a 2D material composed of bismuth atoms arranged in a honeycomb lattice similar to graphene. It holds potential due to its distinctive electronic properties.
- **Germanene, Silicene, and Stanene:** These are materials composed of Germanium, Silicon, and Tin atoms, respectively, arranged in a similar honeycomb lattice structure to graphene. Each possesses its own unique set of properties, making them potentially useful in various applications.
- **Boron Nitride:** Similar in structure to graphene but made of boron and nitrogen atoms, boron nitride offers properties such as excellent thermal and chemical stability, making it valuable in various industries, particularly in nanoelectronics and as a potential lubricant.
- **Single-Layered Molybdenum Disulfide (SLMoS_2):** Unlike graphene, SLMoS_2 consists of molybdenum and sulfur atoms. It exhibits semiconductor properties and has applications in electronics and optoelectronics.

Some of these studies, such as the work done by Mrozek and collaborators in 2019 and Kuś et al. in 2022 [221,222], specifically focus on the properties, synthesis methods, or potential applications of materials like boron nitride and single-layered molybdenum disulfide.

Researchers have been actively exploring various computational methods to unravel the mysteries of nanostructures, particularly in terms of identifying their stable configurations. These efforts have

yielded valuable insights into the behavior and properties of nanomaterials at the atomic level. Among the employed techniques are non-classical optimization algorithms and atomic-level simulations.

The authors of this study have made significant contributions to this field by developing bio-inspired optimization algorithms, such as the Artificial Immune System (AIS) and Particle Swarm Optimization (PSO). These algorithms have been effectively integrated with Molecular Statics (MS) and Molecular Dynamics (MD) solvers, enabling the exploration of various nanostructures, including small aluminum clusters, novel graphene allotropes, and other carbon-based 2D materials with tailored mechanical properties [214,223,224].

This particular work marks a continuation of the authors' research endeavors, focusing on further refining their optimization methods and expanding their application to a broader range of 2D materials. The aim is to identify stable configurations in diverse nanostructures beyond graphene, potentially involving different chemical elements or compounds.

This research holds immense potential for advancing our understanding of nanostructures and paving the way for the development of novel materials with enhanced properties and applications. By elucidating the stable configurations of these materials, researchers can gain valuable insights into their behavior and interactions, enabling the design of nanomaterials with tailored properties for various applications, such as electronics, catalysis, and energy storage.

4.3 Defining the Problem Space: A Comprehensive Approach to Problem Formulation

The optimization problem focuses on the automated design of MoS_2 structures with specific, prescribed material properties. While we consider mechanical stiffness as a primary concern, it's essential to note that this optimization problem is versatile and can be adapted to target various other material properties such as thermal, optical, or any other property related to the microstructure. The objective function in this optimization problem is based on a comparison between the desired or prescribed material properties and the actual properties computed for each designed microstructure. The design vector **ch** encompasses parameters that define the size, shape, topology, and any other relevant characteristics of the microstructure. For instance, in this context, the MoS_2 structure is modified by introducing voids, and the properties of these voids are represented and controlled using the design variables. The general formulation of the optimization problem can be stated as follows:

Objective Function: The objective function ‘f(**ch**)’ depends on the prescribed material properties and the actual properties computed for each design of the microstructure. Where f(**ch**) represents the

difference between the prescribed material properties and the computed properties based on the design parameters represented by **ch**.

Constraints: There might be additional constraints depending on the specific requirements of the problem. For example, constraints could limit the volume fraction or distribution of voids, or they could impose restrictions on the range of design variables within the feasible space.

Design Variables: The design vector 'g_i' represents the variables that define the microstructure, such as dimensions, shape, void distribution, or any other parameters that impact the material properties. These variables can be adjusted to find the optimal design that aligns with the desired material properties.

The process involves iteratively adjusting the design variables 'g_i' to minimize the difference between the prescribed and computed material properties. Optimization algorithms, such as the Evolutionary Algorithm described earlier, are used to search through the solution space and determine the optimal set of design variables that yield the desired material properties.

By formulating the optimization problem in this manner, it becomes possible to systematically design and engineer microstructures with specific material properties, facilitating the creation of tailored materials for diverse applications.

$$\begin{cases} find & \mathbf{ch} = (g_1, g_2, \dots \dots g_N) \\ minimize & f(ch) = \left\| \mathbf{P} - \mathbf{P}_{ref} \right\| \\ s.t & g_{iL} \leq g_i \leq g_{iU} \end{cases} \tag{4.1}$$

The equations presented indicate a mathematical representation of the optimization problem. The variables g_{iL} and g_{iU} represent the lower and upper constraints respectively for the design variables (defining aspects such as size, shape, and distribution of voids within the nanostructure). The element **P** represents the properties of the nanostructure obtained from a given design vector **ch**, while $\mathbf{P}_{ref}$ represents the desired reference or prescribed properties of the nanostructure. The goal of the optimization is to minimize the difference between the current (obtained) and the reference (prescribed) material properties. This difference is formulated as a function of the design variables **ch**. The objective function aims to reduce this difference to zero, indicating an exact match between the reference and obtained properties. However, achieving an exact match may not always be feasible or practical due to various constraints or complexities. Hence, a small difference between the reference and obtained properties might also be acceptable, depending on the specific problem context.

The focus of the work is on optimizing the nanostructure, particularly considering mechanical properties, which in this case, are represented by the variables **P** and $\mathbf{P}_{ref}$. These properties are dependent on the stiffness of the nanostructure, including the introduced voids. The optimization process involves iteratively adjusting the design variables (g_i) to minimize the difference between the computed (**P**) and the desired ($\mathbf{P}_{ref}$) material properties, particularly focusing on the mechanical properties related to the stiffness of the nanostructure with incorporated voids. The objective function, therefore, represents the discrepancy between the actual and desired properties, and the optimization process aims to find the optimal combination of design variables that bring the properties of the nanostructure as close as possible to the prescribed reference properties, especially focusing on mechanical stiffness affected by the introduced voids. The stress–strain relationship for small strains can be expressed with Voight notation as follows:

$$\sigma_{ij} = \mathbf{P}_{ij}\varepsilon_{ij} \tag{4.2}$$

where ε_{ij} denotes the strain components, and $\mathbf{P}_{ij}$ denotes the elastic constants to be used during objective function evaluation. The shape of the nanostructure is modified according to **ch** by introducing an elliptic void, as shown in Figure 4.2.

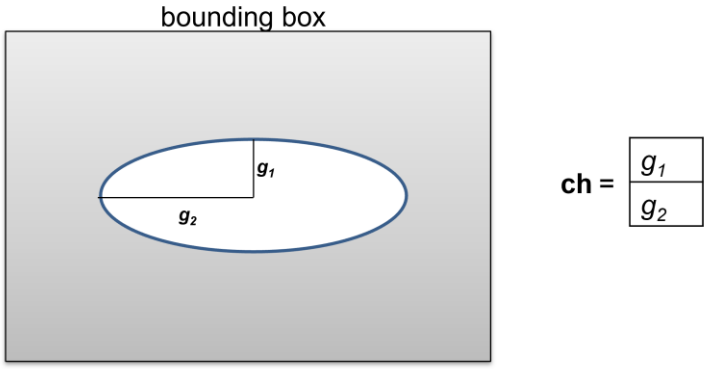

Figure 4.2 The nanostructure with an elliptical void described by two design variables.

A 2D infinite nanostructure was modeled using periodic boundary conditions. This means that the structure was designed in a way that its boundaries behave as if they are connected to each other, allowing for an infinite replication of the structure. The use of periodic boundary conditions is common in simulations to replicate an infinite system, allowing for more efficient calculations by eliminating the need to model an extensive structure entirely. The maximum size of the void within this nanostructure was limited by the size of the unit cell utilized in the simulations. The unit cell is the fundamental repeating unit used to create the periodic structure and its size defines the boundaries

within which the simulation is conducted. The voids within the nanostructure are limited in size based on the dimensions of this unit cell.

The mechanical properties, specifically the stiffness in two directions, were computed using a Molecular Dynamics (MD) approach. The outcome of these simulations provides information on the nanostructure's mechanical behavior, allowing for the assessment of stiffness in the specified directions. These computed mechanical properties are likely part of the data used to evaluate the fitness function in the optimization process aimed at tailoring the material's properties. The algorithm for determining the stiffness of the nanostructure is shown in Figure 4.3.

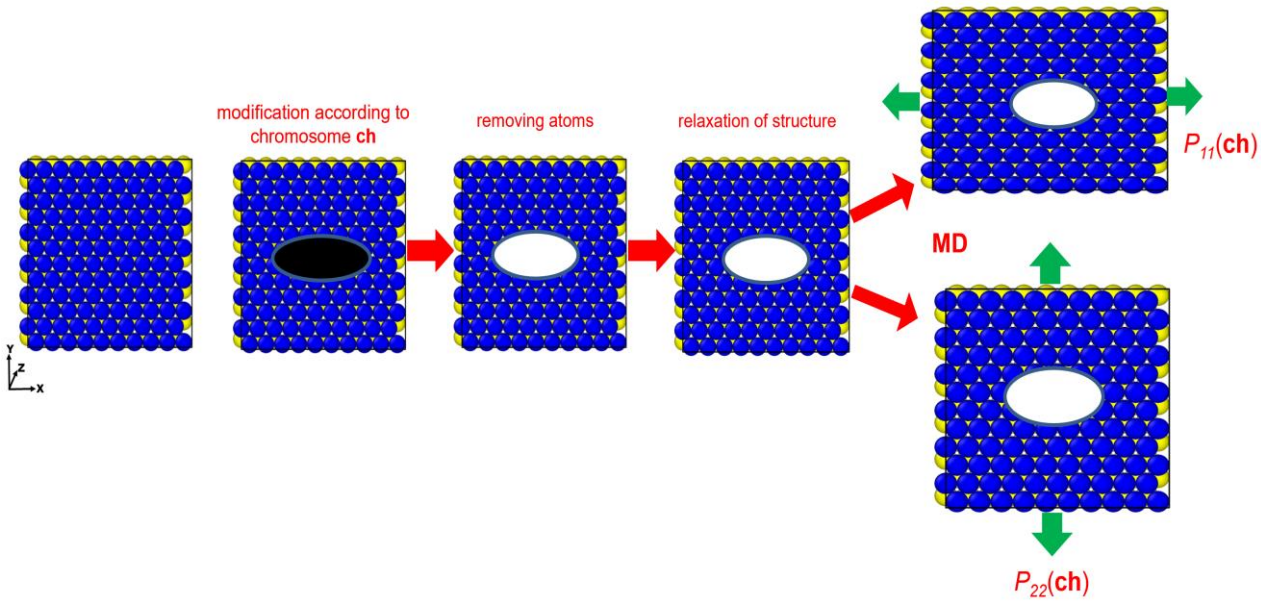

Figure 4.3 Determination of nanostructure stiffness in two directions. An ellipse is introduced into the pristine nanostructure by removing atoms in black area. Next, the structure is relaxed, and two analyses of microstructure stretching are performed in two different directions. Then, the stiffness is computed on the basis of the MD results.

In the study, the process of modifying the 2D nanostructure involved introducing voids into the pristine nanostructure. Subsequently, a relaxation step was carried out to stabilize the structure after the void introduction. This relaxation process aims to allow the structure to equilibrate and minimize any structural instabilities resulting from the void creation. Following the relaxation step, the nanostructure underwent uniaxial tensile load testing. stress–strain curves were obtained in two different directions, providing insights into how the material responds to tensile loads along those specific axes. It's highlighted that while the focus in this work is on stiffness computation in two specific directions for a monolayer of MoS_2, other types of loads could be applied to investigate additional material properties. For instance, shear stresses, as well as thermal and optical properties

of the nanostructure, could be explored by applying different types of loads or subjecting the material to various environmental conditions or simulations. The atomic model used in this study consisted of approximately 10,000 atoms within the nanosheet, covering a domain size of about 175 square angstroms ($Å^2$). This information provides a sense of the scale and complexity of the atomic model used in the simulations, reflecting the detailed nature of the computational analysis performed in the study.

The Stillinger–Weber (SW) [93,94] potential was utilized to represent the atomic interactions within the MoS_2 nanostructure. Before subjecting the MoS_2 structure to tensile deformation, the model was relaxed at a specified temperature of 300 Kelvin (K) and at 0 bar pressure. This relaxation process was conducted through an isothermal–isobaric ensemble (NPT) for a duration of 30 picoseconds (ps). The NPT ensemble maintains a constant temperature and pressure throughout the simulation, allowing the structure to equilibrate under these conditions. Subsequently, the uniaxial tensile deformation was carried out at a constant temperature of 300 K. The Nose–Hoover thermostat was used to regulate and maintain the temperature of the simulation system. This thermostat helps control the temperature of the system by adjusting the kinetic energy of the simulated particles.

The positions and velocities of all atoms were updated using the Verlet integration algorithm. The simulations were performed using the LAMMPS software package. Additionally, the Open Visualization Tool (OVITO) was utilized for visualization and analysis of the output data from the simulations [190]. The uniaxial tensile deformation was carried out at a constant strain rate of 0.0001 $picoseconds^{-1}$ to estimate the stiffness of the MoS_2 nanostructure. This type of deformation involves applying a force to stretch the material along a single axis, allowing the calculation of stress–strain relationships to determine the mechanical properties, specifically stiffness, in the direction of the applied force.

Various methodologies are available to calculate stress within the simulated systems. Among these methods, the virial theorem, a concept rooted in the works of Clausius and Maxwell, is well-known. There are also more modern approaches to stress calculation, including methodologies developed by researchers such as Hardy, Lutsko, and Tsai [225–227]. While the modern approaches are considered more advanced and potentially more accurate than the virial theorem, studies have shown that excellent agreement between the Hardy approach and the virial stress approach can be achieved with adequate spatial or temporal averaging [228,229]. This means that, under specific conditions where averaging is sufficiently applied, these methods can converge and produce comparable results.

However, due to the availability and straightforward implementation in many molecular dynamics' codes, including LAMMPS, the virial stress approach is commonly utilized in this study. LAMMPS provides readily available implementations for stress calculations in molecular dynamics simulations. Specifically, in the molecular dynamics calculations performed using LAMMPS, the stress tensor components were computed following particular methodologies, as detailed in references [230]. These stress calculations provide essential information about the distribution and behavior of stress within the simulated system, which is critical for understanding the mechanical properties of the material and its response to external forces.

$$\sigma_{ab} = \frac{1}{\mathrm{V}}\left[\frac{1}{2}\sum_{i}^{N^*}\sum_{j(\neq 1)}^{N} f_{ij}^{a}\, r_{ij}^{b} + m_i u_i^a u_i^b\right], \tag{4.3}$$

where a and b denote the Cartesian components, f_{ij} is the force acting on atom i due to another atom j, V is volume, m_i *mass* and u_i velocity of atom i, and N is the number of atoms. Figure 4.4 shows examples of two simulation results with a stiffness of 163 GPa and 158 GPa.

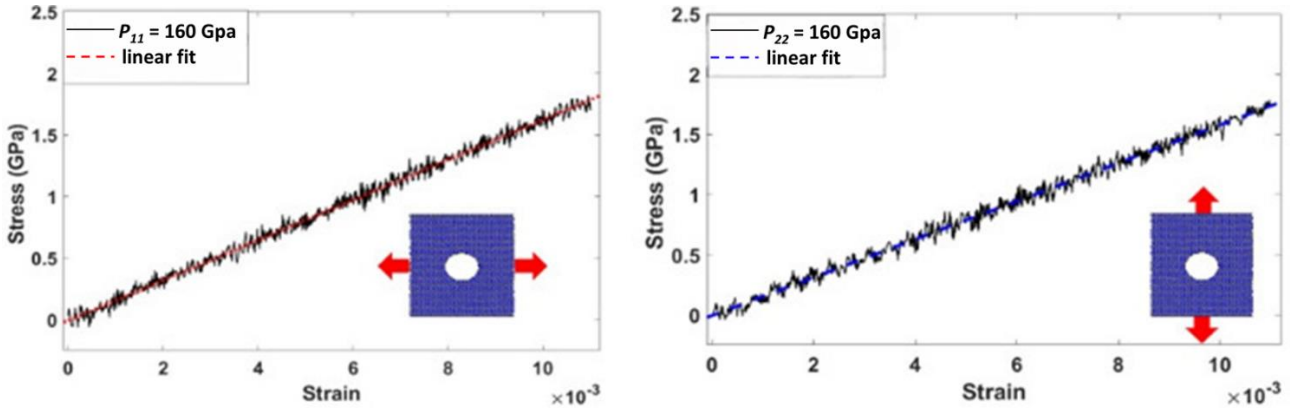

Figure 4.4 Examples of stress-strain relationship during uniaxial tension in two directions.

The objective function value could be computed for such a case as the sum of the absolute difference between computed stiffness and prescribed material properties.

Figure 4.5 shows the deformation evolution of MoS_2 samples at maximum strain values for a stiffness of 163 Gpa and 158 Gpa, and the atoms are painted according to the local elastic atomic strain. The distribution of atomic strain is compared at a strain where MoS_2 sample are in the linear elastic phase according to the stress curve in Figure 4.4.

Normalized strain distribution near the central void with the radii of of $g_1 = 28.12$ Å and $g_2 = 23.15$ Å under the nominal tension stress of 160 GPa are shown in Figure 4.5. From the distribution results of the normal strain ε_{xx} (Figure 4.5 a-d) and ε_{yy} (Figure 4.5 e-h), it is found that the normal strain concentration is different with homogeneous materials. As we all know, based on the homogeneous material assumption, the stress (strain) concentration location is at ±90° void tips. The first image (Figure 4.5b), corresponding to strain ε_{xx} =0.01, presents the appearance of the first plastic strains, which occur on the opposite sides of the void in the area of the thinnest cross-section of the sample. The geometrical discontinuities in an elastic solid are known to re-distribute the strains applied on its boundary, thus leading to unexpected regions of compressive strains inside the solid. The further increase of the external load results in the growth of strains in the area surrounding the void. The propagation of the plastic deformations to the outer edge of the sample (in the horizontal direction, it is accompanied by the first two inclined paths of plastic strains (Figure 4.5 c and d)). The distribution of strain field presented in Figure 4.5c corresponds to ε_{xx} =0.025. In this case, the presence of the map of deformations shows the characteristic symmetric pattern, which is repeated with higher absolute values for higher loads (see Figure 4.5 d). It is also interesting to note that, by comparing the strain calculated from the stress methods, the atoms bearing the largest stress is not the ones with largest distortion, which may be attributed to the discrete and incomplete nature of lattice at the void edges.

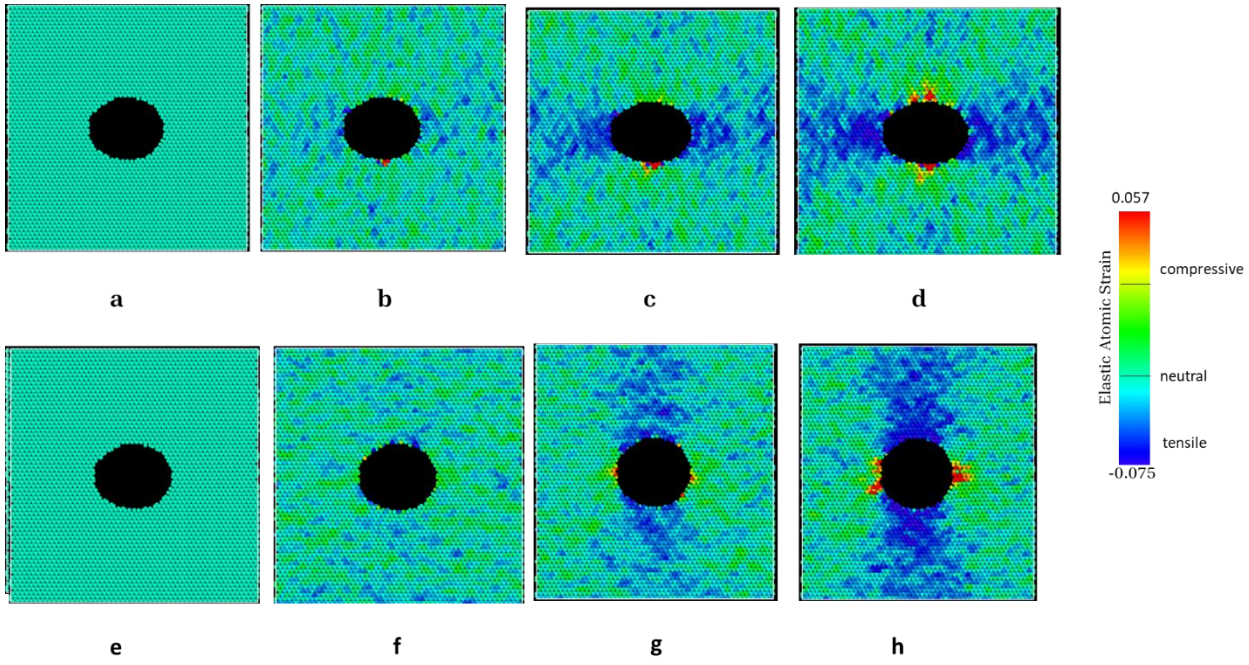

Figure 4.5 Elastic stress concentration around a hole in a MoS_2 subjected to uniform tensile forces on the horizontal sides (a-d) and vertical sides (e-h) and traction-free on the other two boundaries respectively. 'Red' identifies regions of compressive (negative) azimuthal stresses, 'dark blue' is used for large tensile (positive) stresses, and the areas shown in 'pale blue' are only modestly affected by the presence of the hole.

The process of optimizing the nanostructure by introducing voids to achieve specific, prescribed mechanical properties. This optimization process is demonstrated across various cases involving different sets of prescribed material properties. The EA utilized in this study comprises two sub-populations, each containing a total of 32 individuals. These individuals represent different potential designs or solutions for the nanostructure. The EA employs specific methods for selection, mutation, and crossover:

Tournament Selection: This involves selecting individuals based on a tournament size of 5.

Uniform Selection: Employed with a probability of 0.3, offering uniform selection across the population.

Gaussian Mutation: Utilized with a probability of 0.5, where random mutations are introduced following a Gaussian distribution.

Simple Crossover: Used with a probability of 0.1, involving a basic exchange of genetic information between selected individuals.

Arithmetic Crossover: Also applied with a probability of 0.1, facilitating a crossover process that operates on numerical values to produce new solutions.

These parameters were chosen based on the prior experience gained during the resolution of structural optimization problems, referencing earlier studies by Kokot, Orantek, and Mrozek [215,224,231], which provided insights into the effective configuration of EA parameters for similar optimization problems. The number of iterations for the EA was set at 50, implying that the EA underwent 50 cycles or generations to search and optimize the design space for the nanostructure, aiming to achieve the desired mechanical properties within the prescribed constraints. This iterative process allows the algorithm to refine the solutions and progressively approach the optimal design for the given mechanical properties.

An optimized nanostructure with an approximate size of 170 Å × 170 Å was employed. This nanostructure was designed to contain an elliptical void, allowing for a specified range in void size. The void's dimensions could vary from 1 × 1 up to 50 × 50 Å, representing the radius of the elliptical void. The optimization process targeted the adjustment of this nanostructure, including the manipulation of the elliptical void within it, to achieve the prescribed material characteristics. The termination or stop condition for the optimization process was formulated as reaching the maximum number of iterations. Once the EA completed the specified number of iterations, the optimization

process concluded. This condition set a limit on the number of cycles the EA could undergo to search and refine the nanostructure design space within the given constraints and objectives.

The evaluation of the fitness function for each individual within the EA was conducted in line with the method described in chapter 2. Section 2.7. This evaluation required solving two problems using the LAMMPS software to determine the stiffness in two different directions. The fitness function was computed based on the results obtained from these simulations. To expedite the computation of fitness functions in each iteration, a parallel computing approach was implemented. This parallel method achieved high efficiency by distributing the workload across multiple processing units. Specifically, when the number of processing units equaled the number of molecular dynamics (MD) problems (which was 64 in this case, accounting for the number of individuals multiplied by the number of mechanical properties), computations were performed in a highly parallel manner.

Moreover, additional processing units were employed to parallelize each MD simulation further. This approach allowed for efficient utilization of computational resources and faster computation of fitness functions, particularly in scenarios involving a considerable number of individuals and properties. The computational tasks were executed using supercomputers such as Okeanos and Karolina, where several hundred to even thousands of processor cores were utilized simultaneously during the computations. These high-performance computing systems were instrumental in facilitating the extensive computational demands of the simulations, enabling efficient parallel processing and significantly reducing the overall computational time.

The changes in the best objective function over few iterations for adequate nanostructures with prescribed material properties $P_{ref11} = P_{ref22} = 160$ GPa are shown in Figure 4.6.

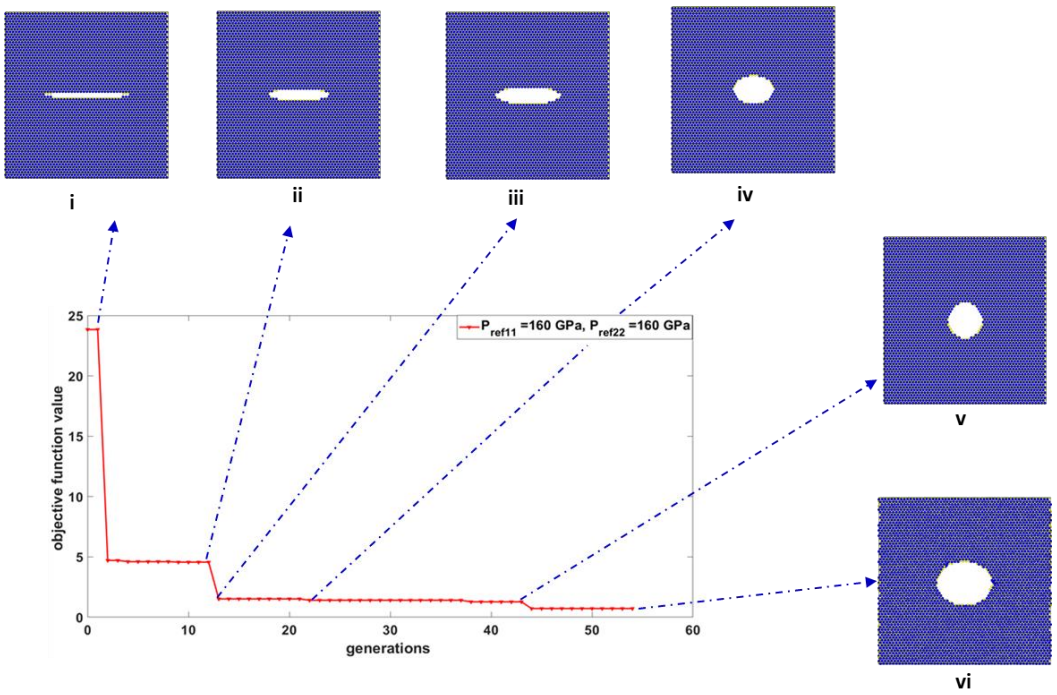

Figure 4.6 Progress of the convergence of the objective function indicating the evolution of the void during iterative generations for prescribed elastic properties Pref11 = 160 GPa, Pref22 = 160 GPa. The corresponding void dimensions obtained during generations were (i) g_1 = 46.06 Å and g_2 = 2.95 Å, (ii)g_1 = 32.18 Å and g_2 = 6.07 Å, (iii) g_1 = 33.92 Å and g_2 = 8.86 Å, (iv) g_1 = 21.36 Å and g_2 = 14.88 Å, (v) g_1 = 18.41 Å and g_2 = 19.38 Å, and (vi) g_1 = 28.12 Å and g_2 = 23.15 Å.

Three separate void identification analyses were conducted for the MoS_2 nanosheet, each associated with distinct prescribed material properties. These analyses involved inducing an elliptical void at the center of the sheet. Table 4.1 in the paper presents the values of the best solutions obtained from these numerical tests. Specifically, it showcases the calculated material properties (referred to as P_{11} and P_{22}) corresponding to the ellipse radius denoted as g_1 and g_2, respectively, for each of the prescribed material properties.

However, it's noted in the results that the obtained material properties (P_{11} , P_{22}) for the given ellipse radii (g_1, g_2) were not entirely identical to the prescribed material properties ($\mathbf{P}_{ref}$). This deviation or difference between the obtained and prescribed material properties is quantified and represented by the errors eP_{11} and eP_{22}. The mentioned errors eP_{11} and eP_{22} signify the discrepancy or difference between the obtained and prescribed material properties. Despite not being identical, the obtained material properties were observed to be very close to the prescribed ones. This signifies that the optimization process managed to achieve material properties that closely aligned with the specified prescribed values, though they weren't exact matches. The errors, eP_{11} and eP_{22}, likely reflect the degree of deviation or inaccuracy between the obtained and prescribed material properties.

Table 4.1. The prescribed and resulting stiffness, ellipse radius, and error of obtained stiffness.

Case	P_{ref11} **(GPa)**	P_{11} **(GPa)**	P_{ref22} **(GPa)**	P_{22} **(GPa)**	g_1 **(Å)**	g_2 **(Å)**	eP_{11} **(%)**	eP_{22} **(%)**
1	150.0	149.2	180.0	179.5	36.35	12.19	0.5	0.3
2	160.0	162.6	160.0	158.0	28.12	23.15	1.6	1.3
3	180.0	179.5	150.0	148.0	15.35	33.44	0.3	1.3

Figure 4.7, 4.8 and 4.9 displays the resulting structures corresponding to the three different cases examined in the analysis. Each case had specific goals related to the size and orientation of the elliptical void within the MoS_2 nanostructure, guided by the prescribed material properties. The expectations for the three cases were as follows:

- **First Case**: The nanostructure was anticipated to have an ellipse with a larger radius in the y-direction, relative to the x-direction.

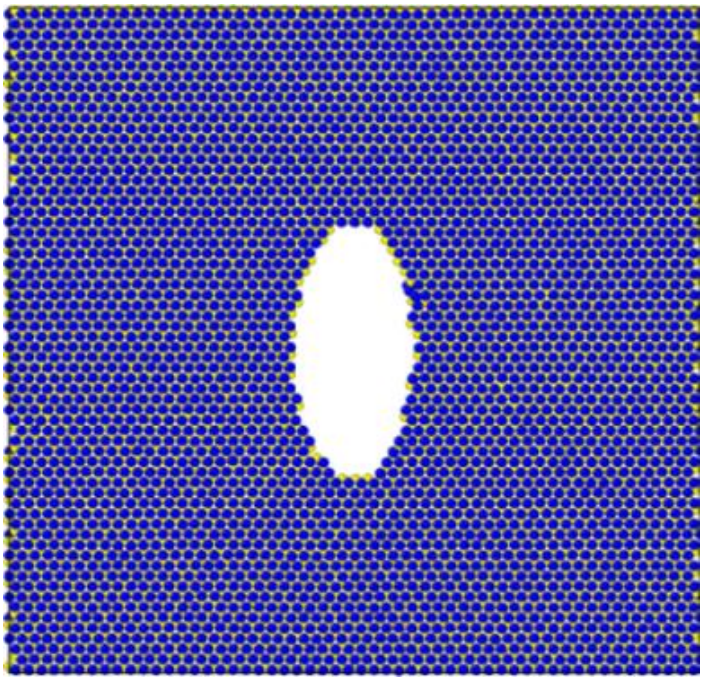

Figure 4.7 Monolayer MoS_2 nanosheet with void identified by optimization: (a) Pref11 = 180, Pref22 = 150 GPa (g1 = 15.35 Å and g2 = 33.44 Å)

- **Second Case**: The radii of the ellipse in the x and y directions were expected to be similar, as per the prescribed material properties.

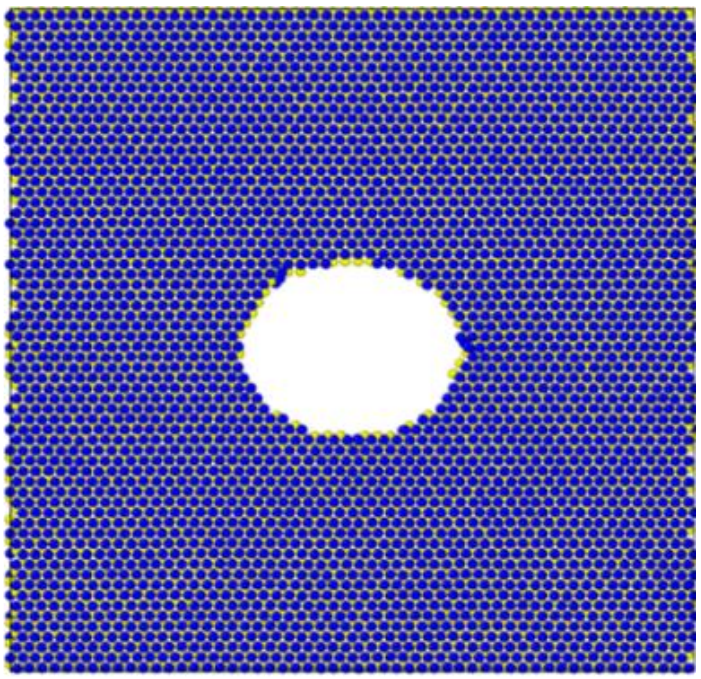

Figure 4.8 Monolayer MoS_2 nanosheet with void identified by optimization: (b) P_{ref11} = 160, P_{ref22} = 160 GPa (g_1 = 28.12 Å and g_2 = 23.15 Å)

- **Third Case**: The prescribed material properties aligned with the first case, implying that the ellipse's radii should be similar to the first case.

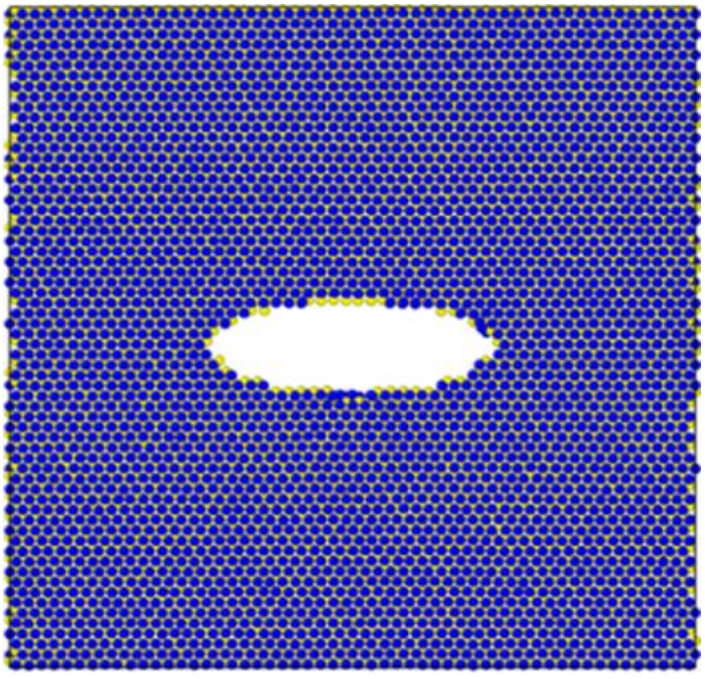

Figure 4.9 Monolayer MoS_2 nanosheet with void identified by optimization: (c) P_{ref11} = 150, P_{ref22} = 180 GPa (g_1 = 36.35 Å and g_2 = 12.19 Å)

Importantly, the MoS_2 nanostructure wasn't symmetrical in the x (g_1) and y (g_2) directions, implying that the second case would not necessarily yield the same ellipse radii in both x and y directions. This lack of symmetry in the material structure was considered in the analysis. The results obtained were

in accordance with these expected goals and intuitive reasoning, generating exact values for the size and orientation of the void within the nanostructure. This successful alignment between the prescribed and achieved results indicated the effectiveness of the optimization method in tailoring the structure to meet specific material property requirements. It's highlighted that while the method demonstrated success with the prescribed stiffness values, there are limitations related to the maximum stiffness of the MoS_2 sheet and the size constraints of the void, affecting the scope and applicability of the method.

4.5 Summary

In this chapter, we introduce evolutionary computation and analyze the similarities and differences with conventional search algorithms. The reasons for using EC in solving optimization problems and the situations where EC could be beneficial are briefly discussed. A brief review on different EAs and their components is provided. The use of EAs by solving a case problem has been demonstrated.

The emergence of defects in materials like MoS_2 can lead to a reduction in their mechanical properties, such as fracture strength and Young's modulus. However, these defects can have potential applications in creating innovative materials or nanosystems, such as graded materials. Leveraging defects, such as voids, in MoS_2 for specific purposes is an area of interest.

In this study, an optimization method was employed to tailor the material properties of a periodic monolayer MoS_2 containing a void as a defect. The goal was to optimize the material to meet prescribed mechanical properties while integrating the presence of the void as part of the design.

The problem was formulated as an optimization challenge seeking to identify the simplest possible nanostructure that adhered to constraints established by prescribed elastic constants. Through numerical examples, the study demonstrated that the proposed optimization method successfully determined the void size required to achieve the desired mechanical properties.

The research showcases the potential of molecular simulations for 2D nanostructures. It emphasizes the efficiency of using molecular simulations to design nanostructures with specific, prescribed properties. Moreover, it indicates that the method is adaptable and could be extended to incorporate considerations for thermal or optical properties of the nanostructure by adjusting the components of the objective function and employing suitable simulation techniques to address these additional properties.

Chapter 5

Conclusions and future work

The mechanical properties of 2D MoS_2 nanostructures, including their exceptional strength and stiffness, are meticulously explored in this PhD Thesis. The comprehensive investigation, encompassing a wide range of experimental and theoretical techniques, has yielded profound insights into the underlying mechanisms that govern their mechanical behavior. The unique structural and compositional features of 2D MoS_2 nanostructures enable them to withstand significant external forces and deformations without compromising their integrity. This remarkable resilience stems from the delicate interplay of these structural and compositional aspects.

The research demonstrates that 2D MoS_2 nanostructures exhibit remarkable tailorability. By manipulating various structural and compositional parameters, we can optimize their mechanical properties to suit specific application requirements. These findings have significant implications for the development of next generation nanodevices based on 2D MoS_2 nanostructures. By understanding and manipulating their mechanical properties, we can harness their exceptional strengths to create highly resilient, durable, and functional nanodevices that revolutionize various technological domains.

My initial research endeavor involved conducting systematic molecular statics simulations to investigate the mechanical properties of monolayer MoS_2 nanosheets. The innovative approach employed molecular statics calculations to analyze the elastic constants of pristine and defective MoS_2. The elastic constants of infinite sheets were found to be isotropic, indicating their uniform orientation and behavior. The calculated elastic constants satisfied the Born mechanical stability criterion, ensuring the structural integrity of the material under mechanical stress. Specifically, the computed elastic constants adhered to the following inequalities: $C_{11} > 0$, $C_{11} > C_{12}$, and $C_{66} > 0$. These inequalities signify that MoS_2 exhibits positive stiffness constants along all three principal axes, ensuring resistance to deformation and maintaining its integrity. Furthermore, our investigations revealed a significant decrease in elastic moduli and associated properties with increasing defect concentrations. This decline in mechanical properties primarily stems from the disruption of the regular atomic structure caused by the presence of defects. Notably, antisite defects, which involve the substitution of atoms within the atomic lattice, were found to have a particularly detrimental effect on the mechanical properties of MoS_2.

The systematic exploration of the geometric structures of antisites and vacancies in monolayer MoS_2 through molecular statics calculations has significantly advanced our understanding of the variation in mechanical properties induced by these point defects. I have demonstrated that the introduction of point defects, particularly antisites, can significantly alter the mechanical behavior of MoS_2. These findings provide valuable insights for optimizing the mechanical properties of MoS_2 for various applications. Overall, the research has considerably improved the understanding of point defects in atomically thin transition metal dichalcogenides. These insights should benefit their potential applications in designing optoelectronic and nanoelectronic devices by enabling the tailoring of their mechanical properties to suit specific requirements.

My second research endeavor aimed to design MoS_2 nanostructures with prescribed mechanical properties, inspired by the study of their mechanical stiffnesses. To achieve this goal, I employed a hybrid optimization algorithm, which employs a combination of evolutionary algorithm (EA) and molecular dynamics (MD) simulations. The EA optimization program allows users to define the design domain, including the nanovoid, and specify possible boundary conditions. Upon execution, the program iteratively optimizes the structure until the desired mechanical properties are met. If no further optimization is possible due to the absence of removable atoms, the program terminates, indicating a structural failure. It still outputs the most optimized configuration obtained before the termination.

The main objective of this work was to introduce and evaluate the hybrid optimization algorithm for the design of 2D MoS_2 nanostructures with prescribed mechanical properties. The proposed algorithm combines the strengths of EAs and MD simulations, leveraging the efficient search capabilities of EAs for exploration of the design space while employing MD simulations for accurate evaluation of mechanical properties. The EA component utilizes mutation and crossover operators to effectively explore and exploit the design space. The crossover operator ensures diversity among the candidate structures, preventing the algorithm from prematurely converging to suboptimal solutions. The high search efficiency of the EA enhances the practical applicability of the algorithm in inverse problem-solving scenarios in nanoscience. Additionally, the algorithm's modular design allows for its integration with various molecular modeling software packages.

Numerical simulations demonstrated the efficacy of the proposed method in identifying stable configurations with nanovoids in MoS_2 nanostructures that exhibit the prescribed mechanical properties. These results were further validated through MD simulations of tensile tests, confirming the accuracy of the optimized structures. The algorithm's versatility extends to the optimization of three-dimensional molecular structures, as it can be applied with various minimization methods and

atomic potentials. The obtained results, the broad range of potential applications, and the adaptability of the algorithm make it a promising tool for general molecular optimization, not limited to 2D structures.

Overall, the hybrid optimization algorithm developed in this work provides a powerful and versatile tool for designing MoS_2 nanostructures with tailored mechanical properties. Its combination of EA and MD simulations enables efficient exploration of the design space, ensuring the identification of structures with the desired mechanical characteristics. The algorithm's modularity and adaptability to various computational setups further enhance its practical utility. The obtained results pave the way for the development of novel MoS_2-based nanodevices with enhanced mechanical properties, tailored to specific applications in various fields.

As an outlook for future studies, a few topics of interest are summarized as follows:

- Addressing thermal effects and rippling: Current first-principles and molecular calculations have provided valuable insights into the elastic properties of 2D materials. However, recent experimental findings suggest that temperature and rippling can significantly impact the in-plane and bending stiffnesses of these materials. Further experimental studies are necessary to fully understand these effects. In parallel, theoretical advancements involving statistical mechanics approaches and MD simulations are needed to predict the elastic behavior of 2D materials at finite temperatures.
- Defect engineering for enhanced strength and toughness: The presence of various defects can significantly alter the mechanical properties of 2D materials. Defect engineering techniques offer the potential to tailor the strength and toughness of these materials. However, fundamental questions regarding fracture mechanics of 2D materials remain unanswered from both continuum and atomistic perspectives. Addressing these questions is crucial for unlocking the full potential of defective engineering.
- Exploring novel applications exploiting superior mechanical properties: The development of novel applications that leverage the superior mechanical properties of 2D materials is an exciting area of research. Structural designs inspired by origami and kirigami, which involve folding and cutting patterns, hold promise for unprecedented applications in flexible and biomedical devices.

These research directions will undoubtedly lead to significant advancements in our understanding and manipulation of the mechanical properties of 2D materials, paving the way for the development of next generation nanodevices with enhanced performance and applications in various field.

Bibliography

[1] B. Marinho, M. Ghislandi, E. Tkalya, C.E. Koning, and G.-W. bertus de, Electrical conductivity of compacts of graphene, multi-wall carbon nanotubes, carbon black, and graphite powder., Powder Technol. 221 (n.d.) 351–358.

[2] K.S. Novoselov, A.K. Geim, S.V. Morozov, D. Jiang, Y. Zhang, S.V. Dubonos, I.V. Grigorieva, and A.A. Firsov, Electric field effect in atomically thin carbon films. , Sci. 306 (2004) 666.

[3] V.Y.U. Aristov, Grzegorz Kummer, Kurt Vyalikh, Denis V., O. Molodtsova, V. Preobrajenski, A.B. Zakharov, A.A. Hess, Christian Hanke, T. Buchner, Bernd Vobornik, Ivana., J. Fujii, G. Panaccione, Y.A. Ossipyan, and M. Knupfer, Graphene Synthesis on Cubic SiC/Si Wafers. Perspectives for Mass Production of Graphene-Based Electronic Devices., NANO Lett. 10 (2010) 992–95.

[4] X. Li, L. Tao, Z. Chen, H. Fang, X. Li, X. Wang, J.-B. Xu, and H. Zhu, Graphene and related two-dimensional materials: Structure-property relationships for electronics and optoelectronics., Appl. Phys. Rev. 4 (2017) 021306.

[5] C.-H. Lee, G.-H. Lee, A.M. van der Zande, W. Chen, Y. Li, M. Han, X. Cui, G. Arefe, C. Nuckolls, T.F. Heinz, J. Guo, J. Hone, and P. Kim, Atomically thin p-n junctions with van der Waals heterointerfaces., Nat. Nanotechnol. 9 (2014) 676–681.

[6] Y. Liu, D. Yu, C. Zeng, Z. Miao, and L. Dai, Biocom- patible Graphene Oxide-Based Glucose Biosensors., Langmuir. 26 (2010) 6158–60.

[7] S. Siddique, M.Z. Iqbal, and H. Mukhtar, Cholesterol immo- bilization on chemical vapor deposition grown graphene nanosheets for biosensors and bioFETs with enhanced electrical performance. Sensors and Actuators B:, Chemical. 253 (2017) 559–65.

[8] K.S. Novoselov, V.I. Fal′ko, L. Colombo, P.R. Gellert, M.G. Schwab, and K. Kim, A roadmap for graphene., Nature. 490 (2012) 192–200.

[9] K.I. Bolotin, K.J. Sikes, Z. Jiang, M. Klima, G. Fudenberg, J. Hone, Kim P., Stormer. and H. L., Ultrahigh electron mobility in suspended graphene., Solid State Commun. 146 (2008) 351–355.

[10] S.H. Kim, J.H. Lee, J.-S. Park, M.-S. Hwang, H.-G. Park, K.J. Choi, and W.I. Park, Performance optimization in gate-tunable schottky junction solar cells with a light transparent and electric-field permeable graphene mesh on n-si., J. Mater. Chem. C. 5 (2017)

3183–87.

[11] C.-C. Chen, C.-C. Chang, Z. Li, A.F.J. Levi, B. Stephen, Gate tunable graphene-silicon Ohmic/Schottky contacts., Appl. Phys. Lett. 101 (2012) 223113.

[12] L. Britnell, R. V. Gorbachev, R. Jalil, B.D. Belle, F. Schedin, Mishchenko A., T. Georgiou, M.I. Katsnelson, L. Eaves, S. V. Morozov, N.M.R. Peres, J. Leist, A.K. Geim, K.S. Novoselov, and L.A. Ponomarenko, Field-Effect Tunneling Transistor Based on Vertical Graphene Heterostructures., Science (80-.). 335 (2012) 947–50.

[13] W. Cao, J. Kang, W. Liu, Y. Khatami, D. Sarkar, and K. Banerjee, 2d electronics: Graphene and beyond., in: 2013 Proc. Eur. Solid-State Device Res. Conf. (ESSDERC). IEEE, Sep 2013., 2013.

[14] K.S. Novoselov, A. Mishchenko, A. Carvalho, A.H. Castro Neto, 2D Materials and van der Waals Heterostructures., Sci. 353 (2016) aac9439.

[15] A.K. Geim, and I. V. Grigorieva, Van der waals heterostructures., Nature. 499 (2013) 419–25.

[16] Q. Jin, N. Liu, B. Chen, and D. Mei, Mechanisms of semiconducting 2h to metallic 1t phase transition in two-dimensional MoS_2 nanosheets., J. Phys. Chem. C. 122 (2018) 28215–24.

[17] M. Chhowalla, H.S. Shin, G. Eda, L.-J. Li, K.P. Loh, Zhang and H., The chemistry of two-dimensional layered transition metal dichalcogenide nanosheets', Nat. Chem. 5 (2013) 263–275.

[18] A. V. Kolobov and J. Tominaga, Two-Dimensional Transition-Metal Dichalcogenides, Springer International Publishing Switzerland 2016, Switzerland, 2016. https://doi.org/https://doi.org/10.1007/978-3-319-31450-1.

[19] Kumar A. and P.K. Ahluwalia, Electronic structure of transition metal dichalco- genides monolayers 1H-MX_2 (M = Mo, W; X = S, Se, Te) from ab-initio theory: new direct band gap semiconductors., Eur. Phys. J. B, 85(6), Jun 2012. 85 (2012).

[20] B. Radisavljevic, A. Radenovic, J. Brivio, V. Giacometti, and A. Kis, Single-layer MoS_2 transistors, Nat. Nanotechnol. 6(3) (2011) 147–150.

[21] H. Wang, L. Yu, Y.-H. Lee, Y. Shi, A. Hsu, M.L. Chin, L.-J. Li, M. Dubey, J. Kong, and T. Palacios, Integrated circuits based on bilayer M oS2 transistors., Nano Lett. 12 (2012) 4674–80.

[22] S. Larentis, B. Fallahazad, and E. Tutuc, Field-effect transis- tors and intrinsic mobility in

ultra-thin $MoSe_2$ layers., Appl. Phys. Lett. 101 (2012) 223104.

[23] L. Liu, S.B. Kumar, Y. Ouyang, J. Guo, Performance limits of monolayer transition metal dichalcogenide transistors., IEEE Trans. Electron Devices. 58 (2011) 3042–47.

[24] M. Bernardi, M. Palummo, and C. Jeffrey, Grossman. Extraordinary sunlight absorption and one nanometer thick photovoltaics using two-dimensional monolayer materials., Nano Lett. 13 (2013) 3664–70.

[25] F.H.L. Koppens, T. Mueller, P. Avouris, A.C. Ferrari, M.S. Vitiello, and M. Polini, Photodetectors based on graphene, other two-dimensional materials and hybrid systems., Nat. Nanotechnol. 9 (2014) 780–93.

[26] M. Buscema, D.J. Groenendijk, G.A. Steele, H.S.J. van der Zant, and A. Castellanos-Gomez., Photovoltaic effect in few-layer black phosphorus PN junctions defined by local electrostatic gating., Nat. Commun. 5 (2014).

[27] S. Samanta, S.S. Nanthakumar, R.K. Annabattula, and X. Zhuang, Detection of void and metallic inclusion in 2D piezoelectric cantilever beam using impedance measurements., Front. Struct. Civ. Eng. 13 (2019) 542–556.

[28] J. Luceno-Sanchez, A. Dıez-Pascual, and R. Pena Capilla, Materials for Photovoltaics: State of Art and Recent Developments., Int. J. Mol. Sci. 20 (2019) 976.

[29] P. Kumar, J. Liu, P. Ranjan, Y. Hu, S. Sharma, K. Yamijala, S.K. Pati, J. Irudayaraj, and G.J. Cheng, Alpha lead oxide (α- PbO): A new 2D material with visible light sensitivity., Small. 14 (2018) 1703346.

[30] D. Li, R. Cheng, H. Zhou, C. Wang, A. Yin, Y. Chen, N.O. Weiss, Y. Huang, and D. Xiangfeng, Electric-field-induced strong enhancement of electroluminescence in multilayer molybdenum disulfide., Nat. Commun. 6 (2015).

[31] H.R. Gutierrez, N. Perea-Lopez, A.L. Elıas, A. Berkdemir, B. Wang, R. Lv, F. Lopez-Urıas, V.H. Crespi, H. Ter-Rones, and M. Terrones, Extraordinary room-temperature photoluminescence in triangular WS_2 monolayers., Nano Lett. 13 (2013) 3447–54.

[32] R. Ganatra, and Q. Zhang, Few layer MoS_2 : A promising layered semiconductor., Acs Nano . 8 (2014) 4074–4099.

[33] K.F. Mak, K. He, J. Shan, and T.F. Heinz, Control of valley polarization in monolayer MoS_2 by optical helicity., Nat. Nanotechnol. 7(8) (2013) 494–498.

[34] Y. Yu, S.-Y. Huang, Y. Li, S.N. Steinmann, W. Yang, and L. Cao, Layer-dependent

electrocatalysis of MoS_2 for hydrogen evolution., Nano Lett. 14 (2014) 553–558.

[35] H.S.S. Ramakrishna Matte, A. Gomathi, A.K. Manna, D.J. Late Dr., R. Datta Dr., P.S.P. K., C.N.R. Rao Prof. Dr., MoS_2 and WS2 analogues of graphene., Angew. Chem. Int. Ed. Engl. 49 (2010) 4059–4062.

[36] R. Canton-Vitoria, N. Tagmatarchis, Y. Sayed-Ahmad-Baraza, C. Ewelsa, D. Winterauer, T. Batten, D. Winterauer, T. Batten, GAS SENSING USING MONOLAYER MoS_2, in: Nanoscale Mater. Warf. Agent Detect. Nanosci. Secur., 2019: pp. 1–44.

[37] I. Song, C. Park, and H.C. Choi, Synthesis and properties of molybdenum disulphide: from bulk to atomic layers., RSC Adv. 5 (2015) 7495–7514.

[38] X. Zhao, S. Ning, W. Fu, S.J. Pennycook, and K.P. Loh, Differentiating Polymorphs in Molybdenum Disulfide via Electron Microscopy, Adv. Mater. (2018) 1802397.

[39] M. Xia, B. Li, K. Yin, G. Capellini, G. Niu, Y. Gong, W. Zhou, P.M. Ajayan, and Y.-H. Xie, Spectroscopic Signatures of AA′ and AB Stacking of Chemical Vapor Deposited Bilayer MoS_2, ACS Nano. 9 (2015) 12246–12254.

[40] Y.-C. Lin, D.O. Dumcenco, Y.-S. Huang, and K. Suenaga, Atomic mechanism of phase transition between metallic and semiconducting MoS_2 single-layers, Cond-Mat.Mtrl-Sci. (2013) 1–18.

[41] O.L. Krivanek, M.F. Chisholm, V. Nicolosi, T.J. Pennycook, G.J. Corbin, N. Dellby, M.F. Murfitt, C.S. Own, Z.S. Szilagyi, M.P. Oxley, S.T. Pantelides, and S.J. Pennycook, Atom-by-atom structural and chemical analysis by annular dark- field electron microscopy., Nat. 464, 571–574 (2010). 464 (2010) 571–574.

[42] J. Yan, J. Xia, X. Wang, L. Liu, J.-L. Kuo, B.K. Tay, S. Chen, W. Zhou, Z. Liu, and Z. Xiang Shen, Stacking-dependent interlayer coupling in trilayer MoS_2 with broken inversion symmetry., Nano Lett. 15 (2015) 8155–8161.

[43] M. Kan, J.Y. Wang, X.W. Li, S.H. Zhang, Y.W. Li, Y. Kawazoe, Q. Sun, and P. Jena, Structures and phase transition of a MoS 2 monolayer., J. Phys. Chem. C. 118 (2014) 1515–1522.

[44] Y. Cheng, A. Nie, Q. Zhang, L. Gan, and R. Shahbazian-yassar, Origin of the phase transition in lithiated molybdenum disulfide., ACS Nano. 8 (2014) 11447–11453.

[45] A.N. Enyashin and A.L. Ivanovskii, Graphene allotropes., Phys. Status Solidi B. 248 (2011) 1879–1883.

[46] T. Heine, Transition Metal Chalcogenides: Ultrathin Inorganic Materials with Tunable Electronic Properties', Acc. Chem. Res. 48 (2015) 65–72.

[47] Q.H. Wang, K. Kalantar-Zadeh, A. Kis, J.N. Coleman, and M.S. Strano, Electronics and optoelectronics of two-dimensional transition metal dichalcogenides, Nat. Nanotechnol. 7(11) (2012) 699-712.

[48] D. Voiry, A. Mohite, and M. Chhowalla, Phase engineering of transition metal dichalcogenides', Chem Soc Rev. 44 (2015) 2702–2712.

[49] A. Castellanos-Gomez, M. Poot, G.A. Steele, H.S.J. van der Zant, N. Agraït, and G. Rubio-Bollinger, Elastic Properties of Freely Suspended MoS_2 Nanosheets', Adv. Mater. 24 (2012) 772–775.

[50] S. Bertolazzi, J. Brivio, and A. Kis, Stretching and breaking of ultrathin MoS_2., ACS Nano,. 5(12) (2011) 9703-9709.

[51] K. Liu, Q.M. Yan, M. Chen, W. Fan, Y.H. Sun, J. Suh, D.Y. Fu, S. Lee, J. Zhou, S. Tongay, J. Ji, J.B. Neaton, and J.Q. Wu, Elastic properties of chemical-vapor-deposited monolayer MoS_2 , WS2 , and their bilayer heterostructures., Nano Lett. 14 (2014) 5097.

[52] J. Pu, Y. Yomogida, K.-K. Liu, L.-J. Li, Y. Iwasa, and T. Takenobu, Highly Flexible MoS_2 Thin-Film Transistors with Ion Gel Dielectrics', Nano Lett. 12 (2012) 4013–4017.

[53] A. Splendiani, L. Sun, Y.B. Zhang, T.S. Li, J. Kim, C.Y. Chim, G. Galli, and F. Wang, Emerging photoluminescence in mono- layer MoS_2, Nano Lett. 10 (2010) 1271.

[54] K.F. Mak, C. Lee, J. Hone, J. Shan, and T.F. Heinz, Atomically thin MoS_2 : A new direct-gap semiconductor., Phys. Rev. Lett. 105 (2010) 4.

[55] G.-B. Liu, D. Xiao, Y. Yao, X. Xu, and W. Yao, Electronic structures and theoretical modelling of two-dimensional group-VIB transition metal dichalcogenides', Chem Soc Rev. 44 (2015) 2643–2663.

[56] W. Zhao, R.M. Ribeiro, and G. Eda, Electronic Structure and Optical Signatures of Semiconducting Transition Metal Dichalcogenide Nanosheets', Acc. Chem. Res. 48 (2015) 91–99.

[57] A. Molina-Sánchez, D. Sangalli, K. Hummer, A. Marini, and L. Wirtz, Effect of spin- orbit interaction on the optical spectra of single-layer, double-layer, and bulk MoS_2, Phys. Rev. B. 88 (2013).

[58] X. Dou, K. Ding, D. Jiang, X. Fan, and B. Sun, Probing Spin–Orbit Coupling and Interlayer

Coupling in Atomically Thin Molybdenum Disulfide Using Hydrostatic Pressure, ACS Nano. 10 (2016) 1619–1624.

[59] A.R. Klots, A.K.M. Newaz, B. Wang, D. Prasai, H. Krzyzanowska, J. Lin, D. Caudel, N.J. Ghimire, J. Yan, B.L. Ivanov, K.A. Velizhanin, A. Burger, D.G. Mandrus, N.H. Tolk, S.T. Pantelides, and K.I. Bolotin, Probing excitonic states in suspended two-dimensional semiconductors by photocurrent spectroscopy, Sci. Rep. 4 (2015).

[60] N. Zibouche, A. Kuc, J. Musfeldt, and T. Heine, Transition-metal dichalcogenides for spintronic applications: Spintronics beyond graphene, Ann. Phys. 526 (2014) 398–401.

[61] H. Wang, H. Yuan, S.S. Hong, Y. Li, and Y. Cui, Physical and chemical tuning of two-dimensional transition metal dichalcogenides, Chem Soc Rev. 44 (2015) 2664–2680.

[62] H.M. Hill, A.F. Rigosi, C. Roquelet, A. Chernikov, T.C. Berkelbach, D.R. Reichman, M.S. Hybertsen, L.E. Brus, and T.F. Heinz, Observation of Excitonic Rydberg States in Monolayer MoS 2 and WS 2 by Photoluminescence Excitation Spectroscopy, Nano Lett. 15 (2015) 2992–2997.

[63] S. Tongay, J. Suh, C. Ataca, W. Fan, A. Luce, J.S. Kang, J. Liu, C. Ko, R. Raghunathanan, J. Zhou, Defects activated photoluminescence in two-dimensional semiconductors: interplay between bound, charged and free excitons., Sci. Rep. 3 (2013) 1–5.

[64] S. Tongay, J. Zhou, C. Ataca, J. Liu, J.S. Kang, T.S. Matthews, L. You, J. Li, J.C. Grossman, and J. Wu, Broad-Range Modulation of Light Emission in Two-Dimensional Semiconductors by Molecular Physisorption Gating, Nano Lett. 13 (2013) 2831–2836.

[65] H. Li, Q. Zhang, C.C. Yap, B.K. Tay, T.H. Edwin, A. Olivier, and D. Baillargeat, From bulk to monolayer MoS_2: evolution of Raman scattering, Adv. Funct. Mater. 22(7) (2012) 1385–1390.

[66] T.C. Berkelbach, M.S. Hybertsen, and D.R. Reichman, Theory of neutral and charged excitons in monolayer transition metal dichalcogenides, Phys. Rev. B. 88 (2013).

[67] J. Ryou, Y.-S. Kim, S. Kc, and K. Cho, Monolayer MoS_2 Bandgap Modulation by Dielectric Environments and Tunable Bandgap Transistors, Sci. Rep. 6 (2016).

[68] C. Zhang, A. Johnson, C.-L. Hsu, L.-J. Li, and C.-K. Shih, Direct Imaging of Band Profile in Single Layer MoS 2 on Graphite: Quasiparticle Energy Gap, Metallic Edge States, and Edge Band Bending, Nano Lett. 14 (2014) 2443–2447.

[69] K. Kaasbjerg, K.S. Thygesen, and K.W. Jacobsen, Phonon-limited mobility in n -type single-

layer MoS 2 from first principles, Phys. Rev. B. 85 (2012).

[70] D. Jena, and A. Konar, Enhancement of Carrier Mobility in Semiconductor Nanostructures by Dielectric Engineering, Phys. Rev. Lett. 98 (2007).

[71] N. Alidoust, G. Bian, S.-Y. Xu, R. Sankar, M. Neupane, C. Liu, I. Belopolski, D.-X. Qu, J.D. Denlinger, F.-C. Chou, & M.Z. Hasan, Observation of monolayer valence band spin-orbit effect and induced quantum well states in MoX_2, Nat. Commun. 5 (2014) 4673.

[72] H. Zhu, Y. Wang, J. Xiao, M. Liu, S. Xiong, Z.J. Wong, Z. Ye, Y. Ye, X. Yin, and X. Zhang, Observation of piezoelectricity in free-standing monolayer MoS_2, Nat. Nanotechnol. 10 (2014) 151–155.

[73] M. Ghorbani-Asl, A.N. Enyashin, A. Kuc, G. Seifert, and T. Heine, Defect-induced conductivity anisotropy in mos_2 monolayers, Phys. Rev. B. 88 (2013) 245440.

[74] H.J. Conley, B. Wang, J.I. Ziegler, R.F. Haglund, S.T. Pantelides, and K.I. Bolotin, Bandgap Engineering of Strained Monolayer and Bilayer MoS_2, Nano Lett. 13 (2013) 3626–3630.

[75] L. Yang, X. Cui, J. Zhang, K. Wang, M. Shen, S. Zeng, S.A. Dayeh, L. Feng, and Bin Xiang, Lattice strain effects on the optical properties of MoS_2 nanosheets, Sci. Rep. 4 (2015).

[76] Y. Chen, C. Tan, H. Zhang, and L. Wang, Two-dimensional graphene analogues for biomedical applications, Chem Soc Rev. 44 (2015) 2681–2701.

[77] J. V. Lauritsen, J. Kibsgaard, S. Helveg, H. Topsøe, B.S. Clausen, E. Lægsgaard, and F. Besenbacher, Size-dependent structure of MoS_2 nanocrystals, Nat. Nanotechnol. 2 (2007) 53–58.

[78] S. Yu, and W. Zheng, Fundamental insights into the electronic structure of zigzag MoS_2 nanoribbons, Phys Chem Chem Phys,. 18 (2016) 4675–4683.

[79] B.J. Alder, and T.E. Wainwright, Phase transition for a hard sphere system, J. Chem. Physics, Vol. 27, No. 5, Pp. 1208–1209, 1957. 27 (1957) 1208–1209.

[80] D. C. Rapaport, The Art of Molecular Dynamics Simulation. Cambridge: 1995., Cambridge University Press, 1995.

[81] H. C. Andersen, Molecular dynamics simulations at constant pressure and/or temperature, J. Chem. Physics,. 72 (1980) 2384–2393.

[82] G. Bussi, D. Donadio, and M. Parrinello, Canonical sampling through velocity rescaling, J. Chem. Physics, 126 (2007) 014101–7.

[83] H.J.C. Berendsen, J.P.M. Postma, van Gunsteren W. F., A. DiNola, and J.R. Haak, Molecular dynamics with coupling to an external bath, J. Chem. Phys. 81 (1984) 3684–3690.

[84] P.H. Hnenberger, Thermostat algorithms for molecular dynamics simulations, Adv. Comput. Simul. 173 (2005) 105–149.

[85] D.. Holian, and B.L. Evans, The nose–hoover thermostat, J. Chem. Physics, 83 (1985) 4069–4074.

[86] W.G. Hoover, Canonical dynamics: Equilibrium phase-space distributions, Phys. Rev. A. 31 (1985) 1695–1697.

[87] S. Nose, A unified formulation of the constant temperature molecular dynamics methods, J. Chem. Phys. 81 (1984) 511–519.

[88] G.J. Martyna, D.J. Tobias, and M.L. Klein, Constant pressure molecular dynamics algorithms, J. Chem. Physics, Vol. 101, No. 5, Pp. 4177–4189, 1994. 101 (1994) 4177–4189.

[89] M. Griebel, and J. Hamaekers, Molecular dynamics simulations of the mechanical properties of polyethylene-carbon nanotube composites, in: M. Rieth W. Schommers, Eds., American Scientific Publis, 2006: p. vol. 9, pp. 409–454,.

[90] M.E. Tuckerman, J. Alejandre, R. López-Rendón, A.L. Jochim, and G.J. Martyna, A liouville-operator derived measure-preserving integrator for molecular dynamics simulations in the isothermal–isobaric ensemble, J. Phys. A. Math. Gen. 39 (2006) 5629.

[91] W. Jiang, H.S. Park, and T. Rabczuk, Molecular dynamics simulations of single-layer molybdenum disulphide (MoS_2): Stillinger-Weber parametrization, mechanical properties and thermal conductivity, J. Appl. Phys. 114 (2013) 063074.

[92] J.-W. Jiang, H.S. Park, and T. Rabczuk, MoS_2 nanoresonators: intrinsically better than graphene?, Nanoscale. 6 (2014) 3618–3635.

[93] A. Kandemir, H. Yapicioglu, A. Kinaci, T. Cagin, C. Sevik, Thermal transport properties of MoS_2 and $MoSe_2$ monolayers, Nanotechnology. 27 (2015) 55703.

[94] M. Wen, S.N. Shirodkar, P. Plech, E. Kaxiras, R.S. Elliott, and E.B. Tadmor, A force-matching Stillinger-Weber potential for MoS_2 : Parameterization and Fisher information theory based sensitivity analysis, J. Appl. Phys. 122 (2017) 244301.

[95] N. Wakabayashi, H.G. Smith, and R.M. Nicklow, Lattice dynamics of hexagonal MoS_2 studied by neutron scattering, Phys. Rev. B. 12 (1975) 659.

[96] J.R. Shewchuk, An Introduction to the Conjugate Gradient Method Without the Agonizing

Pain, Sci. . 49 (1994).

[97] M. Zibignew, Genetic Algorithms + Data Structures = Evolutionary Algorithms, Springer-Verlag, Berlin : Germany, 1996.

[98] J. Kennedy, R.C. Eberhart, and Y. Shi, Swarm Intelligence, Morgan Kaufmann, San Francisco., 2001. https://doi.org/https://doi.org/10.1016/B978-1-55860-595-4.X5000-1.

[99] M. Fischer and Y. Leung, Geo Computational Modelling Techniques and Applications, Springer-Verlag, Berlin. (2001).

[100] W. Barnett, C. Chiarella, S. Keen, R. Marks, and H. Schnabl, Complexity and Evolution, Cambridge University Press., 2000.

[101] X. Yao, Evolutionary Computation: Theory and Application, World Scientific Publ. Co., Singapore., 1999.

[102] M. Patel, V. Honavar, and K. Balakrishnan, Advances in the Evolutionary Sysnthesis of Intelligent Agents, The MIT Press, Cambridge, MA., 2001.

[103] D. Goldberg, Genetic Algorithms in Search, Optimization, and Machine Learning, Addison-Wesley, Reading, MA., 1989.

[104] X. Yao, Evolutionary Computation: A Gentle Introduction, in: Evol. Optim. R. Sarker, M. Mohammadian X. Yao (Edited), 2002: pp. 27–56.

[105] H.-P. Schwefel, Numerical Optimization of Computer Models, Wiley, Chichester, 1981.

[106] H.-P. Schwefel, Evolution and Optimum Seeking, Wiley, New York, 1995.

[107] L.J. Fogel, A.J. Owens, and M.J. Walsh, Artificial Intelligence Through Simulated Evolution, NY: John Wiley & Sons., New York, 1966.

[108] D.B. Fogel, Evolutionary Computation: Towards a New Philosophy of Machine Intelligence, NY: IEEE Press, New York, 1995.

[109] J. Holland, Adaptation in Natural and Artificial Systems, University of Michigan Press, Ann Arbor, MI, USA., 1975.

[110] K.A.D. Jong, An Analysis of the Behaviour of a Class of Genetic Adaptive Systems, University of Michigan, An Arbor, 1975.

[111] J.R. Koza, Genetic Programming, Cambridge, Mass: The MIT Press., MA., 1992.

[112] M. Bazaraa, and C. Shetty, Nonlinear Programming: Theory and Algorithm, Jhon Wiley & Sons, New York, 1979.

[113] J. Seydel, and D.L. Olson, Bids considering multiple criteria, J. Constr. Eng. Manag. . 116 (1990) 609–623.

[114] R. Sarker, T. Runarsson, and C. Newton, A Constrained Multiple Raw Materials Manufacturing Batch Sizing Problem, Int. Trans. Oper. Res. Blackwell's. 8 (2001) 121–138.

[115] D. Whitley, V.S. Gordon, and K. Mathias, Lamarckian Evolution, the Bladwin Effect and Function Optimization, in: Proc. 3 Rd Conf. Parallel Probl. Solving from Nat., 1996.

[116] Z. Michalewicz, and M. Schmidt, Evolutionary Algorithms and Constrained Optimization, in: Chapter-3, Evol. Optim. R. Sarker, M. Mohammadian X. Yao, Kluwer, USA, 2001: pp. 57–86.

[117] R. Sarker, T. Runarsson, and C. Newton, Genetic Algorithms for Solving A Class of Constrained Nonlinear Integer Programs, Int. Trans. Oper. Res. Blackwell's. 8 (2001) 61–74.

[118] F. Hillier and G. Lieberman, Introduction to Operations Research, McGraw-Hill, Boston, USA., 2001.

[119] G. Sierksma, Linear and Integer Programming: Theory and Practice, Marcel Dekker, Inc., New York, 1996.

[120] R. Martin, Large Scale Linear and Integer Optimization, Kluwer Academic Publishers, Boston, 1999.

[121] H. Eiselt, G. Pederzoli, and C. Sandblom, Continuous Optimization Models, de Gruyter, Berlin, Germany, 1987.

[122] R. Varela, C. Vela, J. Puente, and A. Gomez, A Knowledge-Based Evolutionary Strategy for Scheduling Problems with Bottlenecks, Eur. J. Oper. Res. 145 (2003) 55–71.

[123] M. Sakawa, and K. Kato, Genetic Algorithms with Double Strings for 0-1 Programming Problems, Eur. J. Oper. Res. 144 (2003) 581–597.

[124] R. Sarker, K. Liang, and C. Newton, A New Evolutionary Algorithm for Multiobjective Optimization, Eur. J. Oper. Res. Elsevier Sci. 140 (2002) 12–23.

[125] E. Zitzler, K. Deb, and L. Thiele, Comparison of Multiobjective Evolutionary Algorithms: Empirical Results, Evol. Comput. 8 (2000) 173–195.

[126] E. Zitzler, and L. Thiele, Multiobjective Evolutionary Algorithms: A Comparative Case Study and the Strength Pareto Approach, IEEE Trans. Evol. Comput. 3 (1999) 257–271.

[127] K. Deb, Multi-objective genetic algorithms: Problem difficulties and construction of test

problems, Evol. Comput. 7 (1999) 205–230.

[128] K.-H. Liang, Evolutionary Optimization with Self-Adaptation and Landscape Approximation, UNSW@ADFA, 2000.

[129] P. Wide, and H. Schellwat, Implementation of a genetic algorithm for routing an autonomous robot, Robotica. 15 (1997) 207–211.

[130] K. De Jong, Evolving in a Changing World. Foundation of Intelligent Systems, in: In Z. Ras and A. Skoworn (eds.), Lecture Notes in Artificial Intelligence 1609, Springer, 1999: pp. 513–519.

[131] A. Eiben, R. Hinterding, and Z. Michalewicz, Parameter Control in Evolutionary Algorithms, , IEEE Trans. Evol. Comput. 3 (1999) 124–141.

[132] J. He and L. Kang, On the Convergence Rates of Genetic Algorithms, , Theor. Comput. Sci. 229 (1999) 23–39.

[133] M.M.J. Treacy, T.W. Ebbesen, and J.M. Gibson, Exceptionally high young's modulus observed for individual carbon nanotubes. , Nat. . 381 (1996) 678.

[134] C. Lee, X. Wei, J.W. Kysar, and J. Hone, Measurement of the elastic properties and intrinsic strength of monolayer graphene, Science (80-.). 321 (2008) 385.

[135] U. Ozgur, Y.I. Alivov, C. Liu, A. Teke, M.A. Reshchikov, S. Dogan, V. Avrutin, S.J. Cho, and H. Morkoc, A comprehensive review of zno materials and devices, J. Appl. Phys. . 98 (2005) 103.

[136] J.Q. Wu, When group-iii nitrides go infrared: New properties and perspectives, J. Appl. Phys. 106 (2009) 011101.

[137] Y.G. Sun and J.A. Rogers, Inorganic semiconductors for flexible electronics, Adv. Mater. 19 (2007) 1897.

[138] J.A. Rogers, T. Someya, and Y.G. Huang, Materials and mechanics for stretchable electronics, Sci. 327(5973), 1603 (2010). 327 (2010) 1603.

[139] S. Iijima, Helical microtubules of graphitic carbon, Nat. 354 (1991) 56.

[140] A. Alivisatos, Semiconductor clusters, nanocrystals, and quantum dots, Sci. New Ser. 5251 (1996) 933–937.

[141] H.J. Dai, Carbon nanotubes: Synthesis, integration, and properties, Accounts Chem. Res. 35 (2002) 1035.

[142] S.Z. Butler, S.M. Hollen, L.Y. Cao, Y. Cui, J.A. Gupta, H.R. Gutierrez, T.F. Heinz, S.S. Hong, J.X. Huang, A.F. Ismach, E. Johnston-Halperin, M. Kuno, V.V. Plashnitsa, R.D. Robinson, R.S. Ruoff, S. Salahuddin, J. Shan, L. Shi, M.G. Spencer, M. Terrones, W. Windl, and J.E. Goldberger, Progress, challenges, and opportunities in two-dimensional materials beyond graphene, ACS Nano. 7 (2013) 2898.

[143] K.S. Novoselov, A.K. Geim, S.V. Morozov, D. Jiang, M.I. Katsnelson, I.V. Grigorieva, S.V. Dubonos, Firsov and A.A., Two-dimensional gas of massless dirac fermions in graphene, Nat. . 438 (2005) 197.

[144] A. Splendiani, L. Sun, Y. Zhang, T. Li, J. Kim, C.Y. Chim, and Z. Shen, Emerging photoluminescence in monolayer MoS_2., Nano Lett. 10(4) (2010) 1271–1275.

[145] M. Liu, X.B. Yin, E. Ulin-Avila, B.S. Geng, T. Zentgraf, L. Ju, F. Wang, and X. Zhang, A graphene-based broadband optical modulator, Nat. . 474 (2011) 64.

[146] D. Xiao, G.B. Liu, W.X. Feng, X.D. Xu, and W. Yao, Coupled spin and valley physics in monolayers of MoS_2 and other group-vi dichalcogenides, Phys. Rev. Lett. . 108 (2012) 5.

[147] M.F. Yu, O. Lourie, M.J. Dyer, K. Moloni, T.F. Kelly, and R.S. Ruoff, Strength and breaking mechanism of multiwalled carbon nanotubes under tensile load, Sci. 287 (2000) 637.

[148] C. Lee, X.D. Wei, J.W. Kysar, and J. Hone, Measurement of the elastic properties and intrinsic strength of monolayer graphene. , Sci. 321 (2008) 385.

[149] U. Komaragiri, M.R. Begley, and J.G. Simmonds, The mechanical response of freestanding circular elastic films under point and pressure loads, J. Appl. Mech. . 72 (2005) 203.

[150] A. Castellanos-Gomez, R. Roldán, E. Cappelluti, M. Buscema, F. Guinea, and H.S. van der Zant, Local strain engineering in atomically thin MoS_2, Nano Lett. 13(11) (2013) 5361-5366.

[151] Y.H. Lee, X.Q. Zhang, W.J. Zhang, M.T. Chang, C.T. Lin, K.D. Chang, Y.C. Yu, J.T.W. Wang, C.S. Chang, L.J. Li, and T.W. Lin, Synthesis of large-area MoS_2 atomic layers with chemical vapor deposition, Adv. Mater. 24 (2012) 2320.

[152] K. Kang, S.E. Xie, L.J. Huang, Y.M. Han, P.Y. Huang, K.F. Mak, C.J. Kim, D. Muller, and J. Park, High-mobility three-atom-thick semiconducting films with wafer-scale homogeneity, Nat. 520 (2015) 656.

[153] G.H. Lee, R.C. Cooper, S.J. An, S. Lee, A. van der Zande, N. Petrone, A.G. Hammerherg, C. Lee, B. Crawford, W. Oliver, J.W. Kysar, and J. Hone, High-strength chemical-vapor

deposited graphene and grain boundaries, Sci. 340 (2013) 1073.

[154] J.L. Feldman, Elastic-constants of 2h-MoS_2 and 2h-$NbSe_2$ extracted from measured dispersion curves and linear compressibilities., J. Phys. Chem. Solids. 37 (1976) 1141.

[155] A. Castellanos-Gomez, M. Poot, G.A. Steele, H.S. van der Zant, and N. Agraït, Elastic properties of freely suspended MoS_2 nanosheets, (2012). 24(6) (n.d.) 772-775.

[156] K. Liu, and J. Wu, Mechanical properties of two-dimensional materials and heterostructures, Nano Lett. 2.14 (2014) 5094–5103.

[157] R.C. Cooper, C. Lee, C. a. Marianetti, X. Wei, J. Hone, and J.W. Kysar, Nonlinear elastic behavior of two-dimensional molybdenum disulfide, Phys. Rev. B. 87 (2013) 0.35423.

[158] Y. Li, C. Yu, Y. Gan, P. Jiang, J. Yu, Y. Ou, D.-F. Zou, C. Huang, J. Wang, T. Jia, Q. Luo, X.-F. Yu, H. Zhao, C.-F. Gao, and J. Li, Mapping the elastic properties of two-dimensional MoS_2 via bimodal atomic force microscopy and finite element simulation, Npj Comput. Mater. 49. 4 (2018) 49.

[159] Q. Peng and S. De, Outstanding mechanical properties of monolayer MoS_2 and its application in elastic energy storage, Phys. Chem. Chem. Phys. 15 (2013) 19427.

[160] W. Zhou, X. Zou, S. Najmaei, Z. Liu, Y. Shi, J. Kong, J. Lou, P.M. Ajayan, B.I. Yakobson, and J.-C. Idrobo, Intrinsic structural defects in monolayer molybdenum disulfide, Nano Lett. 13(6) (2013) 2615–22. https://doi.org/10.1021/nl4007479.

[161] C. Jin, F. Lin, K. Suenaga, and S. Iijima, Fabrication of a Freestanding Boron Nitride Single Layer and Its Defect Assignments, Phys. Rev. Lett. 102 (2009) 195505.

[162] R. Ansari, S. Ajori, and B. Motevalli, Mechanical properties of defective single-layered graphene sheets via molecular dynamics simulation, Superlattices Microstruct. 51 (2012).

[163] Hong J., Z. Hu, and M. Probert, Exploring atomic defects in molybdenum disulphide monolayers., Nat Commun. 6 (2015) 6293.

[164] A. Mahata, J.-W. Jiang, D.R. Mahapatra, and T. Rabczuk, Effect of intrinsic structural defects on mechanical properties of single layer MoS_2., Nano-Structures & Nano-Objects. 18 (2019) 100247.

[165] W. Wang, C. Yang, L. Bai, M. Li, and W. Li, First-Principles Study on the Structural and Electronic Properties of Monolayer MoS_2 with S-Vacancy under Uniaxial Tensile Strain, Nanomater. 2018, 8, 74. 8 (2018) 74.

[166] N. Samaneh, and M. Zaiser, Rupture of graphene sheets with randomly distributed defects,

AIMS Mater. Sci. 3 (2016) 1340–49. https://doi.org/10.3934/matersci.2016.4.1340.

[167] M. Li, Y. Wan, L. Tu, Y. Yang, and J. Lou, The Effect of $VMoS_3$ Point Defect on the Elastic Properties of Monolayer MoS_2 with REBO Potentials., Nanoscale Res Lett. 11 (2016) 155.

[168] F. Giannazzo, M. Bosi, F. Fabbri, E. Schilirò, G. Greco, and F. Roccaforte, Direct Probing of Grain Boundary Resistance in Chemical Vapor Deposition-Grown Monolayer MoS_2 by Conductive Atomic Force Microscopy., Phys. Status Solidi RRL. 14 (2020) 1900393.

[169] M. Born, On the stability of crystal lattices, Mathematical Proceedings of the Cambridge Philosophical Society, 1940.

[170] M. Born and K. Huang, Dynamics Theory of Crystal Lattices, Oxford University Press, 1954.

[171] J.F. Nye, Physical Properties of Crystals, Oxford University Press, 1957.

[172] D.C. Wallace, Thermodynamics of Crystals, Wiley, 1972.

[173] G. Grimvall, B. Magyari-Köpe, V. Ozoliņš, and K.A. Persson, Lattice instabilities in metallic elements, Rev. Mod. Phys. 84 (2012) 945.

[174] R. Wang, W. Yang, C. Hu, and D. -h. Ding, Point and space groups and elastic behaviours of one-dimensional quasicrystals, J. Phys. Condens. Matter. 9 (1997) 2411.

[175] J. Wang, R. Zhang, D.H. Ding, and R. Wang, Positive-definite conditions of elastic constants of two-dimensional quasicrystals with noncrystallographic symmetries, Acta Crystallogr A. 55 (1999) 558.

[176] M. Maździarz, Comment on "The Computational 2D Materials Database: high-throughput modeling and discovery of atomically thin crystals," 2D Mater. 6 (2019). https://doi.org/10.1088/2053-1583/ab2ef3.

[177] M. Carroll, Must elastic materials be hyperelastic?, Math. Mech. Solids. 14 (2009) 369–76.

[178] J. Hetnarski, and R. Ignaczak, The Mathematical Theory of Elasticity, 2nd edn, Taylor and Francis, London, UK, 2010.

[179] A. Blinowski, J. Ostrowska-Maciejewska, and J. Rychlewski, Two-dimensional Hooke's tensors-isotropic decomposition, effective symmetry criteria, Arch. Mech. 48 (1996) 325–45.

[180] Q.C. He, Zheng and Q.S, On the symmetries of 2D elastic and hyperelastic tensors, J. Elast. 43 (1996) 203–25.

[181] S.. Mehrabadi and M.. Cowin, Eigen tensors of linear anisotropic elastic materials, Q.J.

Mech. Appl. Math. 43 (1990) 15–41.

[182] J.. Nye, Physical Properties of Crystals: their Representation by Tensors and Matrices, Clarendon, oxford, 1985.

[183] Y. Dimitrienko, Tensor Analysis and Nonlinear Tensor Functions, Springer, Netherlands, 2002.

[184] M. Maździarz and M. Gajewski, Estimation of isotropic hyperelasticity constitutive models to approximate the atomistic simulation data for aluminium and tungsten monocrystals, Comput. Mod. Eng. Sci. 105 (2015) 123–50.

[185] F.-X. Mouhat and F. Coudert, Necessary and sufficient elastic stability conditions in various crystal systems, Phys. Rev. B 90 224104. 90 (2014) 224104.

[186] J.A. Stewart and D.E. Spearot, Atomistic simulations of nanoindentation on the basal plane of crystalline molybdenum disulfide (MoS_2), Model. Simul. Mater. Sci. Eng. 21 (2013) 45003.

[187] S. Thomas, K.M. Ajith, and M.C. Valsakumar, Directional anisotropy, finite size effect and elastic properties of hexagonal boron nitride, J. Phys. Condens. Matter. 28 (2016) 295305.

[188] S. Thomas, K.M. Ajith, S. Uck Lee, and M.C. Valsakumar, Assessment of the mechanical properties of monolayer graphene using the energy and strain fluctuation methods, RSC Adv. 2018, 8, 27283–27292. 8 (2018) 27283–92.

[189] J. Zhou, and R. Huang, Internal lattice relaxation of single-layer graphene under in-plane deformation, J. Mech. Phys. Solids 2008, 56, 1609–1623. 56 (2008).

[190] A. Stukowski, Visualization and analysis of atomistic simulation data with ovito-the open visualization tool., Model. Simulat. Mater. Sci. Eng. 18 (2009) 015012.

[191] N.T. Hung, A.R. Nugraha, and R. Saito, Two-dimensional MoS_2 electromechanical actuators, J. Phys. D Appl. Phys. 51 (2018) 75306.

[192] R.B. van Dover, L.F. Schneemeyer, and R.M. Fleming, Discovery of a useful thin-film dielectric using a composition-spread approach, Nature. 392 (1998) 162–164.

[193] M.J. Akhter, W. Kus, A. Mrozek, and T. Burczynski, Mechanical Properties of Monolayer MoS_2 with Randomly Distributed Defects, Materials (Basel). 1307 (2020) 13. https://doi.org/10.3390/ma13061307.

[194] M.F. Khan, G. Nazir, V.M. lermolenko, and J. Eom, Electrical and photo-electrical properties of MoS_2 nanosheets with and without an Al_2O_3 capping layer under various

environmental conditions, Sci. Technol. Adv. Mater. 17 (2016) 166–176.

[195] X. Li, and H. Zhu, Two-dimensional MoS_2: Properties, preparation, and applications. Xiao Li, Hongwei Zhu. 2015, journal of metriomics, J. Metriomics. 1 (2015) 33–44.

[196] M. Heiranian, A.B. Farimani, and N.R. Aluru, Water desalination with a single-layer MoS_2 nanopore, Nat. Commun. 6 (2015) 8616.

[197] J. Feng, K. Liu, R.D. Bulushev, S. Khlybov, D. Dumcenco, A. Kis, and A. Radenovic, Identification of single nucleotides in MoS_2 nanopores., Nat. Nanotechnol. (2015).

[198] T. Yang, H. Lin, X. Zheng, K.P. Loh, and B. Jia, Tailoring pores in graphene-based materials: from generations to applications, J. Mater. Chem. A. 5 (2017) 16537–16558.

[199] M. Macha, S. Marion, V.V.R. Nandigana, A. Radenovic, 2D materials as an emerging platform for nanopore-based power generation, Nat. Rev. Mater. 4 (2019) 588–605.

[200] S. Su, X. Wang, and J. Xue, Nanopores in two-dimensional materials: accurate fabrication, Mater. Horizons. 8 (2021) 1390–1408.

[201] M. Graf, M. Lihter, M. Thakur, V. Georgiou, J. Topolancik, B.R. Ilic, K. Liu, J. Feng, Y. Astier, and A. Radenovic, Fabrication and practical applications of molybdenum disulfide nanopores, Nat. Protoc. 14 (2019) 1130–1168.

[202] A.B. Farimani, K. Min, and N.Aluru, DNA base detection using a single-layer MoS_2., Acs Nano. 8 (2014) 7914–7922.

[203] K. Liu, J. Feng, A. Kis, and A. Radenovic, Atomically thin molybdenum disulfide nanopores with high sensitivity for DNA translocation, Acs Nano. 8 (2014) 2504–2511.

[204] P. Waduge, I. Bilgin, J. Larkin, R.. Henley, K. Goodfellow, A. Graham, D. Bell, N. Vamivakas, S. Kar, and M. Wanunu, Direct and scalable deposition of atomically thin low-noise MoS_2 membranes on apertures. , Acs Nano 9, 7352-7359. 9 (2015) 7352–7359.

[205] J.A. Wilson and A. Yoffe, The transition metal dichalcogenides discussion and interpretation of the observed optical, electrical and structural properties, Adv. Phys. 18 (1969) 193–335.

[206] X. Liu, T. Xu, X. Wu, Z. Zhang, J. Yu, H. Qiu, J.. Hong, C. Jin, J. Li, X. Wang, L. Sun, and W. Guo, Top-down fabrication of sub-nanometre semiconducting nanoribbons derived from molybdenum disulfide sheets., Nat. Commun. 4 (2013) 1776.

[207] R. Zan, Q.M. Ramasse, R. Jalil, T. Georgiou, U. Bangert, K. Novoselov, Control of radiation damage in MoS_2 by graphene encapsulation, ACS Nano . 7 (2013) 10167–10174.

[208] P. Vancsó, G.Z. Magda, J. Pető, J.-Y. Noh, Y.-S. Kim, C. Hwang, L.P. Biró, and L. Tapasztó, The intrinsic defect structure of exfoliated MoS_2 single layers revealed by Scanning Tunneling Microscopy, Sci. Rep. 6 (2016) 29726.

[209] Y. Li, P. Chen, C. Zhang, J. Peng, F. Gao, and H. Liu, Molecular dynamics simulation on the buckling of single-layer MoS_2 sheet with defects under uniaxial compression, Comput. Mater. Sci. 162 (2019) 116–123.

[210] T. Burczyński, W. Kuś, W. Beluch, A. Długosz, A. Poteralski, and M. Szczepanik, Intelligent Computing in Inverse Problems. In: Intelligent Computing in Optimal Design. Solid Mechanics and Its Applications, Springer, Cham, 2020. https://doi.org/10.100 (accessed December 12, 2021).

[211] T. Burczyński, and G. Kokot, Evolutionary algorithms and boundary element method in generalized shape optimization, J. Theor. Appl. Mech. 41 (2003) 341–364.

[212] T. Burczyński, W. Beluch, A. Dlugosz, M. Nowakowski, and P. Orantek, Coupling of the boundary element method and evolutionary algorithms in optimization and identification problems, Eur. Congr. Comput. Methods Appl. Sci. Eng. ECCOMAS. (2000) 11–14.

[213] O. Sigmund, Tailoring materials with prescribed elastic properties, Mech. Mater. 20 (1995) 351–368.

[214] A. Mrozek, W. Kuś, and T. Burczyński, Nano level optimization of graphene allotropes by means of a hybrid parallel evolutionary algorithm., Comput. Mater. Sci., 106 (2015) 161–169.

[215] A. Mrozek, W. Kus, and T. Burczynski, Method for determining structures of new carbon-based 2d materials with predefined mechanical properties, Int. J. Multiscale Comput. Eng. 15 (2017) 379–394.

[216] S.W. Cranford and M.J. Buehler, Mechanical properties of graphyne, Carbon, 49(13), (2011) 4111–4121.

[217] M. Maździarz, A. Mrozek, W. Kuś, and T. Burczyński, Anisotropic-cyclicgraphene: a new two-dimensional semiconduct- ing carbon allotrope, Mater. 11 (2018) 1–12.

[218] A. Mrozek and T. Burczyński, Examination of mechanical properties of graphene allotropes by means of computer simulation, Comput. Assist. Methods Eng. Sci. 20 (2013) 309–323.

[219] H. Park, M.R. Fellinger, T.J. Lenosky, W.W. Tipton, D.R. Trinkle, S.P. Rudin, C. Woodward, J.W. Wilkins, and R.G. Hennig, Ab initio based empirical potential used to

study the mechanical properties of molybdenum, Phys. Rev. B. 85 (2012) 214121.

[220] Q. Peng, W. Ji, and S. De, Mechanical properties of graphyne monolayers: a first-principles study, Phys. Chem. Chem. Phys. 14 (2012) 13385–13391.

[221] A. Mrozek, Basic mechanical properties of 2H and 1T single-layer molybdenum disulfide polymorphs. A short com- parison of various atomic potentials, Int. J. Multiscale Comput. Eng. 17 (2019) 339–359.

[222] W. Kuś, M.J. Akhter, and T. Burczyński, Optimization of monolayer MoS_2 with prescribed mechanical properties, Mater. 15 (2022) 1–9.

[223] W. Kuś, and A. Mrozek, Optimization of carbon based flat structures topologies by using parallel computing, Comput. Methods Mater. Sci., 16 (2016) 163–168.

[224] A. Mrozek, W. Kuś, and T. Burczyński, Searching of stable configurations of nanostructures using computational intelligence methods, Tech. Sci. 20 (2010) 85–97.

[225] R.J. Hardy, Formulas for determining local properties in molecular dynamics simulations: Shock waves, J. Chem. Phys. 76 (1982) 622–628.

[226] J.F. Lutsko, Stress and elastic constants in anisotropic solids: Molecular dynamics techniques, J. Appl. Phys. 64 (1988) 1152–1154.

[227] D.H. Tsai, The virial theorem and stress calculation in molecular dynamics, J. Chem. Phys. 70 (1979) 1375–1382.

[228] J.A. Zimmerman, E.B. WebbIII, J.J. Hoyt, R.E. Jones, P.A. Klein, and D.J. Bammann, Calculation of stress in atomistic simulation, Model. Simul. Mater. Sci. Eng. 12 (2004) 319.

[229] J. Cormier, J.M. Rickman, and T.J. Delph, Stress calculation in atomistic simulations of perfect and imperfect solids, J. Appl. Phys. . 89 (2001) 99–104.

[230] A.P. Thompson, S.J. Plimpton, and W. Mattson, General formulation of pressure and stress tensor for arbitrary many-body interaction potentials under periodic boundary conditions, J. Chem. Phys. 131 (2009) 154107.

[231] A. Mrozek, W. Kuś, P. Orantek, and T. Burczyński, Prediction of the aluminium atoms distribution using evolutionary algorithm., Recent Dev. Artif. Intell. Methods. 10 (2005) 127–130.

[232] F. Giannazzo, S. Sonde, and V. Raineri, Electronic Properties of Graphene Probed at the Nanoscale, in: Phys. Appl. Graphene - Exp., 2011: pp. 352–376.

[233] P. preuss, Bilayer Graphene Gets a Bandgap, (2009). https://newscenter.lbl.gov/2009/06/10/graphene-bandgap/.